


Spring 1-1-2014

Sea Level Reconstruction: Validation and Value

Mathew David West Strassburg

University of Colorado Boulder, mathew.strassburg@colorado.edu

Follow this and additional works at: https://scholar.colorado.edu/asen_gradetds

 Part of the [Aerospace Engineering Commons](#), [Climate Commons](#), and the [Oceanography Commons](#)

Recommended Citation

Strassburg, Mathew David West, "Sea Level Reconstruction: Validation and Value" (2014). *Aerospace Engineering Sciences Graduate Theses & Dissertations*. 83.

https://scholar.colorado.edu/asen_gradetds/83

This Dissertation is brought to you for free and open access by Aerospace Engineering Sciences at CU Scholar. It has been accepted for inclusion in Aerospace Engineering Sciences Graduate Theses & Dissertations by an authorized administrator of CU Scholar. For more information, please contact cuscholaradmin@colorado.edu.

SEA LEVEL RECONSTRUCTIONS: VALIDATION AND VALUE

by

MATHEW DAVID WEST STRASSBURG

B.S., University of Colorado, 2007

M.S., University of Colorado, 2011

A thesis submitted to the

Faculty of the Graduate School of the

University of Colorado in partial fulfillment

of the requirement for the degree of

Doctor of Philosophy

Department of Aerospace Engineering Sciences

2014

This thesis entitled:
Sea Level Reconstruction: Validation and Value
written by Mathew D. W. Strassburg
has been approved for the Department of Aerospace Engineering Sciences

Dr. Robert Leben

Dr. Benjamin Hamlington

Dr. Steve Nerem

Dr. William Emery

Dr. Weiqing Han

Date_____

The final copy of this thesis has been examined by the signatories, and we
Find that both the content and the form meet acceptable presentation standards
Of scholarly work in the above mentioned discipline.

Strassburg, Mathew D.W., (Ph.D., Aerospace Engineering Sciences)

Sea Level Reconstruction: Validation and Value

Thesis directed by Dr. Robert Leben

The ability to see how sea level has changed from past states or to accurately project how it will change in the future is limited by historical sea level data. Tide gauge measurements have a long temporal record but limited spatial coverage and satellite altimetry provides global measurements but has only been available for 20 years. Reconstructions extend spatially dense datasets, such as those from satellite altimetry, by decomposing the dataset into basis functions and fitting those functions to in-situ tide gauge measurements with a longer temporal record. A longer temporal record allows one to separate signals that cannot be found in the relatively short altimeter record. However, the fidelity and utility of sea level reconstructions is still a topic of discussion.

I compare and evaluate two methods for reconstructing sea level and show how reconstructions can be beneficial where other sea level datasets are limited. The compared sea level reconstruction methods differ in the technique for calculating basis functions, i.e. empirical orthogonal functions (EOFs) versus cyclostationary EOFs (CSEOFs). Additionally, I use published sea level reconstruction datasets to analyze changes in the North Equatorial Current bifurcation point, in regional trends in the Southeast Asian Seas, and in the

contribution of the Pacific Decadal Oscillation (PDO) to global sea level over the last 60 years. These results give direction for making high quality sea level reconstructions and identify significant scientific findings made possible through reconstructing sea level. Sea level reconstructions provide the ability to separate natural recurring signals from those that are historically unprecedented, such as the rise in global mean sea level, which is an unparalleled virtue given the current state of the climate.

ACKNOWLEDGEMENTS

I would like to express my gratitude, first and foremost to my advisor and co-advisor, Dr. Robert Leben and Dr. Benjamin Hamlington, both of whom were quite intimidating when I first began graduate school but have become great mentors and good friends over the past few years. Bob(o) has the uncanny ability to pick out the most significant aspect of a paper/figure/argument while others are still trying to process it. This has helped me to learn where to look and how to find importance in many things I once would've missed. I could always count on him for a good conversation when I needed a break from writing code. Ben unknowingly talked me into pursuing my PhD while having a burger at a 50's diner in downtown Lisbon, of all places. I've come to really appreciate his extensive knowledge and patience, especially after receiving some very understandable explanations of rather complex subjects from him (and occasionally different explanations on the same subject when I was particularly confused).

Additional contributors to this endeavor include Dr. William Emery, who encouraged me to study remote sensing and helped me find an advisor when applying for the program, and Dr. Steve Nerem, who emboldened me by requesting I guest lecture in his orbital mechanics and remote sensing courses.

My mom and sister have shown me amazing support through my extended academic career, although sometimes I wonder if it's because they just want to say there's a "rocket scientist" in the family. Regardless, I could not ask for more from either of them. Amanda and Jax have, in their own ways, been a continuous inspiration and constant reminder to never give up and to stay optimistic. Lastly, my dad always set the example to never quit learning. I consider myself very lucky and am entirely grateful to have had the mentors, friends, and family that I've had.

CONTENTS

CHAPTER 1 INTRODUCTION	1
CHAPTER 2 BACKGROUND AND THEORY	4
2.1 Overview of Reconstructions.....	4
2.2 Decomposing Simple Signals Using CSEOFs.....	11
2.3 Conclusions and Discussion	18
CHAPTER 3 CSEOF VS. EOF BASIS FUNCTION COMPARISON.....	19
3.1 Overview	19
3.2 Data and Methods	20
3.3 Results.....	27
3.4 Conclusions and Discussion	52
CHAPTER 4 VARIABILITY IN THE NORTH EQUATORIAL CURRENT (NEC) BIFURCATION LOCATION.....	56
4.1 Overview	56
4.2 Data and Methods	57
4.3 Results.....	59
4.4 Conclusions and Discussion	66
CHAPTER 5 SEA LEVEL TRENDS IN SOUTH EAST ASIAN SEAS (SEAS).....	68
5.1 Overview	68

5.2	Data and Methods	73
5.3	Results.....	76
5.4	Conclusions and Discussion	83
CHAPTER 6 INVESTIGATING THE PACIFIC DECADEAL OSCILLATION (PDO) CONTRIBUTION TO GLOBAL SEA LEVEL		86
6.1	Overview	86
6.2	Data and Methods	88
6.3	Results.....	89
6.4	Conclusions and Discussion	99
CHAPTER 7 CONCLUSION.....		103
CHAPTER 8 REFERENCES.....		105

TABLES

Table 1. Correlation between parameters calculated from AVISO training dataset and parameters calculated from various CSEOF reconstructions.	32
Table 2. Correlation between parameters calculated from AVISO training dataset and parameters calculated from various EOF reconstructions.	33
Table 3. Correlation between parameters calculated from AVISO training dataset and parameters calculated from various EOF reconstructions using EOF0.	48
Table 4. Summary of sea level reconstruction properties.	74

FIGURES

- Figure 1. Top: Original data (blue) and reformed CSEOF time series (from mode 1) with nested periods of 5 (green) and 20 (red). Middle: Trend of original data (blue) and mode 1 PC time series with nested periods of 5 (green) and 20 (red). Bottom: Mode 1 LV with nested periods of 5 (green) and 20 (red). 13
- Figure 2. Top: Original data (blue) and reformed CSEOF time series with nested periods of 5 (green) and 50 (red). Middle: Trend of original data (blue) and mode 1 PC time series with nested periods of 5 (green) and 20 (red). Bottom: Mode 1 LV with nested periods of 5 (green) and 50 (red). The left column is for the first CSEOF mode and the right column is for the second CSEOF mode. 15
- Figure 3. Top: Original data (blue) and reformed CSEOF time series with nested periods of 5 (green) and 20 (red). Middle: Trend of original data (blue) and mode 1 PC time series with nested periods of 5 (green) and 20 (red). Bottom: Mode 1 LV with nested periods of 5 (green) and 20 (red). The left column is for the first CSEOF mode and the right column is for the second CSEOF mode. 17
- Figure 4. Trend pattern from the 1993-2012 AVISO record. An average spatial trend of 0.26 has been removed. All units in cm/yr. 21
- Figure 5. Spatial distribution of all historical tide gauges used (top) and number of available tide gauges during a given decade (bottom)..... 23

- Figure 6. Additional synthetic tide gauge locations: ideal grid (upper left), basin edges only (upper right), northern hemisphere grid (lower left), southern hemisphere grid (lower right).24
- Figure 7. CSEOF reconstruction trend patterns (left column) and EOF Reconstruction trend patterns (right column) calculated with synthetic tide gauge distribution from the 1930's (top row), 1970's (middle row), and all available tide gauges (bottom row). All units in cm/yr.28
- Figure 8. Detrended GMSL from AVISO data (blue) compared to GMSL from CSEOF reconstruction (top) and EOF reconstruction (bottom). Reconstructions with all tide gauge records are depicted by solid lines, while reconstructions with 1930's tide gauge records are depicted by dotted lines. Note: All GMSL data have been smoothed by 3 months for clarity.....30
- Figure 9. CSEOF reconstruction with ideal tide gauge distribution (left column) and CSEOF reconstruction with edge tide gauge distribution (right column) correlations (top row), and relative amplitudes (bottom row). Note: ideal relative amplitude is 0.....36
- Figure 10. Identical to Figure 9 for EOF reconstructions.38
- Figure 11. CSEOF reconstruction (left column) and CSEOF reconstruction with tide gauge noise (right column) trend maps (top row), correlations (middle row), and relative amplitudes (bottom row). Note: the top colorbar (in cm/yr) is associated with the top row, while the bottom colorbar is associated with the middle and bottom rows; ideal relative amplitude has a value of 0..... 40

- Figure 12. EOF reconstruction (left column) and EOF reconstruction with tide gauge noise (right column) trend maps (top row), correlations (middle row), and relative amplitudes (bottom row). 42
- Figure 13. Detrended GMSL from AVISO (blue) data compared to GMSL from CSEOF reconstruction (top) and EOF reconstruction (bottom). Reconstructions with noisy tide gauge records are depicted by dotted lines..... 44
- Figure 14. Similar to Figure 7 with 90% of the decomposed variance remaining in the reconstructions. Colorbar units are cm/yr. 46
- Figure 15. Detrended GMSL from AVISO (blue) data compared to GMSL from EOF reconstruction without EOF0 (green) and EOF reconstruction with EOF0 (dotted). 49
- Figure 16. CSEOF reconstruction trend patterns (left column) and EOF Reconstruction trend patterns (right column) calculated in the Atlantic Ocean(top row) and the Pacific Ocean (bottom row). All units in cm/yr. 51
- Figure 17. Mean sea surface height from *Rio et al.* [2011], ranging from 65 cm (blue) to 180 cm (red) with contours of 10 cm. The proxy box is shown in black. 59
- Figure 18. Hovmoller diagrams of SSH from HLK (left), AVISO (middle), and CW (right). Average of 12-14 °N latitude band, from 130 to 270 °E, over the time period 1993 to 2009. 60

- Figure 19. Bifurcation latitude time series from AVISO satellite altimetry data (green) and HLK reconstruction (blue). Time series are low pass filtered with a Gaussian filter and annual corner frequency. 61
- Figure 20. Top: NEC bifurcation latitude calculated from HLK and filtered as in Figure 19. Bottom: Wavelet power spectrum for reconstruction inferred bifurcation latitude; contour unit ($^{\circ}$)²; >95% confidence interval indicated by bold line; dashed line indicates cone of influence for edge effects. 62
- Figure 21. Modal variance averaged in the 12-14°N latitude band. Mode 19 starts on the top (red) and they decrease in descending order to mode 1 on the bottom (dark blue). 64
- Figure 22. Non-filtered NEC bifurcation latitude inferred from sea level reconstruction using only modes 2, 3, 9, 17 (blue) and filtered NEC bifurcation latitude inferred from full HLK (green). 66
- Figure 23. The 20 bodies of water (seas, straits, and gulfs) defined in the Limits of the Ocean and Seas [IHO, 1953] fro the SEAS region. 70
- Figure 24. Schematic of remotely forced wave pathways into the Indonesian throughflow region (after *Wijffels and Meyers* [2004]). Red lines show the waveguide from the equatorial Indian Ocean, with energy spreading into the internal seas through both Lombok and Ombai Straits (red arrows). Black lines show the pathways for equatorial Pacific wind energy traveling down the Papuan/Australian shelf break and radiating westward-propagating Rossby Waves into the Banda Sea and South Indian Ocean (black arrows). 72

Figure 25. SEAS average sea level trends over the 17-year satellite altimeter record from 1993-2009 shown plotted as trend values with standard error estimates (A) and as color maps for AVISO and each of the reconstructions. Reconstructed average trends agree with AVISO (shown in bold) to within the estimated error. 77

Figure 26. Lagged correlation coefficient (shown as the blue line in the upper plot) of the historical 17-year regional trend maps with the linear trend map from the satellite altimeter time period 1993-2009 centered on 2001 (rightmost blue dot). The bottom plot shows the 17-year sea level trend maps from HLK/BV in mm/year for the 1959-1976 (left), 1977-1992 (center), and 1993-2009 (right) time periods. The blue dots shown on the upper plot are the center points of the three 17-year windows. 78

Figure 27. SEAS average sea level trends over the 17-year time period from 1959 through 1975 shown plotted as trend values with standard error (upper plot) and as color maps (bottom panels) for each reconstruction. 80

Figure 28. SEAS average sea level trends over the 17-year time period from 1976 through 1992 shown plotted as trend values with standard error (upper plot) and as color maps (bottom panels). 81

Figure 29. SEAS average sea level trends from the HLK/TG reconstruction for the three 17-year time periods centered on 1967, 1984, and 2001..... 82

- Figure 30. SEAS average sea level trends over the 60-year time period from 1950 through 2009 shown as plotted as trend values with standard error (upper plot) and as color maps (bottom panels) for each of the reconstructions. 84
- Figure 31. Regional distribution of sea level trends from 1993-2011 for the AVISO dataset (left), the *Hamlington et al.* [2011b] reconstructed sea level (HLK) (center), and the *Church et al.* [2004] reconstructed sea level (CW) (right)..... 90
- Figure 32. Correlation between the regional trend map from the AVISO dataset and twenty-year trend patterns from two sea level reconstructions, HLK (blue) and CW (green). Twenty-year trend patterns from the HLK dataset are also shown for two different periods associated with extrema in the correlation time series. 91
- Figure 33. Loading vectors (top) and PCTS (bottom) for the EOF decomposition of twenty-year trends in the HLK dataset. The first three modes are shown, explaining 84% of the variance in the twenty-year trend patterns. 93
- Figure 34. Top: Comparison between the mode 1 of the EOF decomposition of twenty-year trends from the HLK dataset and twenty-year trends computed from the PDO index (shown with opposite sign for direct comparison). Bottom: Contribution of the first three EOF modes to the twenty-year trends in GMSL. For comparison, the twenty-year trends computed directly from the GMSL of HLK are shown with a mean value of 1.54 mm/year removed. 95
- Figure 35. Sea level trends (mm/year) from 1993 to 2010 for (A) AVISO data, (B) PDO contribution estimated from HLK sea level reconstruction, (C) AVISO

minus the PDO contribution. Note, GMSL trend has been removed from AVISO
data..... 98

CHAPTER 1 INTRODUCTION

Many things may be inferred by studying the height of the ocean. One can determine ocean-surface velocity, variations of ocean circulation, and changes in global ocean volume among other things. In recent years, the importance of measuring and understanding sea level has become all the more pronounced as 'climate change' has become a household term. Specific focus has been given to sea level rise due to thermal expansion, melting of glaciers and ice caps, and ice loss of Greenland and Antarctic ice sheets [*Church and White, 2011*]. Variations in sea level over long time periods provide important insight into the state of the climate. Understanding these variations, on both a global and regional scale, is critical to projecting future sea level rise and the associated implications. Of equal importance is being able to compare the current state of the ocean with previous states. Historically, sea level has been monitored two ways: through a number of tide gauges placed along coasts, and more recently through satellite measurement.

Since 1993 satellite altimetry has provided precise measurements of sea surface height (SSH) with near-global coverage. These measurements have led to the first definitive estimates of global mean sea level (GMSL) rise [e.g. *Nerem, 1995*] and have improved our understanding of how sea level is changing regionally at decadal timescales [*Bromirski et al., 2011*]. The relatively short satellite record,

however, does little to answer the question of how the current state of the ocean compares to previous states. Tide gauges, on the other hand, have measured sea level over the last 200 years, with some records extending back to 1807. While providing long records, the spatial resolution of tide gauges is poor, making studies of GMSL and the large-scale patterns of low-frequency ocean variability difficult. To overcome these challenges and to make accurate comparisons between climate variations over different time periods, a long and consistent data record is necessary.

Sea level reconstructions offer a solution to these shortcomings by decomposing the globally complete satellite altimetry dataset into basis functions and fitting those functions to the long records of the tide gauges. This yields a dataset with the high spatial resolution of satellite altimetry and the longer record length of tide gauges. One challenge of reconstructing sea level is proving the accuracy of the dataset and optimizing the reconstruction technique. This work takes a deeper look at reconstruction methods, accuracy, and differing ways they can be useful.

In this thesis, I analyze two basic methods of sea level reconstruction that differ only in the choice of basis functions used to fit to the historical tide gauge measurements and discuss relevant scientific findings made possible by reconstructing sea level. Chapter 2 introduces previous sea level reconstruction work and goes into detail regarding the two examined methods of creating the basis of reconstruction, namely empirical orthogonal functions (EOFs) and

cyclostationary EOFs (CSEOFs). Chapter 3 compares the aforementioned methods of reconstructing sea level using a known dataset. The remainder of the work goes into the useful results that can be obtained using sea level reconstructions. Chapter 4 looks at the nature of the variability of the bifurcation point of the North Equatorial Current in the Tropical Pacific. Interesting trends are found in the Southeast Pacific using full, published reconstructions and shown in Chapter 5. Chapter 6 discusses how sea level reconstruction has given insight into how a decadal signal contributes to global sea level. Finally, Chapter 7 summarizes the results and discusses how sea level reconstruction may evolve in the future.

CHAPTER 2 BACKGROUND AND THEORY

2.1 Overview of Reconstructions

In two hundred years, measuring sea level has evolved from a few physical gauges drawing tidal variations on a rotating drum to a number of satellites measuring global ocean height with radar and beaming the results back to Earth. Remotely sensing sea level using satellite altimetry began in the mid-70s, but it wasn't until 1992 with the launch of TOPEX/Poseidon that there was sufficient measurement precision and orbit accuracy to make the data fruitful. Conceptually, satellite altimetry is a simple premise. The range from the satellite to the ocean is determined by transmitting a burst of microwave radiation from the altimeter toward the sea surface and measuring the time it takes for the reflected energy to return. Sea level can then be determined by removing the range from the satellite height above a reference ellipsoid. In practice, it's not quite that simple, as many corrections (instrument, atmospheric, sea-state bias, geophysical) need to be made to achieve sufficient measurement precision [*Chelton et al.*, 2001].

Satellites such as TOPEX/Poseidon and the Jason series have provided global sampling (315 km equatorial cross-track separation) of sea level every ten days, allowing for scientific analysis of topics ranging from mesoscale circulation to the rate of sea level rise. Unfortunately, the 20-year satellite altimetry data record is

not sufficient to see how the ocean has been changing over the past century and makes it difficult to predict future oceanographic changes. Prior to satellite altimetry, the only means of measuring sea level was through tide gauges. Tide gauges are distributed on coastlines around the world with some records dating back to the 1800's. Most records, however, begin in the 1950s or later. The usefulness of tide gauge data is limited due to geographic clustering, a scarce number of gauges, and a lack of gauges in the middle of the ocean basins. Combining a shorter but essentially complete global data set, such as one offered by satellite altimetry, with the longer but sparsely distributed tide gauge dataset draws on the advantages of both data types, allowing for better monitoring and understanding of sea level signals associated with observed oceanic processes and greater predictive capabilities of what is to come.

Reconstructing sea level initially focused on global mean sea level (GMSL) rise preceding the satellite altimetry record [e.g. *Church et al.*, 2004 (hereinafter *CW2004*); *Hamlington et al.*, 2011b (hereinafter *H2011*)]. It has since been determined that sea level reconstructions can also provide valuable insight into other ocean signals prior to the satellite altimetry era [e.g. *Hamlington et al.*, 2013]. Of particular interest are longer period signals and the modulation of shorter signals, as these could not have been fully captured in the short 20-year satellite altimetry record. Sea level reconstructions can also be used to explain secular trends and multi-year climate variability such as the El Niño-Southern Oscillation (ENSO), as shown in *H2011*. More recently, reconstructions have proven useful in

capturing lower frequency variability, such as the contribution of the Pacific Decadal Oscillation (PDO) to GMSL [*Hamlington et al.*, 2013; *Hamlington et al.*, Under Review], as will be discussed in Chapter 6.

The most accepted approach for sea level reconstructions is similar to that used by *Smith et al.* [1996], *Kaplan et al.* [1998] and *Smith and Reynolds* [2004] for sea surface temperature (SST), and *Chambers et al.* [2002], *CW2004*, *Berge-Nguyen* [2008], *Llovel et al.* [2009], *Church and White* [2011], *Ray and Douglas* [2011], and *Meyssignac* [2012] for sea level. It involves forming a set of basis functions through empirical orthogonal function (EOF) decomposition of the dense training dataset. A second technique uses a basis function decomposition process known as cyclostationary empirical orthogonal function (CSEOF) analysis, proposed by *Kim et al.* [1996], and verified by *Kim and North* [1997], *Kim and Wu* [1999], and *Kim and Chung* [2001]. The CSEOF technique excels in extracting physical climate modes from geophysical datasets and was adopted and implemented by *Hamlington et al.* [2011b, 2012, 2013] for sea level reconstruction. Basis functions found using either of the above methods are then used to interpolate the tide gauge data to create a reconstruction.

Although the method for computing basis functions varies between EOF and CSEOF reconstructions, they are similar in that they decompose the data into spatial patterns (known as loading vectors (LVs)) with a corresponding amplitude time series (known as the principal component (PCs) time series). The distinguishing difference is that CSEOFs can account for non-stationary signals

because each LV is not a single spatial pattern, but a set of time dependent spatial patterns corresponding to a nested period. Each individual LV and PC time series pair represents a mode of variability, and summing over all modes recovers the initial data set. The lower order modes explain more variance and higher order modes contain more of the noise inherently found in the initial dataset. To avoid reproducing this noise in the reconstruction, only a limited number of lower order modes are used in a reconstruction. The signal neglected in the higher order modes is referred to as truncation error. There is a delicate trade-off when selecting the number of modes to use: keeping less variance causes physical signals to be left out of the reconstruction, while keeping too much variance may cause increased noise levels in the reconstruction. In the sections to follow, each method of calculating basis functions is described.

2.1.1 EOF Reconstructions

Singular value decomposition (SVD) is used to calculate the eigenvectors and eigenvalues of the spatial covariance structure, as explained in *CW2004* and *Meyssignac et al.* [2012]. An initial dataset, H , can be broken down into spatial eigenvectors also called loading vectors (LVs), and amplitude time series also called principal component (PC) time series, as well as the eigenvalues, λ .

$$H(r,t) = LV(r)\lambda PC^T(t) \quad (1)$$

Each EOF mode is comprised of a spatial pattern (LV) modulated by a corresponding amplitude time series (PC). The first few grave modes contain the most explained variance and often depict physical phenomena. For reconstruction of sea level prior to the timespan of the original data, amplitude time series (PC^{α} s) are calculated based on how the tide gauges fit the satellite data. These coefficients are found by solving for least squares or minimizing a cost function (see a comparison in *Christiansen et al.* [2010]). The reconstruction, \hat{H} , can then be formed in the following manner:

$$\hat{H}(r,t) = \sum_{i=1}^K LV_i(r) PC_i^{\alpha}(t) \quad (2)$$

In equation (2), K is the total number of modes used to create the reconstruction. As explained by *H2011*, EOF basis functions may not be ideal for sea level reconstruction because the LV s are forced to be stationary with respect to time (no time dependence). That is, a certain mode can contribute more or less to the reconstructed dataset from a temporal standpoint but the spatial pattern is fixed. This limits EOF reconstruction's ability to extract cyclostationary signals such as propagating waves or moving periodic patterns [e.g. *H2011*].

CW2004 added a homogeneous EOF (known as EOF0, or mode of 1's) with unit amplitude prior to fitting to the tide gauges to account for ocean mass and volume variations causing mean sea level changes. This allows for most of the secular trend to be extracted in one mode, but constrains the entire reconstruction

period to a similar trend. Also, the ability to capture climate signals in GMSL as well as regional trends is lost because the spatial mean of the remaining EOFs is removed. This spatial mean removal prevents any changes in mean sea level from being misrepresented as regional sea level trend. The benefits and limitations associated with using an EOF0 are discussed in Chapter 3.

2.1.2 CSEOF Reconstructions

CSEOF analysis was first introduced by *Kim et al.* [1996] as a method to extract time varying signals in the climate and have been shown to surpass EOFs in capturing cyclostationary signals [*Kim and Wu*, 1999]. Simply stated, the difference between EOFs and CSEOFs is the ability for CSEOFs to capture spatial patterns that vary in time and space. This is possible because the spatial maps comprising the CSEOF LVs are time dependent, whereas EOF LVs only vary spatially. The details for CSEOF analysis are complex, however, and are unnecessary for the understanding of the results in this dissertation. CSEOF analysis is briefly introduced below and the reader is directed to *Kim and North* [1997] if more detail is desired.

CSEOF LVs are periodic with a chosen “nested period”, with a period of d in (3). This period is selected to best reflect the data type in question. Climate and geophysical datasets exhibit one-year periodicity primarily due to seasonal variations in solar insolation, making a 1-year nested period a valid choice for the comparisons in Chapter 3, and the full CSEOF reconstruction used in Chapters 4, 5, and 6. *H2011* demonstrated that a 1-year nested period can also extract lower

frequency signals, such as the El Niño Southern Oscillation (ENSO) signal, which has a 3-6 year stochastic period, and is phase locked to the annual cycle. The following explanation is similar to that given by *H2011*. Section 2.2 of this chapter shows simplified examples of CSEOF decomposition, but for more discussion on the process and the nested period, refer to *Yeo and Kim [2013]*. Depending on the frequency of the data sampling, each CSEOF LV consists of a number of spatial maps with a corresponding PC. With a 1 year nested period, there are 52 maps in each LV when considering weekly data. For a reconstruction comparable to that shown in (2), the following applies for CSEOFs:

$$\begin{aligned}\hat{H}(r,t) &= \sum_{i=1}^K LV_i(r,t) PC_i^\alpha \\ LV(r,t) &= LV_i(r,t+d)\end{aligned}\quad (3)$$

Where it can be seen that the LVs now have a dependency on time that is directly related to the nested period, d . A covariance matrix, C , must be defined, which additionally takes into account other points in space and time, r' and t' , respectively:

$$C(r,t;r',t') = C(r,t+d;r',t'+d) \quad (4)$$

This shows that the space-time covariance matrix is also now periodic in time. The use of (4) when solving for the CSEOF LVs allows for cyclostationary signals to be extracted by also making the LVs periodic with the nested period. The LVs and PC time series are related as follows:

$$C(r,t;r',t')LV(r',t') = \lambda LV(r,t) \quad (5)$$

Because the covariance matrix is no longer square when considering the nested period, the problem cannot be solved in the same manner as EOFs, i.e., SVD. Alternatively, (4) is Fourier transformed twice, so it can be expressed in the same manner as EOFs in Fourier space. One transform is with respect to t and one with respect to t' , exploiting the periodic nature of C . Both the LVs and PC time series are obtained while in Fourier space and then transformed back into physical space. Again, more details are available in *Kim et al.* [1996] for the curious audience.

2.2 Decomposing Simple Signals Using CSEOFs

The selection of the nested period is not a trivial task. To clarify this and illustrate the benefits of CSEOF decomposition, examples of CSEOF decomposition of one-dimensional time series are shown here. Nested period is chosen based on knowledge about a set of data. Because of the seasonal variations inherent in many climate signals, a nested period of one year is often the optimal choice when dealing with the ocean. There are cases when a diurnal or monthly nested period may be better suited, such as the height of the ionosphere or ocean tide signals.

In general, selecting a less than ideal nested period will not ruin the results of the decomposition but it might make it more difficult to separate signals of interest. If the nested period is much less than a specific signal's period, the CSEOF collapses into an EOF. That is, the loading vectors move towards time

independence. If the nested period is much larger than a specific signal's period, the signal may be repeated many times in the LV. In this case, some of the long-term variation of a short period signal will be mixed between the CSEOF and LV, or multiple signals captured in one mode. This makes it difficult to separate long and short variability, such as the modulated annual cycle and the annual cycle [H2011].

2.2.1 A Growing Periodic Signal

This example shows how CSEOFs can separate a periodic signal from a trend as shown in (6).

$$y = (t/10)\cos(2\pi t/5). \quad (6)$$

Given the periodicity of (6), a natural nested period selection would be 5. The top panel in Figure 1 shows this data plotted over a time series from $t = 0$ to $t = 100$. When reforming only the first mode (out of two), there is slight underestimation from truncating the second mode. However, both CSEOF decompositions capture nearly all of the variance in a single mode. The difference becomes a little more apparent when looking at the lower panels. The trend is almost completely captured in the PC time series, while the periodic signal is captured in the loading vectors. It can be seen that using a longer than ideal nested period of 20 causes some of the periodic signal to mix with the PC time series, which is most noticeable in the end effects. In other words, if this were real a dataset under analysis, there is a slight risk that a small portion of periodic signal could be misinterpreted as trend if using a larger than ideal nested period. The LVs using each nested period are virtually identical with the exception of the length (although difficult to see, the

green LV from the decomposition with a nested period of 5 only extends to $t = 5$). Of course, the clear benefit here is the ability of CSEOFs to separate trend and periodic signal in a single mode.

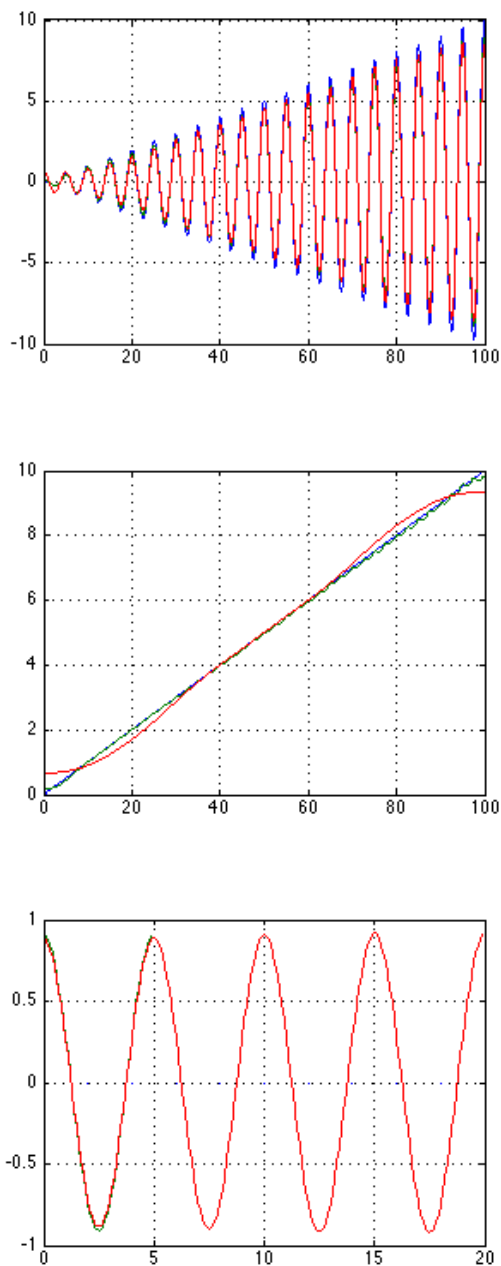


Figure 1. Top: Original data (blue) and reformed CSEOF time series (from mode 1) with nested periods of 5 (green) and 20 (red). Middle: Trend of original data (blue) and mode 1 PC time series with nested periods of 5 (green) and 20 (red). Bottom: Mode 1 LV with nested periods of 5 (green) and 20 (red).

2.2.2 A Growing Periodic Signal With a Long Oscillation

A more complex signal is given in (7). This signal is comparable to a higher frequency signal with increasing amplitude with an underlying oscillation at $1/10^{\text{th}}$ of the higher frequency.

$$y = (t/10)\cos(2\pi t/5) + \sin(2\pi t/50). \quad (7)$$

CSEOF decompositions were performed with the obvious nested periods of 5 and 50 (Figure 2). The left side of Figure 2 shows that for a nested period of 5, the first mode behaves almost identically as that with the simpler time series of (6) (Figure 1), i.e., the PC accounts for the trend while the LV accounts for the high frequency oscillation. The second mode's PC time series (right panel) picks up the lower frequency variability. Thus, with a nested period of 5, the CSEOF easily separates each original signal.

The CSEOF decomposition with the nested period of 50 still pulls out the trend in the first PC time series, but now the nested period is sufficiently long enough to capture both the lower and higher frequency in the first LV. In this case, more variability is captured in the first mode, but the signals are less obvious and the second mode does not yield insight into the original signal. With much more complex datasets, such as global sea level, separation of signals becomes hugely beneficial.

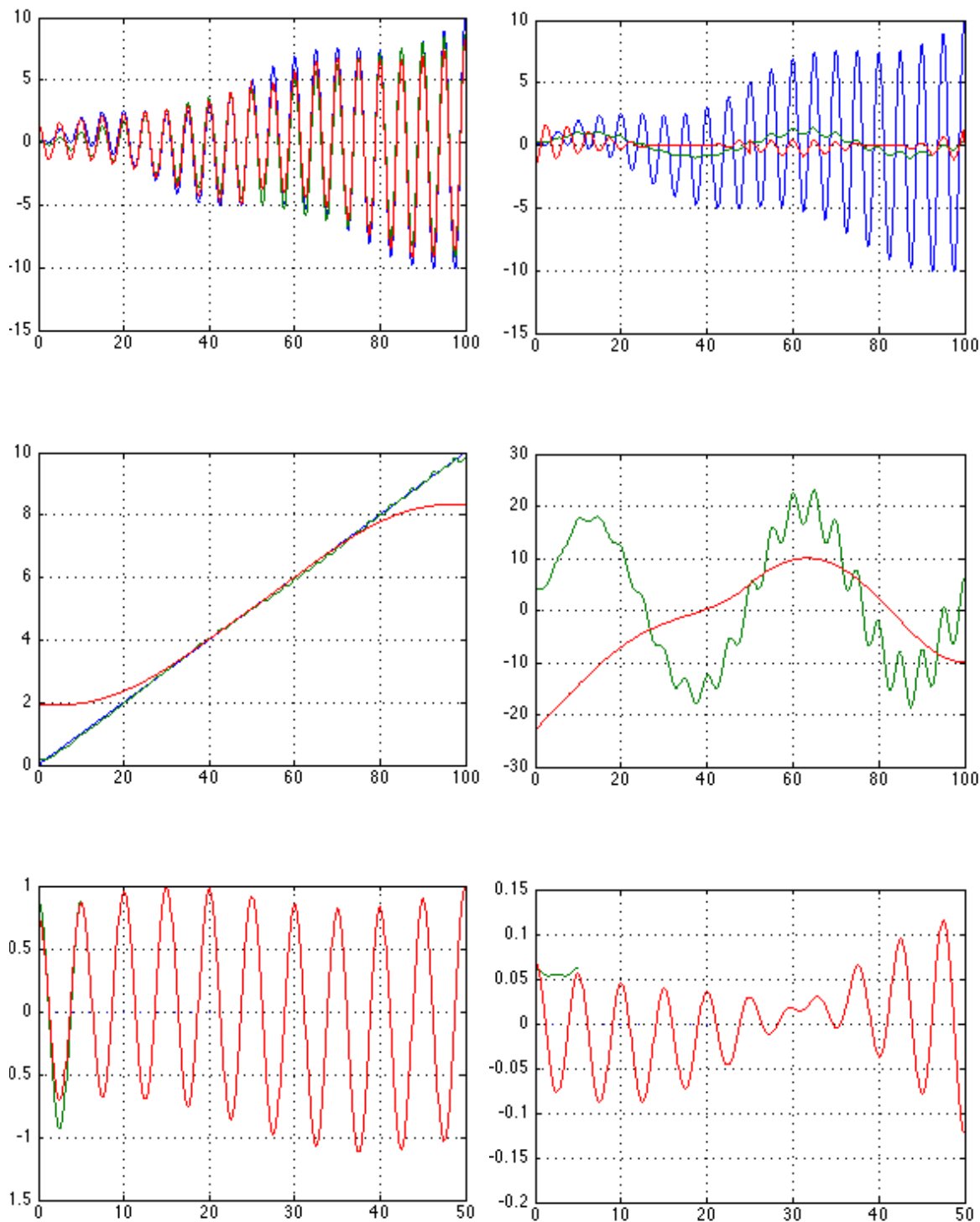


Figure 2. Top: Original data (blue) and reformed CSEOF time series with nested periods of 5 (green) and 50 (red). Middle: Trend of original data (blue) and mode 1 PC time series with nested periods of 5 (green) and 20 (red). Bottom: Mode 1 LV with nested periods of 5 (green) and 50 (red). The left column is for the first CSEOF mode and the right column is for the second CSEOF mode.

2.2.3 Two Growing Periodic Signals

The final example is a combination of two signals, both increasing in amplitude, with one having a period four times greater than the other, as in (8).

$$y = (t/10)\cos(2\pi t/5) + (t/10)\cos(2\pi t/20) . \quad (8)$$

Again, obvious nested periods of 5 and 20 are used in the CSEOF decomposition. Similar to in the previous section, the shorter nested period allows the CSEOF process to more fully separate the signals. In this case ($d = 5$), the PC time series from mode 1 contains the longer period signal and its trend and mode 2 contains the shorter period signal in the LV with the trend in the time series, but looking at both modes it becomes apparent that again the shorter nested period allows for more overall separation of the initial data. Using a nested period of 20 allows for nearly the entire time series to be captured in the first mode. The trend is again well separated in the PC, while the combined oscillations are in the LV. This is possible because, unlike in Figure 2, the low frequency signal is still relatively short compared to the entire data time span. This leads to a valuable observation about reconstructions: the more training data you have, the better the reconstruction. Unfortunately, only the passage of time yields more satellite altimetry training data.

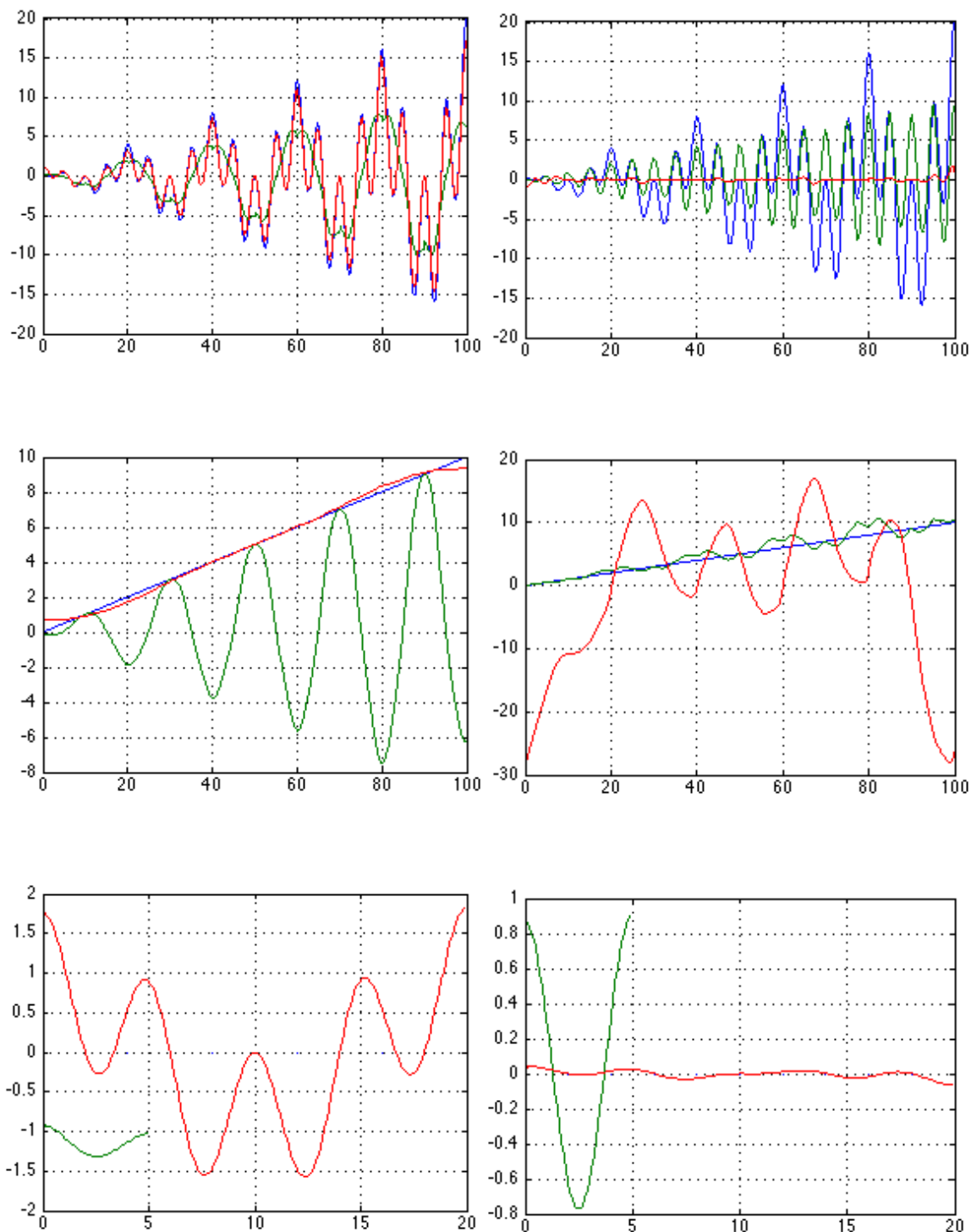


Figure 3. Top: Original data (blue) and reformed CSEOF time series with nested periods of 5 (green) and 20 (red). Middle: Trend of original data (blue) and mode 1 PC time series with nested periods of 5 (green) and 20 (red). Bottom: Mode 1 LV with nested periods of 5 (green) and 20 (red). The left column is for the first CSEOF mode and the right column is for the second CSEOF mode.

2.3 Conclusions and Discussion

Although the basic principles behind EOFs and CSEOFs are similar, they are significantly different with respect to the way they are computed and the results they yield. The main difference is the ability of the CSEOF method to account for time in the loading vectors, and thus, separate cyclostationary signals. The benefit of this as it relates to reconstructing sea level is expanded on through the remainder of this dissertation.

Additionally, using examples of simplified signals that could be considered akin to ocean signals, it was shown that although there are no wrong nested periods (the worst that can happen is a very computationally expensive EOF), there are certainly right ones. Sometimes the nested period is obvious, sometimes it depends on the final objective of the analysis, and sometimes it takes the 'trial and error' method to find.

CHAPTER 3 CSEOF VS. EOF BASIS FUNCTION COMPARISON

3.1 Overview

This chapter compares the EOF and CSEOF methods of calculating basis functions described in Chapter 2. This comparative study seeks to answer five open questions in an idealized setting using the available satellite altimeter record:

1. How sensitive is each method to tide gauge selection?
2. How sensitive is each method to tide gauge noise?
3. How does the amount of reconstructed variance affect reconstruction quality?
4. How does incorporating EOF0 affect the EOF reconstruction skill?
5. How does reconstructing a specific basin individually differ from reconstructing the global ocean?

To answer these questions, CSEOF and EOF reconstructions are created with varying tide gauge distribution based on historical completeness (Section 3.3.1), extreme tide gauge distributions (Section 3.3.2), with tide gauge time series that include noise (Section 3.3.3), with basis functions consisting of different percentages of retained variance (Section 3.3.4), including EOF0 in the EOF reconstruction (Section 3.3.5), and reconstructing the Atlantic and Pacific Oceans independently (Section 3.3.6). These reconstructions are then compared with the original dataset by investigating regional trends, point-wise correlation, point-wise relative

amplitude, reproducibility of variability in GMSL, and reproducibility of known oceanographic indices.

3.2 Data and Methods

3.2.1 Satellite Altimetry Dataset

The basis of estimation for the reconstructions and the benchmark with which we compare is the Archiving, Validation, and Interpretation of Satellite Oceanographic (AVISO; <http://www.aviso.oceanobs.com/>) half degree gridded dataset spanning 1993 through 2012 created from TOPEX/Poseidon, Geosat, GFO, ERS-1 & 2, Jason-1 & 2, and Cryosat-2 satellite altimetry measurements. The Ssalto/Duacs multimission altimeter data processing system created the dataset using improved homogeneous corrections, global crossover minimization, and intercalibration to derive highly accurate along-track anomaly data. The along-track data were gridded using space-time objective mapping to account for correlated noise [Le Traon *et al.*, 1998]. This dataset was updated, reprocessed, and released in June 2013. In this study, weekly data on a $0.5^{\circ} \times 0.5^{\circ}$ grid, spanning from 1993 through 2012 are used, which is subsampled from the original $0.25^{\circ} \times 0.25^{\circ}$ gridded AVISO dataset. For use as the training (or calibration) data, each grid point time series had a mean, and linear, annual, and semiannual least squares fits removed. Any grid points that were not continuous over the entire time period were removed.

The seasonal cycle is a dominant source of periodic variance in ocean height and it has been shown that it can be captured well with both decomposition

techniques [H2011]. Thus, it is not valuable to examine it here. Leaving a secular trend in the training dataset complicates the reconstruction process using both methods of basis function calculation. The linear trend is not decomposed into a single mode because of the limited satellite data record length. Additionally, leaving this secular signal in the training dataset could impose a fixed trend pattern over the entire reconstruction time period, which cannot be assumed to be accurate. For these reasons and because reconstructing secular trends in GMSL has previously been discussed [Christiansen *et al.*, 2010], I choose to exclude this signal from the training dataset. The zero-mean trend map of the AVISO dataset is shown in Figure 4.

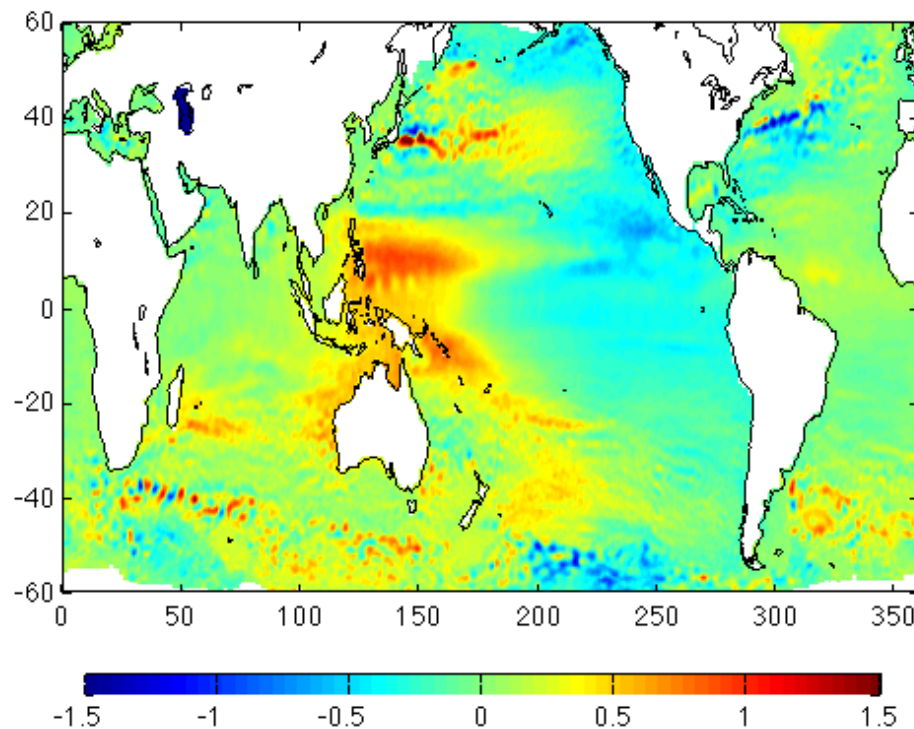


Figure 4. Trend pattern from the 1993-2012 AVISO record. An average spatial trend of 0.26 has been removed. All units in cm/yr.

3.2.2 Synthetic Tide Gauge Datasets

Synthetic tide gauge datasets are grid points in the AVISO dataset nearest to actual tide gauge locations from the Permanent Service for Mean Sea Level (PSMSL; <http://www.psmsl.org>). Only revised local reference (RLR) tide gauge locations with significant record length were taken into account, which resulted in a total of 412 separate locations since 1900 (Figure 5). More detailed discussions of tide gauge selection can be found in *CW2004* and *H2011*. As with the training dataset, seasonal cycles were removed from the tide gauge data so as not to reproduce well resolved annual and semi-annual signals. However, unlike the training dataset, linear trend signals are retained allowing the reconstructions to capture regional and global trends.

Reconstructions were created using all 412 synthetic tide gauges, as well as with subsets of tide gauges at decadal intervals. To look at the effects of using different tide gauge distributions, subsets were taken from each decade from 1900 onward. If a tide gauge produced data for a majority of a decade, then the corresponding grid point became a synthetic gauge for that decade's subset. As can be seen in Figure 5, the number of available in-situ measurements through tide gauges varies significantly over the past century, with fewer than 100 stations prior to 1940 and more than 300 in the 1990s.

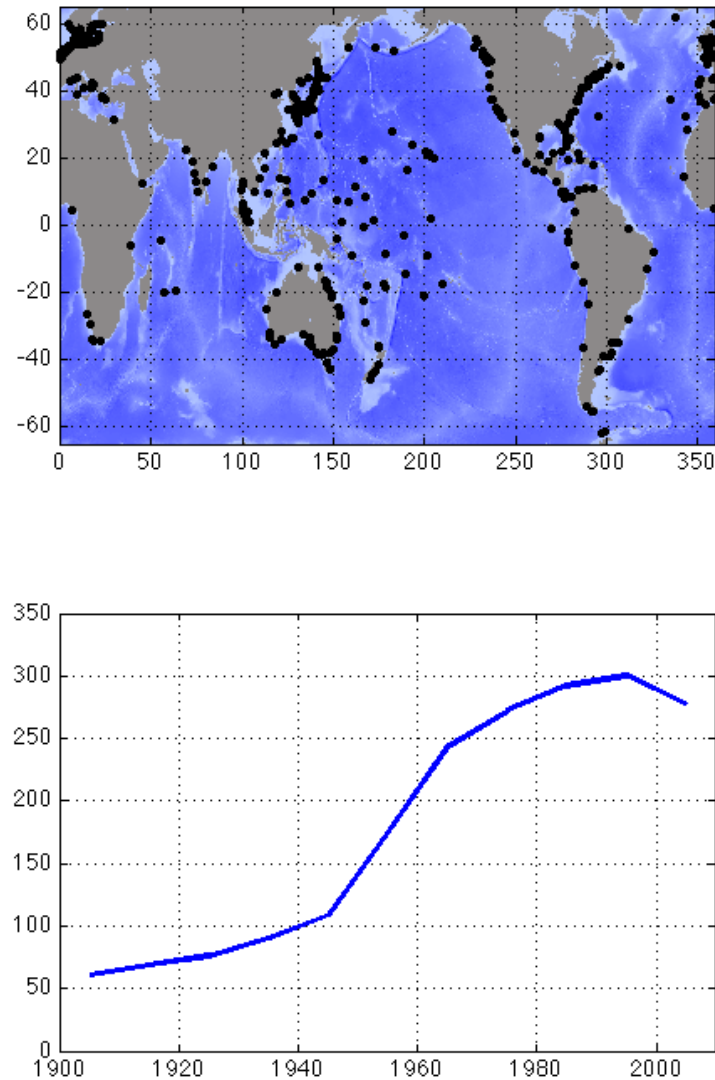


Figure 5. Spatial distribution of all historical tide gauges used (top) and number of available tide gauges during a given decade (bottom).

Using tide gauges distributions that are more extreme allows investigation into less realistic, but equally interesting scenarios. To achieve this, 410 synthetic tide gauges were created on an equal grid of around 9° . On the other end of the distribution spectrum, the complete historical tide gauge set of 412 was altered to remove all tide gauges from the ocean centers, leaving 342 tide gauges. Additionally, to measure hemispherical bias, equal grids of synthetic tide gauges

were created in the northern and southern hemispheres as well. In an effort to keep the total number of tide gauges similar, the northern hemisphere set has 411 gauges with a spacing of 6° and the southern hemisphere set has 393 gauges with a spacing of 7° . Maps of each of these distributions are shown in Figure 6.

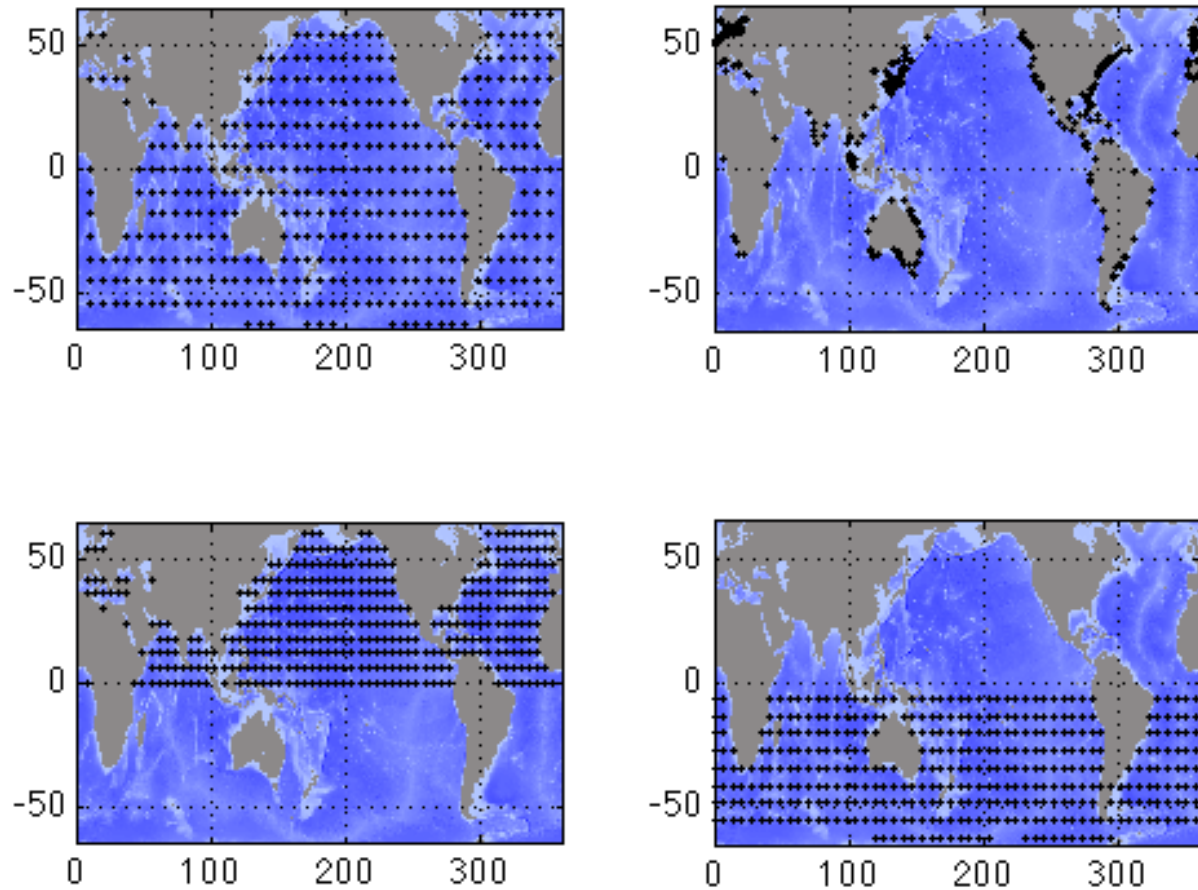


Figure 6. Additional synthetic tide gauge locations: ideal grid (upper left), basin edges only (upper right), northern hemisphere grid (lower left), southern hemisphere grid (lower right).

Additionally, to investigate more realistic tide gauge time series, noise was added to the synthetic tide gauge dataset. Noise was estimated by removing the mean of the monthly tide gauge measurements and performing a 3 month high-pass

filter. This was found by removing a 3-month running mean from the tide gauge data, and resulted in a zero-mean signal with an average standard deviation of 2.8 cm. These noisy time series were then randomly shifted and added to the synthetic tide gauge time series. The magnitude of noise agrees well with that used by *van Onselen* [2000] to create simulated tide gauge signals in a study of the effects of tide gauge data quality on detecting sea-level height variations.

3.2.3 Ocean Parameter/Index Calculations

Five different parameters are used to quantify the ability of a reconstruction to reproduce observed ocean signals. The first is latitude weighted Global Mean Sea Level (GMSL) with a mean trend of ~ 3.2 mm/yr removed, and the remaining four are sea surface height (SSH) equivalents of common ocean indices typically calculated with sea surface temperature (SST): Pacific Decadal Oscillation (PDO), Atlantic Multidecadal Oscillation (AMO), Nino3, and Nino4. To calculate these indices, sea level from the training or reconstruction datasets was latitude weighted and averaged in the areas associated with AMO [Kerr, 2000], Niño3, and Niño4 [Stenseth, et al., 2003]. In the case of PDO, the leading principal component from sea level in the Northern Pacific PDO region is used [Stenseth, et al., 2003; Cummings et al., 2005]. Although PDO and AMO are indices for signals with a longer period than the timespan of this reconstruction, they were chosen because they are well known and still serve to show reconstruction accuracy in critical regions, albeit on shorter time scales.

3.2.4 Reconstruction Assumptions

Given that the specific purpose of this work is to compare EOF and CSEOF reconstruction methods in an idealized setting and not necessarily to create the most accurate reconstructions possible, a number of assumptions have been made for clarity and ease of calculation. For instance, a weighting scheme to account for areas with higher densities of tide gauges is not applied in the reconstruction process. Additionally, it is assumed that the synthetic tide gauges behave similarly to actual tide gauges with respect to variability in the open ocean. Because synthetic tide gauges are at distances of around 30 km from the coast and come from the training dataset, our assumption is debatable. For comparison purposes, however, synthetic tide gauges sampled in this manner are assumed to be realistic enough for evaluation of the two techniques. Similarly, this process differs from true sea level reconstruction in that the global dataset training period spans the entire tide gauge period. This would defeat the purpose of creating a useable reconstruction, but in this case allows for validation of reconstructions with the calibration dataset over the entire time period. For the purpose of comparison, all reconstructions are made with basis functions that contain 70% of the training dataset variance, with the exception of those discussed in Section 3.3.4. Objective methods of determining the number of modes to retain while avoiding over fitting do exist [CW2004; H2011] but were not considered in the present work because the optimize the reconstruction and would therefore make it more of an apples to

oranges comparison, as each reconstruction would be creating a different percentage of the original variance.

3.3 Results

3.3.1 Decadal Tide Gauge Distributions

The number and distribution of useful tide gauges has varied over the past century (Figure 5), beginning with most of the gauges in the northern hemisphere, especially around Europe, and eventually taking on a more global distribution, including stations located on islands within ocean basins. The role that available tide gauges play on reconstruction quality is difficult to quantify with published reconstructions because of the lack of global data with which to compare prior to the calibration period. *Christiansen et al.* [2010] looked at the effect of tide gauge number on GMSL and found that varying the number of synthetic tide gauges from 20 to 200 improved the reconstructions only slightly. Here, reconstructions are created using both methods, CSEOF and EOF, by fitting to tide gauge distributions from each decade over the past century. Figure 7 shows 20-year trend patterns from reconstructions with 3 different tide gauge distributions: the 1930s, the 1970s, and all available tide gauges. For simplicity, these will be referred to as CR30, CR70, and CRAA, for the CSEOF reconstructions, and ER30, ER70, and ERAA for the EOF reconstructions.

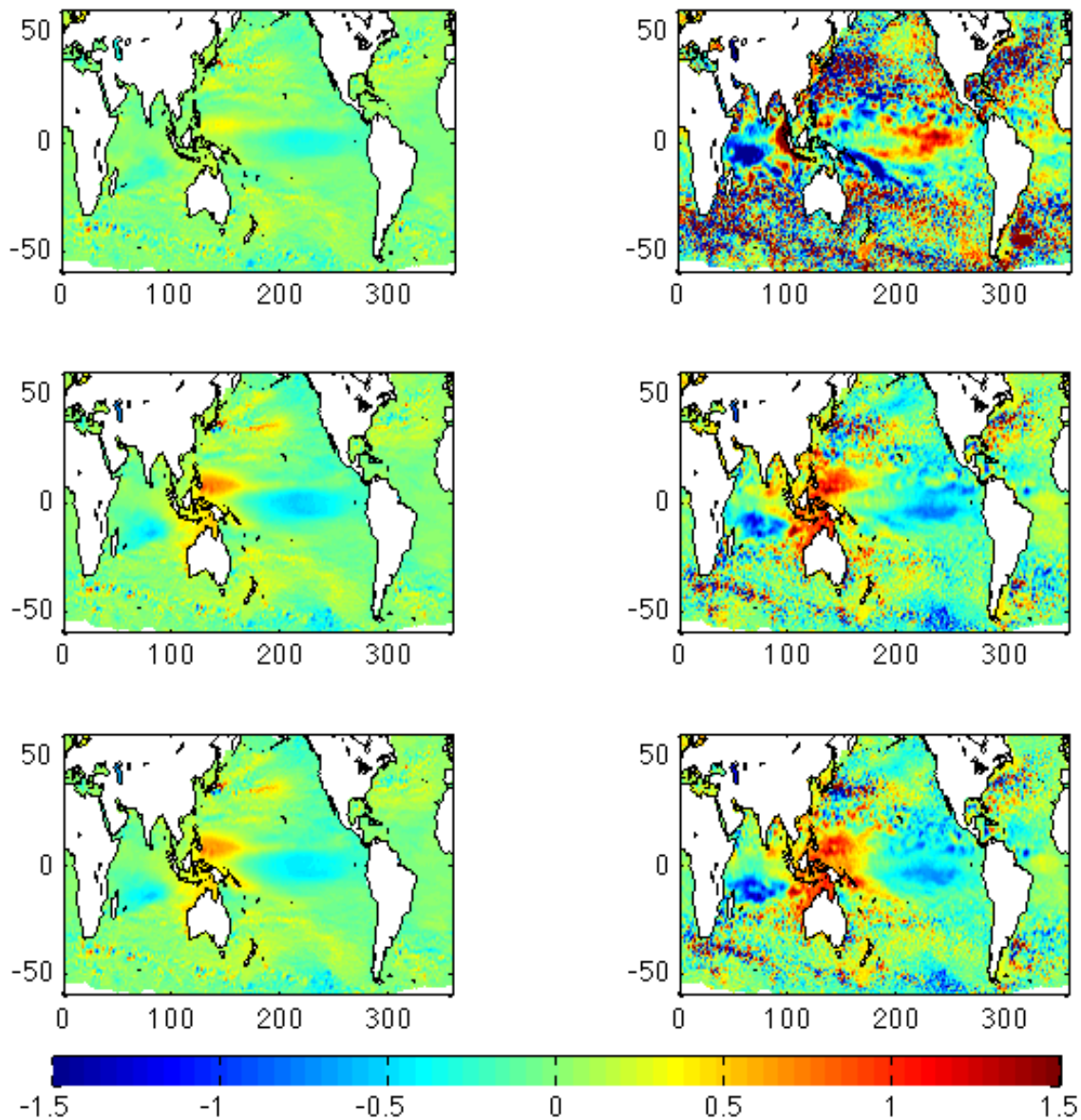


Figure 7. CSEOF reconstruction trend patterns (left column) and EOF Reconstruction trend patterns (right column) calculated with synthetic tide gauge distribution from the 1930's (top row), 1970's (middle row), and all available tide gauges (bottom row). All units in cm/yr.

The left column in Figure 7 shows the regional trends in the CSEOF reconstructions as a function of synthetic tide gauge availability. It can be seen that with CR30, the trends have lower amplitude compared to CR70 and CRAA,

although a similar pattern remains. This is most likely due to a lack of in-situ measurements where regional trends are most prominent, such as the equatorial Pacific, during that time period. CR70 and CRAA are very similar to each other, with slightly lower amplitude in CRAA. When comparing this trend pattern with that of the training data (Figure 4), there is strong agreement with the exception of the southern tropics in the Indian Ocean. It should also be noted that the CSEOF reconstructions, in general, tend to slightly underestimate the regional trend, regardless of the tide gauge distribution.

The right column of Figure 7 shows similar trend patterns for the EOF reconstruction method. In general, these trend maps show much more stochastic signal in high latitudes, generally associated with over fitting. ER30 has very little spatial agreement with ER70 or ERAA. The latter two reconstructions agree in terms of general sea level trend patterns in the tropics (see Figure 4), but show much higher trend in the northern Indian Ocean and at the Indonesian throughflow region, and a negative trend in the southern tropical Indian Ocean. A plausible explanation is the lack of sufficient tide gauge representation in the Indian Ocean.

Although secular trends in GMSL were not considered in this work, interannual to decadal variability in GMSL has become a favored area of research [Chambers *et al.*, 2012; Hamlington *et al.*, 2013]. Figure 8 shows a GMSL comparison with the detrended training data and reconstructions calculated using all available and the 1930s tide gauge distributions. For clearer representation, all

weekly data used in Figure 8 were smoothed by applying a 3-month moving window.

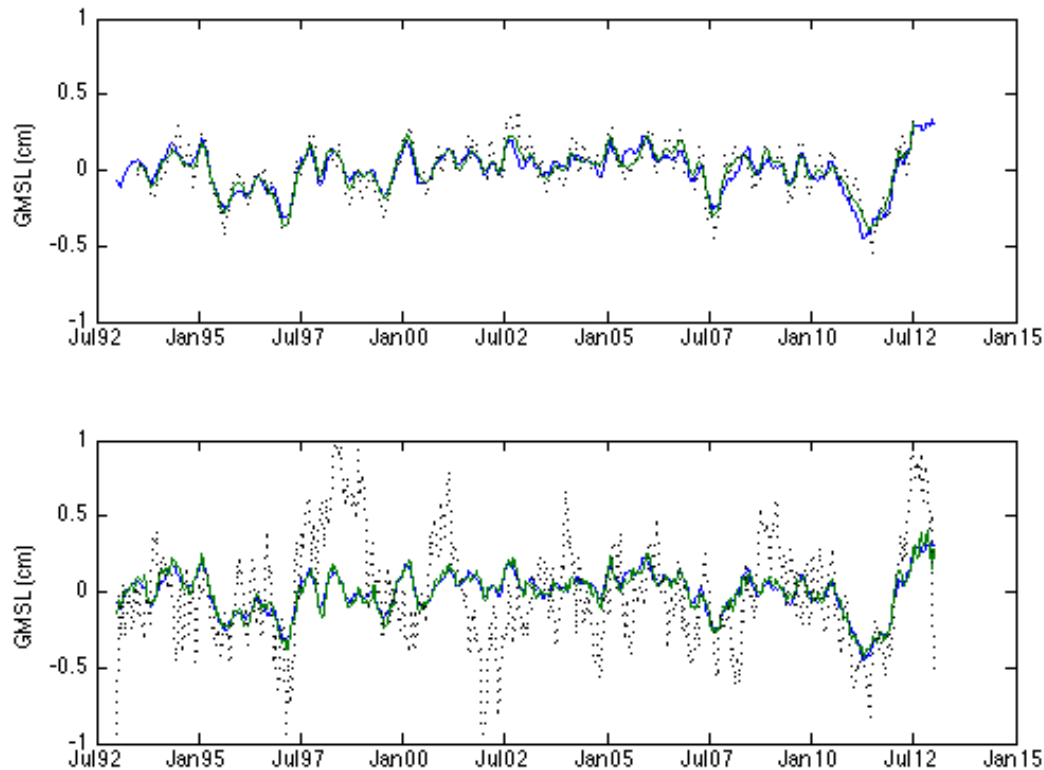


Figure 8. Detrended GMSL from AVISO data (blue) compared to GMSL from CSEOF reconstruction (top) and EOF reconstruction (bottom). Reconstructions with all tide gauge records are depicted by solid lines, while reconstructions with 1930's tide gauge records are depicted by dotted lines. Note: All GMSL data have been smoothed by a 3-month moving average for clarity.

The CSEOF reconstructions agree well with the AVISO GMSL, both in phase and in amplitude. Note that using the lower quality CR30 does increase the amplitude of the GMSL variability slightly. Overall, the average GMSL amplitude from CR30 is 2% lower than that of the training data, while the average amplitude using CRAA is 9% below the training GMSL. There is no discernable difference

between CR70 and CRAA when considering GMSL variability. The correlations associated with the training dataset and CR30, CR70, and CRAA are 0.83, 0.88, and 0.89, respectively. Although there is slight drop off in correlation from the limited tide gauge dataset, these correlations are sufficiently high using sampling from the beginning of the century to suggest that a user could be confident in GMSL derived from a CSEOF reconstruction throughout the 20th century.

Table 1 also shows the correlation between various ocean indices calculated from the CSEOF reconstructions and the indices calculated from the AVISO training data. This further emphasizes the lack of dependence the CSEOF reconstruction method has on tide gauge distribution. With even a significant drop off in the number of tide gauges, such as going from the complete tide gauge distribution to the 1900s distribution, GMSL correlation decreases by less than 13%. In fact, the average decrease in index correlation from the reconstruction where all available tide gauges are used to the reconstruction where the 1900s tide gauge distribution is used is only 6.4%.

Table 1. Correlation between parameters calculated from AVISO training dataset and parameters calculated from various CSEOF reconstructions.

	GMSL	PDO	AMO	Nino3	Nino4
1900s (61 tide gauges)	0.773	0.656	0.850	0.927	0.907
1920s (76 tide gauges)	0.812	0.654	0.868	0.936	0.923
1940s (108 tide gauges)	0.872	0.685	0.902	0.975	0.954
1960s (243 tide gauges)	0.878	0.678	0.907	0.982	0.962
1980s (292 tide gauges)	0.877	0.660	0.912	0.977	0.967
2000s (277 tide gauges)	0.888	0.644	0.911	0.970	0.965
All gauges (412 tide gauges, 70% variance explained with 11 modes)	0.886	0.651	0.911	0.979	0.967
Ideal Grid (410 tide gauges)	0.909	0.628	0.926	0.983	0.977
Basin Edges (342 tide gauges)	0.883	0.655	0.906	0.975	0.957
Northern Hemisphere Grid (411 tide gauges)	0.906	0.635	0.924	0.981	0.971
Southern Hemisphere Grid (393 tide gauges)	0.910	0.657	0.928	0.975	0.979
All gauges with noise	0.886	0.658	0.910	0.977	0.967
All gauges (90% variance explained with 16 modes)	0.953	0.655	0.958	0.984	0.980
All gauges (90% variance) with noise	0.953	0.666	0.957	0.982	0.980
Atlantic Reconstruction	0.905		0.927		
Pacific Reconstruction	0.931	0.621		0.976	0.971

The EOF reconstruction method overestimates GMSL under all tide gauge scenarios, which is in agreement with *Christiansen, et al.* [2010]. When considering ER30, the amplitude overestimation is extreme, nearly 500% on average, as opposed to 30% with ERAA. *Christiansen, et al.* [2010] suggest that this is caused by overemphasizing higher order modes that do not actually contribute to GMSL variability and that more tide gauges curb this overestimation. The correlations associated with the training dataset GMSL and that from ER30, ER70, and ERAA are 0.20, 0.66, and 0.72, respectively. Table 2 is similar to Table 1 but pertains to

the EOF reconstructions. EOF reconstructions show a significant degradation of signal when working with limited tide gauge distributions. The average decrease in correlation across all indices from the reconstruction with complete tide gauge dataset to the reconstruction with the 1900s distribution is 88.0%. This analysis suggests that the accuracy of an EOF reconstruction could be significantly degraded using historical tide gauge distributions before 1950, and care should be taken with time-varying tide gauge distributions when reconstructing sea level.

Table 2. Correlation between parameters calculated from AVISO training dataset and parameters calculated from various EOF reconstructions.

	GMSL	PDO	AMO	Nino3	Nino4
1900s (61 tide gauges)	0.112	0.018	0.095	0.226	0.042
1920s (76 tide gauges)	0.077	0.131	0.172	0.150	0.036
1940s (108 tide gauges)	0.059	0.019	0.138	0.115	0.045
1960s (243 tide gauges)	0.642	0.449	0.663	0.925	0.896
1980s (292 tide gauges)	0.710	0.498	0.729	0.947	0.958
2000s (277 tide gauges)	0.666	0.480	0.722	0.898	0.909
All gauges (412 tide gauges, 70% variance explained with 108 modes)	0.716	0.519	0.765	0.950	0.970
Ideal Grid (410 tide gauges)	0.883	0.578	0.886	0.991	0.981
Basin Edges (342 tide gauges)	0.635	0.451	0.686	0.851	0.656
Northern Hemisphere Grid (411 tide gauges)	0.874	0.595	0.906	0.992	0.990
Southern Hemisphere Grid (393 tide gauges)	0.853	0.554	0.856	0.953	0.914
All gauges with noise	0.689	0.467	0.701	0.935	0.953
All gauges (90% variance explained with 237 modes)	0.811	0.534	0.817	0.953	0.973
All gauges (90% variance) with noise	0.684	0.418	0.556	0.887	0.943
Atlantic Reconstruction	0.550		0.624		
Pacific Reconstruction	0.682	0.406		0.928	0.959

When considering reconstructions with all available tide gauges, additional observations from Table 1 and Table 2 can be made. Variability in the Nino regions is captured very well using both methods of reconstruction. GMSL and AMO are in the reconstructions, but not as well reproduced as the more prominent equatorial (Nino) signals. Additionally, the fact that the PDO region is not area averaged, which has an inherent spatial smoothing in the other indices, allows much more high frequency signal to remain in the computed EOF, reducing the correlation. Lastly, it should be noted that in this idealized case, reconstructing regionally does not improve the ability to capture the indices tested here.

3.3.2 Experimental Tide Gauge Locations

Idealistic tide gauge distributions were used to make reconstructions under extreme circumstances, as shown in Figure 6. These distributions represent the ideal case, where there is uniform spacing over the entire ocean (without accounting for latitude weighting); the limited case of only having in-situ measurements along the edge of basins, and the cases of pronounced hemispheric clustering. To see how reconstructions vary with these very different tide gauge distributions, correlation between the reconstructions and training data, and relative amplitude are calculated at each grid point. As in *Christiansen et al.* [2010], the relative amplitude is calculated as $(\sigma_{\text{rec}} - \sigma_{\text{AVISO}})/\sigma_{\text{AVISO}}$, where σ_{rec} and σ_{AVISO} are the standard deviations of each grid point in the reconstruction and AVISO datasets, respectively. Ideal relative amplitude has a value of 0, with negative values

showing underestimation by the reconstruction and positive values showing overestimation.

The correlation and relative amplitudes of the CSEOF reconstructions using both the global ideal grid distribution and the basin edge distribution are shown in Figure 9. The correlation and relative amplitude are virtually unchanged with the edge distribution, supporting the argument that the CSEOF method of reconstruction has very little sensitivity to tide gauge distribution, as was found when looking at historical distributions. In general, correlations between the reconstruction and training data are very good, and relative amplitude is slightly lower, but nearly equal for both tide gauge distributions. Table 1 reinforces this agreement, showing that correlation changes very little regardless of which experimental tide gauge distribution is used. This goes against reconstruction intuition, particularly for the edge-only scenario.

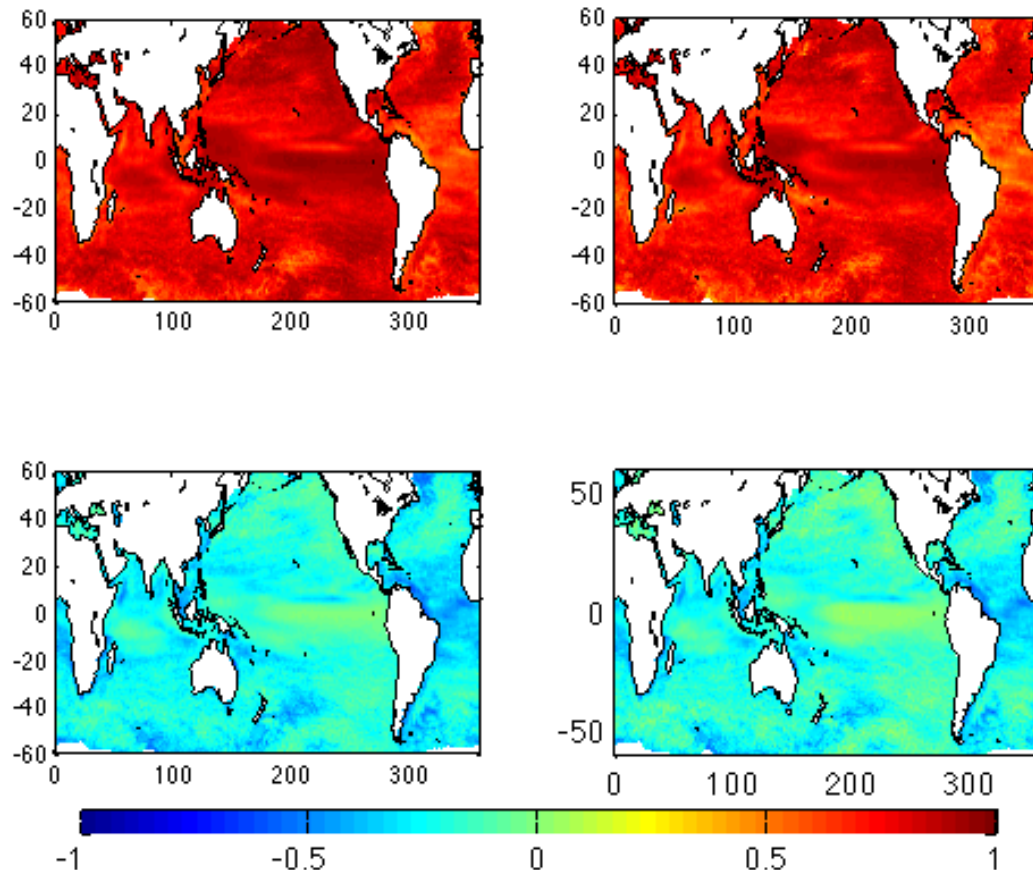


Figure 9. CSEOF reconstruction with ideal grid tide gauge distribution (left column) and CSEOF reconstruction with edge tide gauge distribution (right column) correlations (top row), and relative amplitudes (bottom row). Note: ideal relative amplitude is 0.

Correlation and relative amplitude maps created from AVISO and EOF reconstructions using the ideal grid and edge-only tide gauge distributions are shown in Figure 10. It can be seen that there is much higher correlation and much more reasonable relative amplitude when using the ideally gridded tide gauges as opposed to those located only on the edges of the oceans. In the edge-only EOF reconstruction, correlation is highest and relative amplitude is nearest zero in proximity to the coast and in the Pacific equatorial, as one might expect. Table 2 further illustrates these points, showing that correlations between the training data

and EOF reconstructions' common indices vary much more. For example, correlations of GMSL for ideal grid, and edge only tide gauge distributions are 0.883, and 0.635, respectively. This is a range of nearly 0.25, which is 10 times larger than that seen with CSEOF reconstructions.

Another interesting observation to note is that reconstructions created using grids limited to only one hemisphere perform relatively well regardless of basis function methodology. Two conclusions may be inferred from this observation: avoiding tide gauge clustering is not necessarily a priority when selecting tide gauges for reconstruction; the oceanic signals associated with the indices used have a presence in both hemispheres.

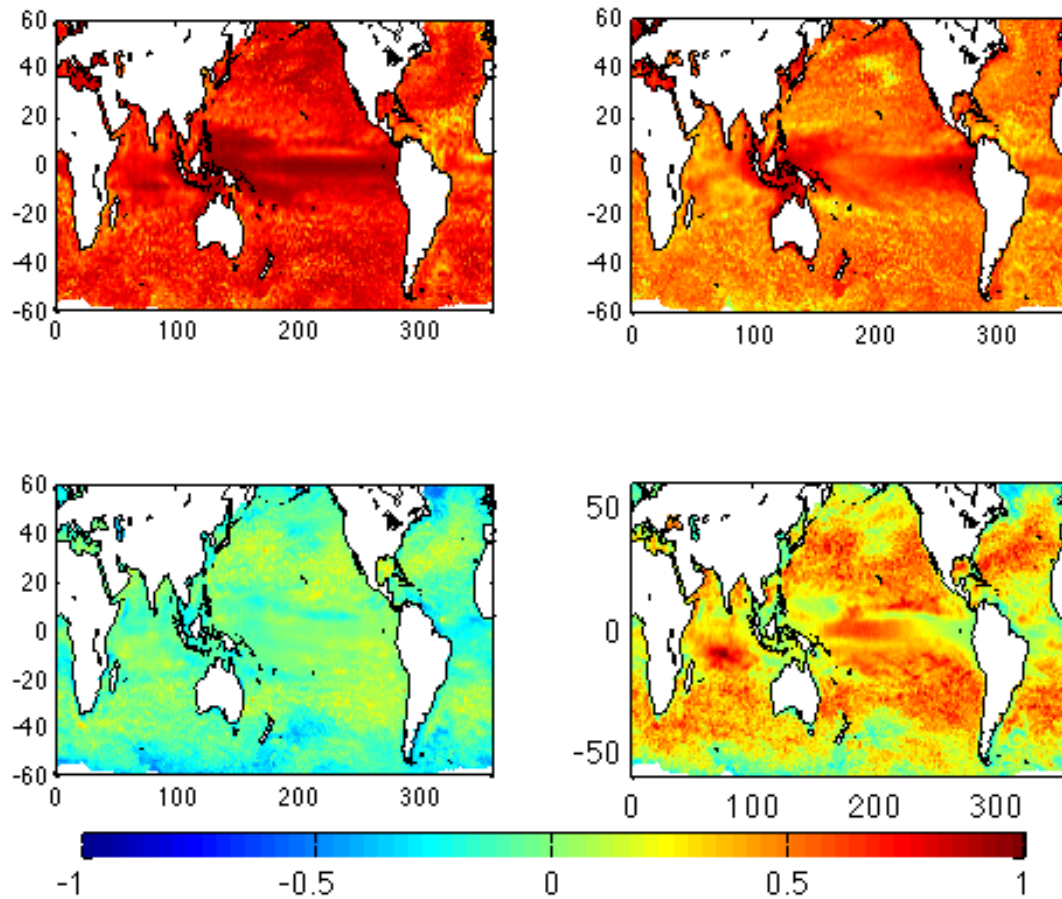


Figure 10. Identical to Figure 9 for EOF reconstructions.

3.3.3 Noise in the Tide Gauge Records

To investigate how more realistic tide gauge measurements would affect reconstruction quality, actual tide gauge data were processed as described in Section 3.2.2 to estimate a realistic noise signal that could be added to the synthetic tide gauge time series. Reconstructions were created with the noisy, synthetic tide gauge dataset to be compared to those reconstructions with the complete synthetic tide gauge dataset and the training dataset.

Figure 11 shows trend, correlation, and relative amplitude maps for CSEOF reconstructions created from all available tide gauges (the full historical distribution) with and without added noise. There is no discernable difference in the maps when adding noise to the tide gauge datasets. Table 1 shows that the correlation associated with the PDO, AMO and Nino3 changes only slightly when adding tide gauge noise. The lack of sensitivity to added noise in the CSEOF reconstruction is due to the use of tide gauge data at multiple (52) time steps when computing the amplitude of CSEOF loading vectors, which effectively smooths the time varying random noise within the temporal window during the fitting process. Figure 11 shows that correlation is generally quite high, particularly as the equatorial Pacific. There are certain areas, such as the Central Atlantic where agreement is not as good. This is most likely due to lack of sufficient in-situ representation in that region. As for the relative amplitude, it should be noted the reconstructions are very close to the satellite altimetry data in amplitude or slightly underestimate it with the exception of the equatorial central to western Pacific; this is in agreement with the GMSL results from Figure 8.

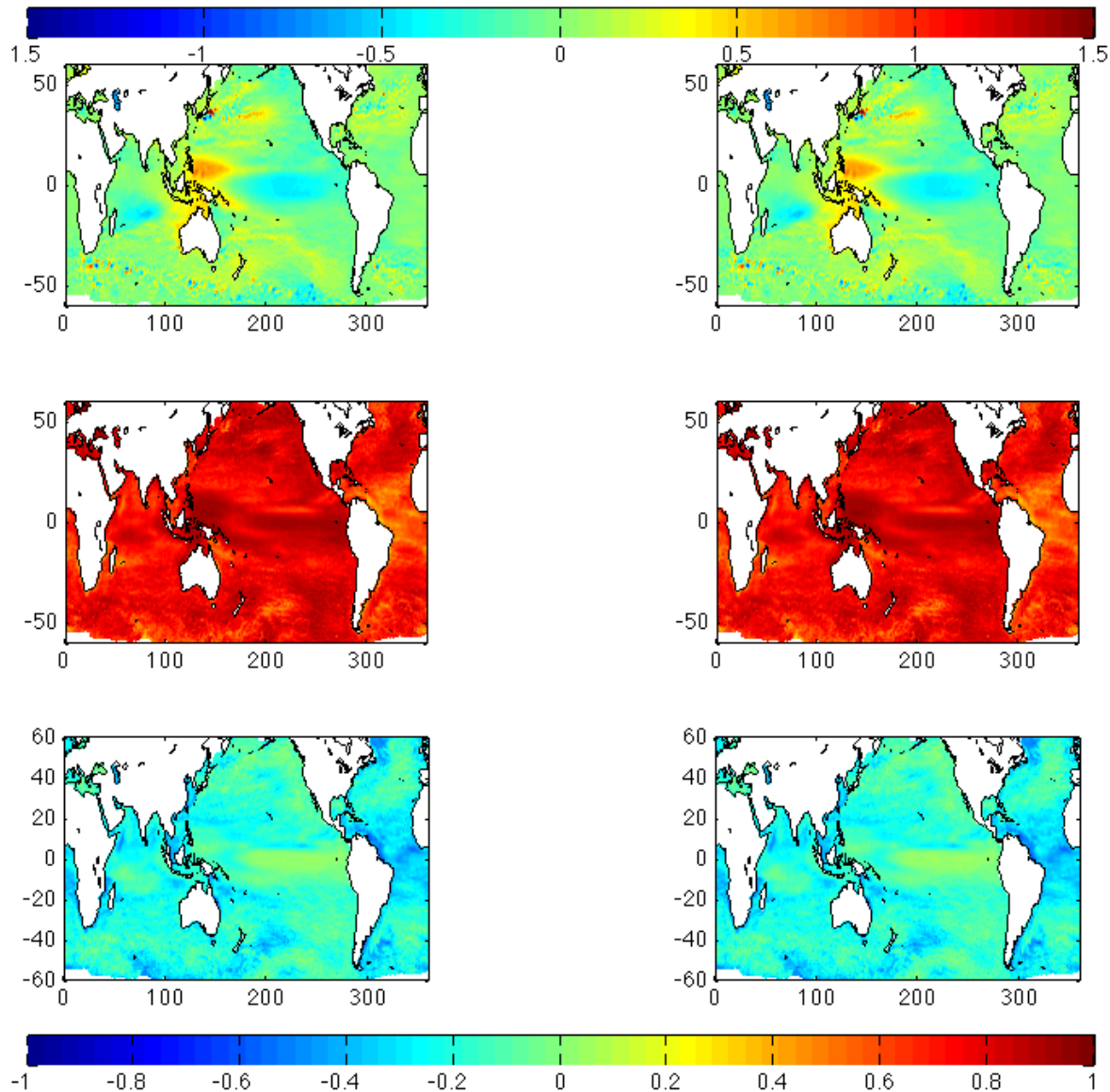


Figure 11. CSEOF reconstruction (left column) and CSEOF reconstruction with tide gauge noise (right column) trend maps (top row), correlations (middle row), and relative amplitudes (bottom row). Note: the top colorbar (in cm/yr) is associated with the top row, while the bottom colorbar is associated with the middle and bottom rows; ideal relative amplitude has a value of 0.

A similar plot for the EOF method (Figure 12) shows that the trend maps computed from EOF reconstructions with and without noise, agree quite well; however, the correlation decreases and relative amplitude is overestimated

significantly over the tropics and mid-latitude regions. These results are consistent with or without added noise. Table 2 shows that the correlation of all indices decreases when adding realistic noise to the ideal simulated tide gauge data. Although the correlation changes are less than 0.07, they are an order of magnitude larger than that seen in the CSEOF reconstructions. Similar to the CSEOF correlation and amplitude maps, the EOF maps show that the reconstructions agree with AVISO well in the Equatorial Pacific. However, outside of that region, correlations are generally much lower than seen with the CSEOF method. Also, the relative amplitude map shows that outside the Pacific and high latitude regions, the reconstructions generally overestimate sea level signals. Again, this agrees with what was seen in the GMSL analysis (Figure 8).

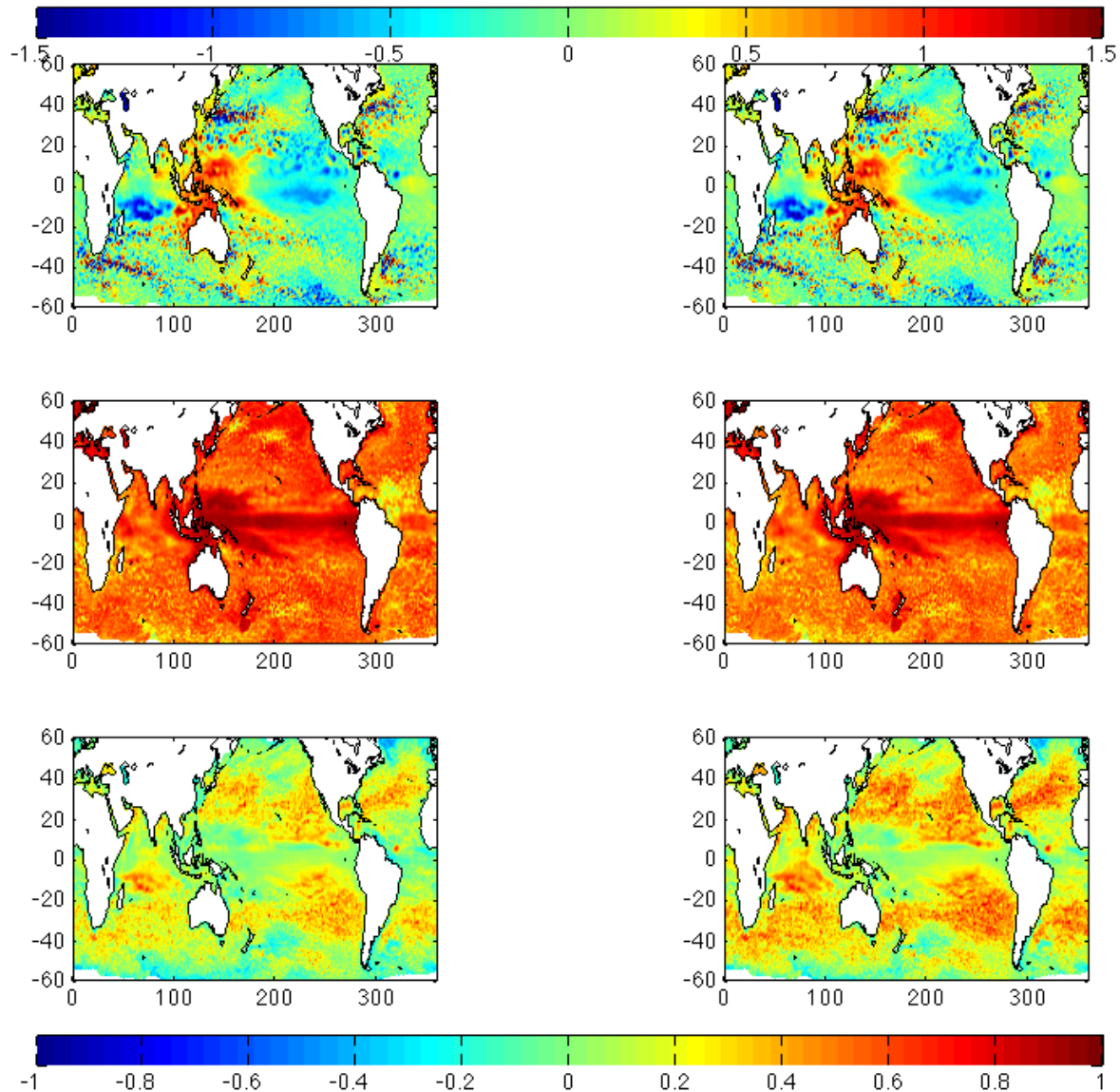


Figure 12. EOF reconstruction (left column) and EOF reconstruction with tide gauge noise (right column) trend maps (top row), correlations (middle row), and relative amplitudes (bottom row).

GMSL was calculated using reconstructions from both basis function methods with and without the addition of tide gauge noise. This is plotted along side the detrended AVISO GMSL with seasonal signal removed (Figure 13). The GMSLs from the CSEOF reconstructions agree very well with the GMSL from AVISO, and

adding tide gauge noise does not alter the reconstruction in any visible way. Overall, it increases the average amplitude underestimation by 1% to a total of 9% below the training data GMSL magnitude. This underestimation may be natural since only a small number of CSEOF modes are used for reconstruction. Adding more modes may decrease amplitude underestimation. The EOF GMSL signal has more stochasticity than the training data GMSL. Note that adding noise to the synthetic tide gauges increases the signal overestimation slightly (from 30% to 35%), although not nearly as much as using sparse tide gauge distributions (Figure 8). Comparing the relative amplitude maps indicates that the CSEOF (EOF) method tends to underestimate (overestimate) the true signal. To confirm these results, this analysis was also performed using random white noise with a standard deviation of 2.8 cm. Although the effects were smaller, the findings were confirmed.

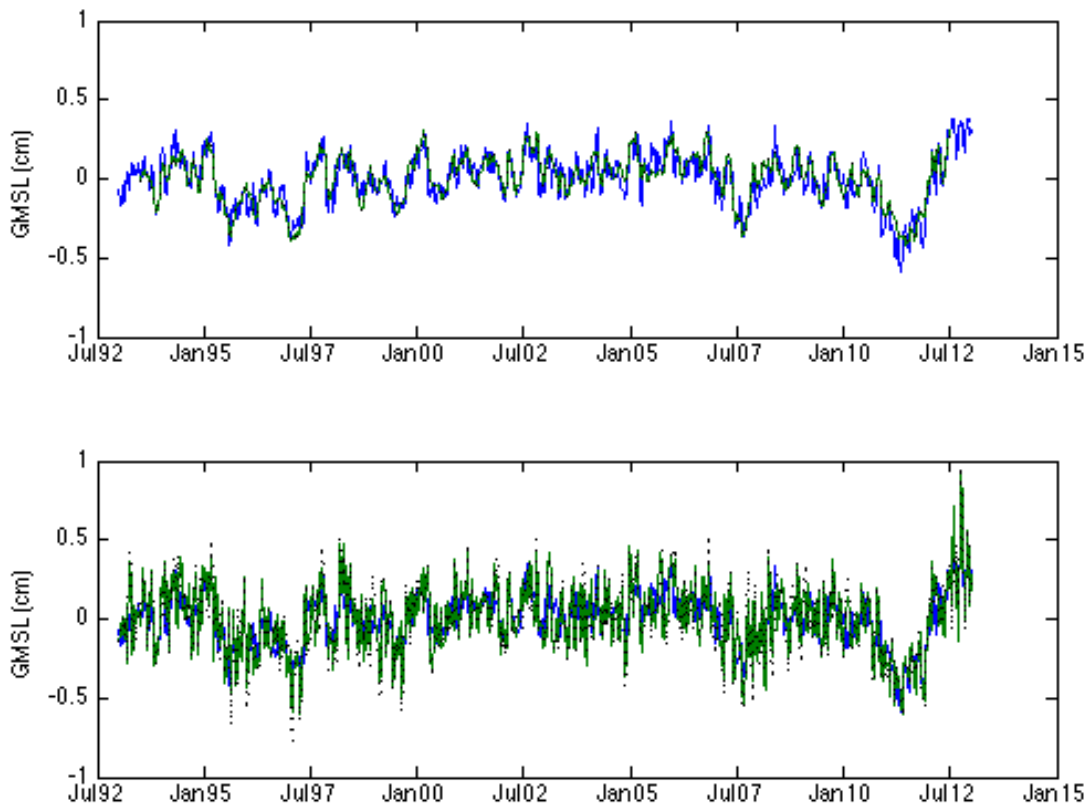


Figure 13. Detrended GMSL from AVISO (blue) data compared to GMSL from CSEOF reconstruction (top) and EOF reconstruction (bottom). Reconstructions with noisy tide gauge records are depicted by dotted lines.

3.3.4 Selected Variance

Before creating any reconstruction, the question of how much variance should be kept in the basis functions must be answered. *CW2004* kept over 80% (using 20 EOF modes) not including the seasonal cycle in their $1^{\circ} \times 1^{\circ}$ monthly reconstruction, and *H2011* kept over 95% (using 19 CSEOF modes) including the seasonal cycle with a $0.5^{\circ} \times 0.5^{\circ}$ weekly reconstruction. In order to create the reconstructions with 70% of the original variance, 108 EOF modes were required, whereas only 11

CSEOF modes were needed. For comparison, reconstructions were also created using 90% of the original variance. In this case, 237 EOF modes and 16 CSEOF modes were required.

Figure 14 shows the trend patterns associated with the reconstructions created using the previously explained tide gauge distributions and basis functions containing 90% variance. When comparing to Figure 7, the CSEOF trend maps are essentially unchanged regardless of whether 70% or 90% of the original variance is used. Correlations with the ocean indices calculated from the training data (Table 1) show very slight improvements (~1%) for the PDO and the Niño indices, while the GMSL and AMO correlation improved by 8% and 5%, respectively, when increasing the variance explained from 70% to 90%. These results are for all available tide gauges and valid using both the standard and noisy tide gauge datasets. These increased correlations are due to more accurate reconstruction in areas with less dominant variability, such as the North Atlantic.

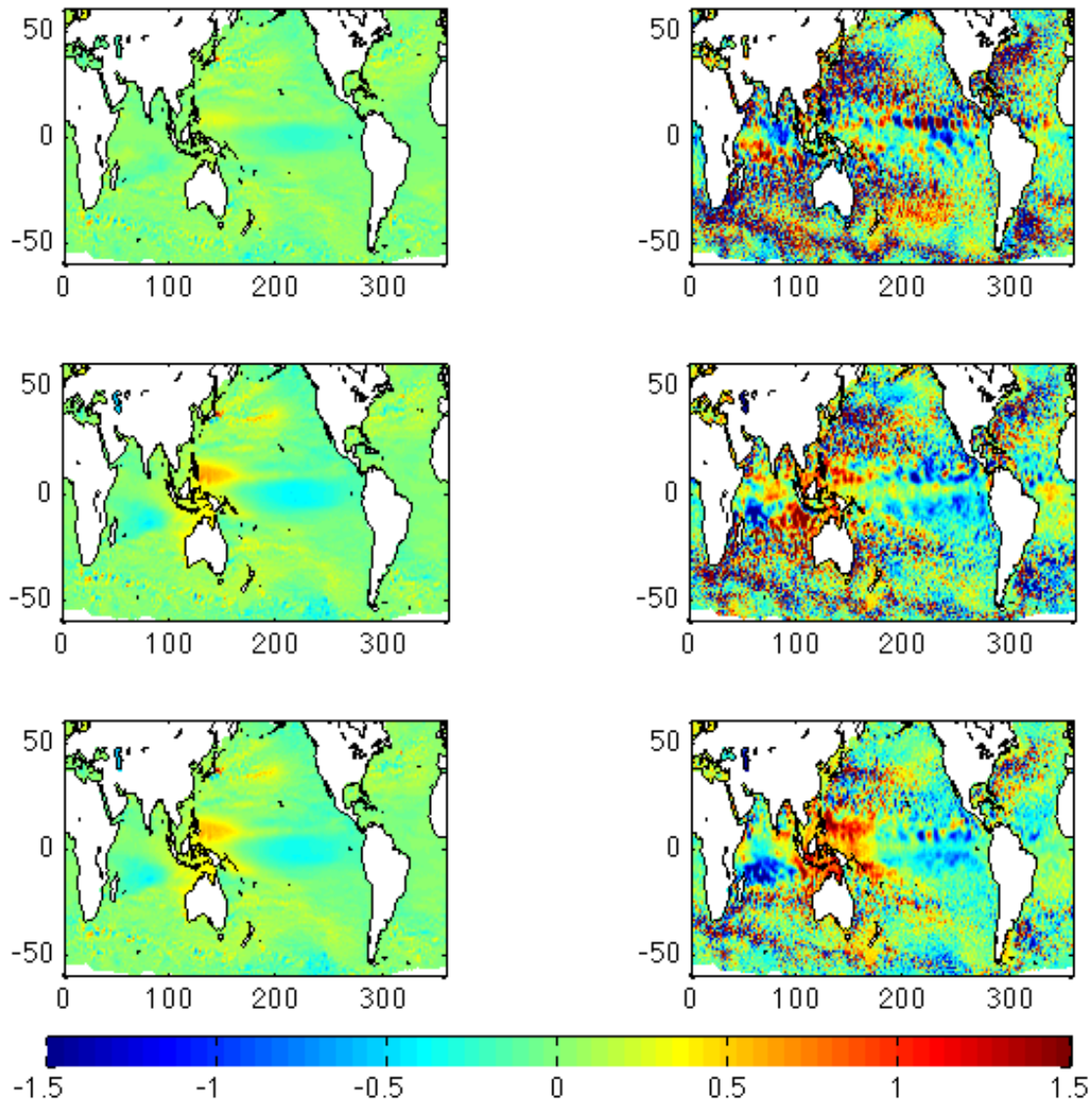


Figure 14. Similar to Figure 7 with 90% of the decomposed variance remaining in the reconstructions. Colorbar units are cm/yr.

Similar observations can be made with the EOF reconstructions. In this case, it can be seen that the trend maps differ significantly when using 70% or 90% of the variance. When comparing Figure 14 to Figure 7, some key observations about using more variance can be inferred: for ER30, the amount of noise is similar but some of the dominant equatorial features are lost; for ER70, the trend map

becomes much noisier, including the main equatorial features; for ERAA, the amount of noise increases moderately and the features change slightly. In all cases, the peak amplitudes increase on top of the existing overestimation. This suggests that too much variability was kept in the basis functions, causing over fitting of the synthetic tide gauge records.

When comparing the index correlations from the 70% variance, non-noisy, full tide gauge reconstruction in Table 2 to similar correlations with a 90% variance reconstruction, conclusions similar to the CSEOF conclusions can be made. With more variance, correlations of PDO and Niño indices increase by 3% and less than 1%, respectively. GMSL correlation increases by 13%, and AMO correlation increases by 7%. However, when considering noisy tide gauges, the reconstruction with more variance has less correlation with all of the chosen indices. GMSL, PDO, AMO, Niño3, and Niño4 correlations decrease by 5%, 19%, 27%, 7%, and 3%, respectively, when reconstructing with 90% of the total variance as opposed to 70%.

3.3.5 Creating EOF Reconstructions Using EOF0

As mentioned in Chapter 2, a common practice when creating EOF reconstructions [CW2004; Christiansen, 2010] is to include a mode of 1's (also known as EOF0), which is the addition of a homogeneous loading vector (LV) before all of the other modes prior to tide gauge fitting. This captures much of the long-term trend in a single mode. In order to accomplish this without inaccurately redistributing sea level in other locations, all LVs besides EOF0 must be demeaned and normalized prior to reconstructing.

To further this comparison, EOF reconstructions including the EOF0 method were created under many of the previous tide gauge scenarios. Table 3 shows the correlation between indices calculated from the AVISO training dataset and these EOF reconstructions. Note that the reconstructions using the experimental tide gauge distributions were not created using an EOF0. The correlation values in Table 3 are slightly lower, but similar to those seen with the EOF reconstructions not including EOF0 (Table 2), with the exception of detrended GMSL. There is an average decrease in GMSL correlation of 41% when using EOF0.

Table 3. Correlation between parameters calculated from AVISO training dataset and parameters calculated from various EOF reconstructions using EOF0.

	GMSL	PDO	AMO	Nino3	Nino4
1900s (61 tide gauges)	0.011	0.050	0.048	0.085	-0.017
1920s (76 tide gauges)	0.082	0.206	0.132	-0.092	0.010
1940s (108 tide gauges)	0.032	0.001	0.101	0.115	0.043
1960s (243 tide gauges)	0.337	0.418	0.611	0.923	0.893
1980s (292 tide gauges)	0.376	0.489	0.633	0.943	0.958
2000s (277 tide gauges)	0.400	0.472	0.661	0.900	0.907
All gauges (412 tide gauges, 70% variance explained with 108 modes)	0.465	0.522	0.709	0.948	0.967
All gauges with noise	0.419	0.469	0.641	0.932	0.953
All gauges (90% variance explained with 237 modes)	0.543	0.530	0.776	0.951	0.974
All gauges (90% variance) with noise	0.401	0.403	0.531	0.886	0.946

To investigate this further, Figure 15 shows detrended GMSL from AVISO, the EOF reconstruction with all gauges, and the EOF reconstruction with EOF0 and all gauges (similar to Figure 8 and Figure 13). Including EOF0 greatly

decreases the skill of reconstructing inter-annual to multi-decadal variability in GMSL. This is shown by vast overestimation of amplitude, and phase mismatch in Figure 15. The ability to capture climate signals in GMSL as well as regional trends is lost when including an EOF0 because the spatial mean of the remaining EOFs is removed prior to tide gauge interpolation.

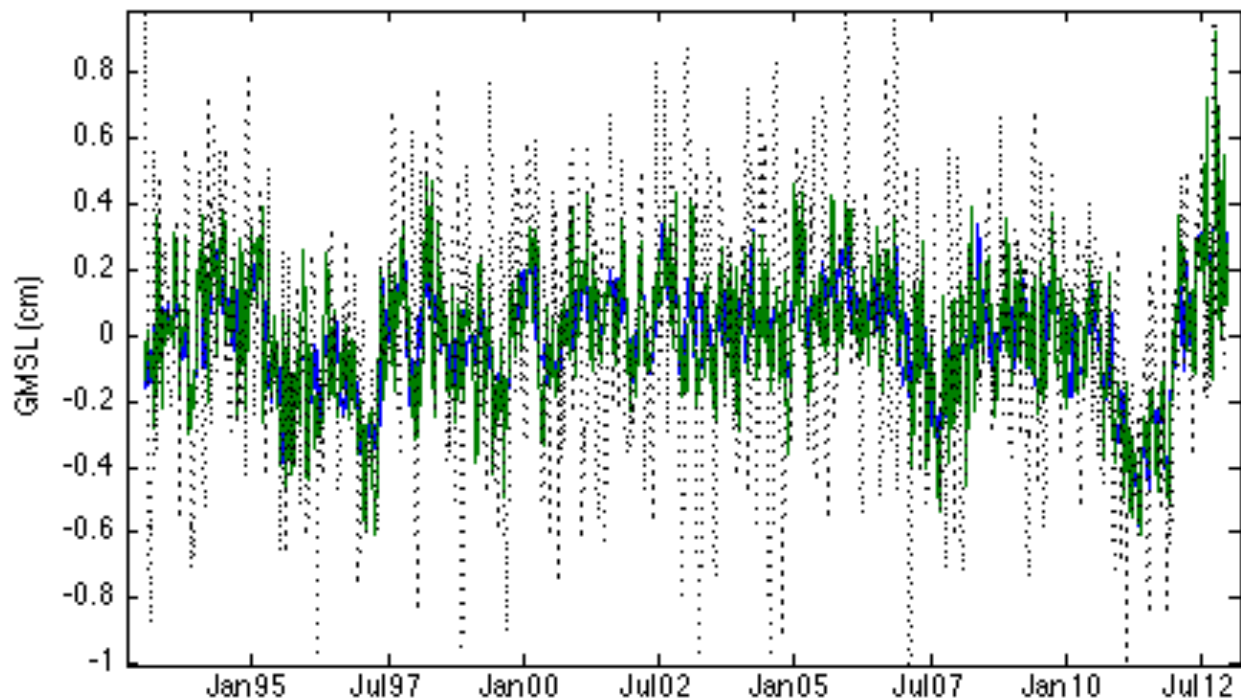


Figure 15. Detrended GMSL from AVISO (blue) data compared to GMSL from EOF reconstruction without EOF0 (green) and EOF reconstruction with EOF0 (dotted).

3.3.6 Reconstructing the Pacific and Atlantic

Reconstructions were created for the Pacific and Atlantic Oceans by trimming the training data and synthetic tide gauge locations to only include points within a given basin. Figure 16 shows the trend maps from these reconstructions over the

entire 20-year period. These figures can be viewed in comparison to trend patterns in the AVISO training data (Figure 4), and trend patterns from the full reconstructions (Figure 7). The Atlantic CSEOF reconstruction does not capture trends quite as well as the global CSEOF reconstruction, while the trends in the Atlantic EOF reconstruction seem to be more accurate than with the global reconstruction. When considering the Pacific Ocean, it seems the trends from both reconstructions improve with the regional method. The CSEOF reconstruction is closer in amplitude to the training data, while the EOF reconstruction resembles the pattern more closely.

The correlations with corresponding indices for each regional reconstruction are shown in Table 1 and Table 2. For this analysis, GMSL is considered the mean sea level across an entire ocean, as opposed to globally. For the CSEOF reconstructions, reconstructing an ocean at a time shows slight improvement with all indices with the exception of PDO. The GMSL correlations from the global CSEOF reconstruction with all tide gauges were found to be 0.919 for the Pacific and 0.887 for the Atlantic. For the global EOF reconstructions, correlation with GMSL was found to be 0.783 for the Pacific and 0.777 for the Atlantic, meaning that there is a significant decrease in the ability to reconstruct basin-wide mean sea level when using reconstructions formed with only one ocean. Using the EOF method, there are also rather significant decreases in the correlation of PDO and AMO and slight decreases in ENSO correlation with the regional reconstruction technique. In general, an argument can be made that regional reconstructions

slightly improve the quality of CSEOF reconstructions, while degrade EOF reconstructions when considering ocean signals. However, there is no clear argument can be made when considering regional trends.

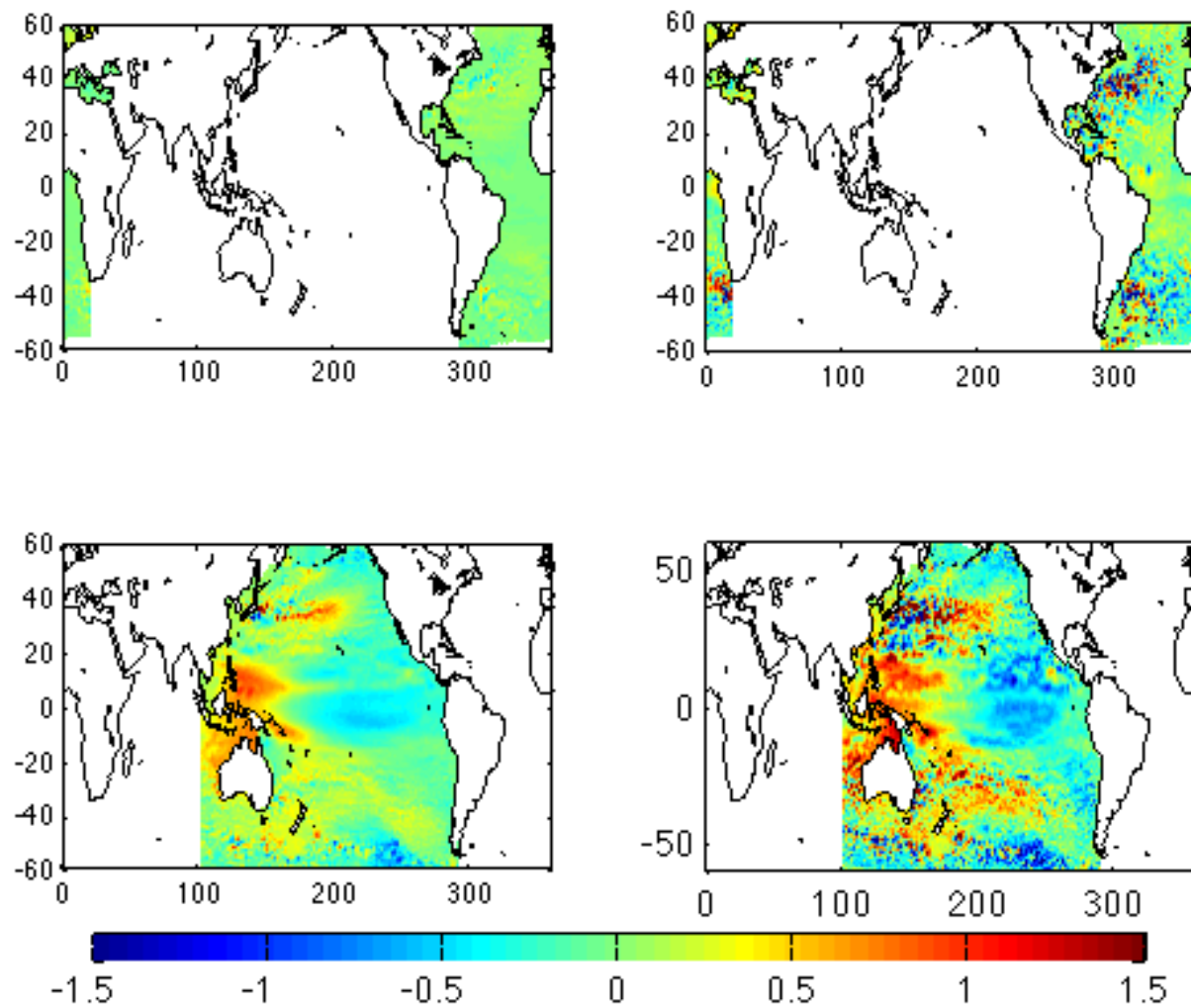


Figure 16. CSEOF reconstruction trend patterns (left column) and EOF Reconstruction trend patterns (right column) calculated in the Atlantic Ocean (top row) and the Pacific Ocean (bottom row). All units in cm/yr.

3.4 Conclusions and Discussion

Sea level reconstructions have proven useful in a wide variety of scientific applications, from studying GMSL trends to examining modulations of the annual cycle. It has, however, proven difficult to verify the accuracy of reconstructions prior to the era of satellite altimetry. One way to verify reconstruction methods is to reconstruct a known dataset, such as the global altimetry dataset. This chapter compares two methods of calculating basis functions for sea level reconstructions. Both EOF and CSEOF decomposition techniques are used to calculate basis functions from a 20-year AVISO satellite altimetry SSH dataset. These basis functions are then fit to a variety of synthetic tide gauge time series to create sea level reconstructions.

For limited tide gauge distributions, such as those found in the early 20th century, the CSEOF reconstruction method is affected far less than the EOF reconstruction method due to the former's ability to capture time varying oscillations, where the latter cannot. Overall, the CSEOF reconstruction accurately reproduces known signals regardless of significant limitations in the tide gauge dataset. However, this method slightly underestimates regional trend amplitudes and global variability. This is due to the use of a small number of CSEOF modes, along with under representation of in-situ measurements in areas with the largest trends. The superior ability to maintain trend patterns and regional variability stems from the temporal connectivity of the LVs attributed to the nested period. This allows CSEOF reconstructions to separate ocean signals, such as wave

oscillations, from regional trends, even with sparse tide gauge locations. Likewise, the lack of effect of noisy tide gauge data on the CSEOF reconstruction stems from a natural temporal averaging created by the windowing of data over the nested period. Similarly, this limits the likelihood of over fitting the data and creates more smoothed reconstructions in general, regardless of original dataset variance or noisy tide gauge records.

The quality of EOF reconstructions decreases far more with limited tide gauge datasets. When considering trend patterns with historical tide gauge distributions, the most limited distributions cause primary features to be lost, noisy spatial patterns to be created, and amplitudes to be overestimated. Trying to reproduce such high temporal and spatial resolution with fixed spatial patterns causes over-emphasis of certain modes, causing vastly overestimated amplitudes in GMSL and in regions without dominant signals (non-equatorial). Additionally, the lack of ability to separate moving periodic signals is portrayed in the reduced correlations between reconstruction calculated and training dataset calculated oceanic indices. Care must be taken when trying to reproduce too much of the original variance with EOF reconstructions, or noise can be reconstructed thereby reducing the quality. Conversely, it is reasonable to reduce the number of EOF modes as the number of tide gauge records decrease to avoid over fitting [*Church and White, 2011*], causing the reconstruction to explain less overall variance as it extends back through time. This issue can be avoided altogether with CSEOF reconstruction.

It can also be seen that the historical tide gauge dataset is not overly limiting compared to a theoretical ideally gridded dataset, and likewise, regional clustering does not appear to drastically alter reconstruction quality. While an argument can be made for using EOF0 in the EOF reconstructions to separate and recreate a global sea level trend, it costs the ability to reproduce inter-annual to multidecadal variations in GMSL. Additionally, breaking the global ocean into basin-sized chunks prior to reconstructing appears to improve the quality of the CSEOF reconstruction slightly, while decreasing the quality of the EOF reconstruction.

Although these results yield great insight into both methods of reconstruction, many assumptions were made, which could be investigated further. For instance, synthetic tide gauges are not necessarily representative of the relationship between real tide gauges and the open ocean. Similar analysis could be done in the future using real tide gauge data. Also, it is doubtful that these results would be as extreme with a calibration dataset of less spatial and temporal resolution. The EOF method could perform better using monthly data or a more sparsely gridded calibration dataset because there would be less “noisy” signal to separate. Lastly, this analysis assumed a constant tide gauge distribution over the entire reconstruction time period, when in reality the number of tide gauges changes frequently. It is unknown whether mimicking the time varying tide gauge distribution would change these results but this could be investigated in the future.

Based on the comparison above, it seems that calculating basis functions through CSEOF decomposition, as opposed to EOF decomposition, allows for more

robust sea level reconstructions, especially in the case of less than ideal tide gauge datasets. This method was found to better reconstruct regional trend patterns, common oceanic indices, and GMSL variability with nearly all tide gauge distributions, noisy tide gauge data, and with different amounts of reconstructed variance.

CHAPTER 4 VARIABILITY IN THE NORTH EQUATORIAL CURRENT (NEC) BIFURCATION LOCATION

4.1 Overview

Up to this point, I have been explaining how reconstructions work and validating their quality. The remainder of the dissertation focuses on how sea level reconstructions can be used to further scientific knowledge. What began with a simple test to determine whether a known signal existed in two commonly used reconstructions eventually evolved into determining how a decadal signal contributes to global sea level. Looking at a single point (this chapter), evolved into looking at sea level trends in the nearby regions (Chapter 5), which led to determining how much the Pacific Decadal Oscillation contributes to global sea level (Chapter 6).

One of the key benefits of sea level reconstructions is that scientific phenomena found using satellite altimetry can be examined over a longer time period. Here, I do just that based on results found by *Qiu and Chen* [2010] (referred to as *QC2010* hereinafter). They use satellite altimetry sea surface height (SSH) data to determine the North Equatorial Current (NEC) bifurcation point in the tropical, western Pacific. They are then able to extend these results back in time

using sea level from a wind-driven 1½-layer reduced-gravity model. This work looks to serve a similar purpose using reconstructed sea level.

The westward flowing NEC is a result of the interaction between the North Pacific subtropical and tropical gyres. This current splits into a southward flow and northward flow upon reaching the Philippine Coast. This split, or bifurcation, separates the NEC into the Kuroshio, flowing north, and the Mindanao Current, flowing south [Nitani, 1972]. The bifurcation point affects properties of physical transport as well as biological systems in the region [e.g., Kimura *et al.*, 2001]. Qiu and Lukas [1996] show that the NEC bifurcation location is subject to local forcing through seasonal winds and remote forcing through baroclinic Rossby waves. Seasonally, the bifurcation point latitude typically reaches a northern (southern) limit in November/December (May-July), with a total latitude range of about 2°.

4.2 Data and Methods

4.2.1 Satellite Altimetry Datasets

Two satellite altimetry datasets were used for this analysis. The first is the AVISO gridded SSH anomaly dataset mentioned in Section 3.2.1. The second is the mean dynamic topography (mdt) mean sea surface height (SSH) field from Rio *et al.* [2011].

4.2.2 Sea Level Reconstructions

Two reconstructions are used for this analysis. Similar to Chapter 3, the two reconstructions used here differ primarily in the selection of basis function

decomposition methods. The first reconstruction of *Church and White et al.* [2004 (*CW2004*); 2006; 2011; referred to as the reconstruction of CW, hereafter] uses empirical orthogonal functions (EOFs) to decompose a custom satellite altimetry training dataset. The second sea level reconstruction considered here uses cyclostationary empirical orthogonal functions (CSEOFs) as basis functions to decompose the AVISO dataset [*Hamlington et al.*, 2011b (*H2011*); 2012; referred to as the reconstruction of HLK (*Hamlington, Leben, Kim*), hereafter]. Each reconstruction uses tide gauges from the PSMSL (Section 3.2.2) and tide gauge selection details can be found in *H2011* and *CW2004*.

4.2.3 Method of Calculating Bifurcation Latitude

QC2010 used satellite altimetry absolute SSH values to find meridional geostrophic velocity as a function of latitude along the Philippine coast. The bifurcation latitude is associated with a velocity of 0, allowing it to be tracked over time using absolute SSH values. To generalize the calculation, *QC2010* found the region of SSH anomaly most highly correlated with the bifurcation latitude and used least squares fitting to create a proxy relating sea level anomaly and bifurcation latitude. This relationship, $Y_p(t) = 11.9 - 0.13 \times h'(t)$, relates the bifurcation latitude (Y_p) to sea level anomaly (h' (°N)) averaged within a specific boundary at any given time (t). This boundary is from 12-14°N and 127-130°E, as depicted by the black box in Figure 17. The backdrop for Figure 17 is the mean dynamic topography, which makes apparent the large height gradients associated

with the NEC, Kuroshi, and Mindanao, allowing for their detection via satellite remote sensing.

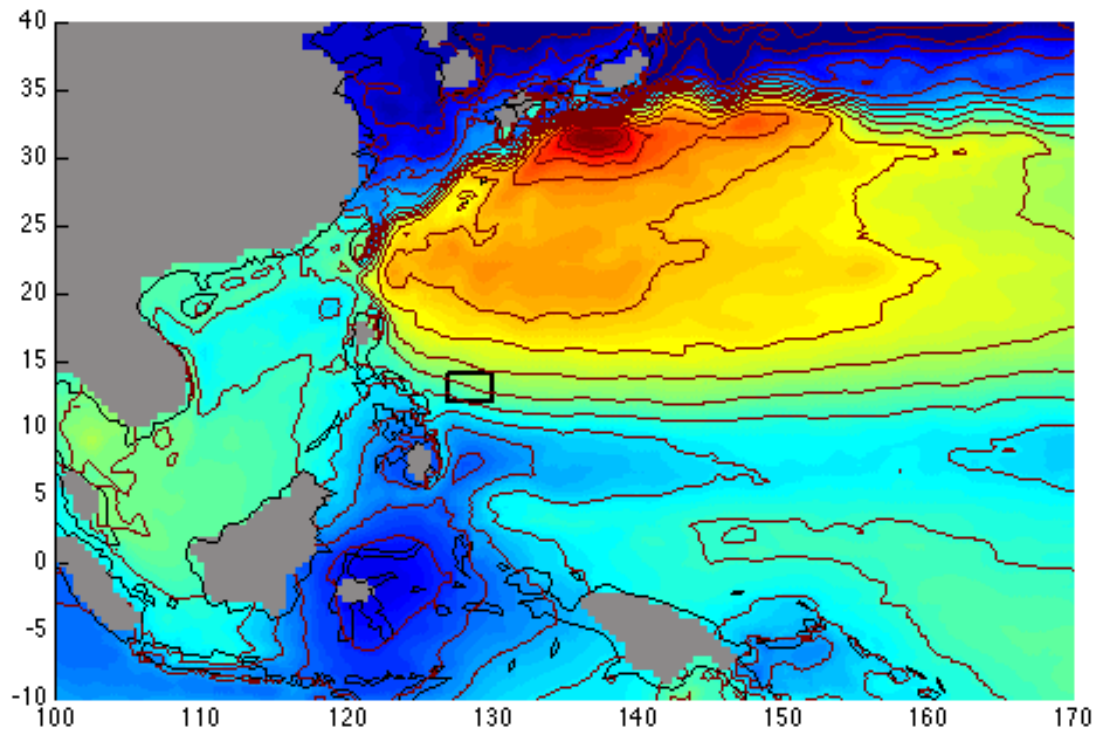


Figure 17. Mean sea surface height from *Rio et al.* [2011], ranging from 65 cm (blue) to 180 cm (red) with contours of 10 cm. The proxy box is shown in black.

4.3 Results

4.3.1 Reconstruction Verification

The initial step in any analysis using reconstructions is to verify that the reconstructions contain the signal being investigated. In this case, it is known that bifurcation latitude is a function of remotely originating Rossby waves; Figure 18 shows Hovmoller diagrams from the region in question to illustrate whether Rossby

waves are present in the datasets, shown as propagations from east to west as time increases. To verify these are actually Rossby waves, specific instances were selected and found to agree with Rossby wave theory, as in *QC2010*. A quick glance at Figure 18 allows for two conclusions to be made: 1) the Rossby waves found in the satellite altimetry dataset are well reconstructed in HLK; 2) Rossby waves are not present in the CW reconstruction. For this reason, CW is unable to accurately model the NEC bifurcation latitude and will not be used in further analysis.

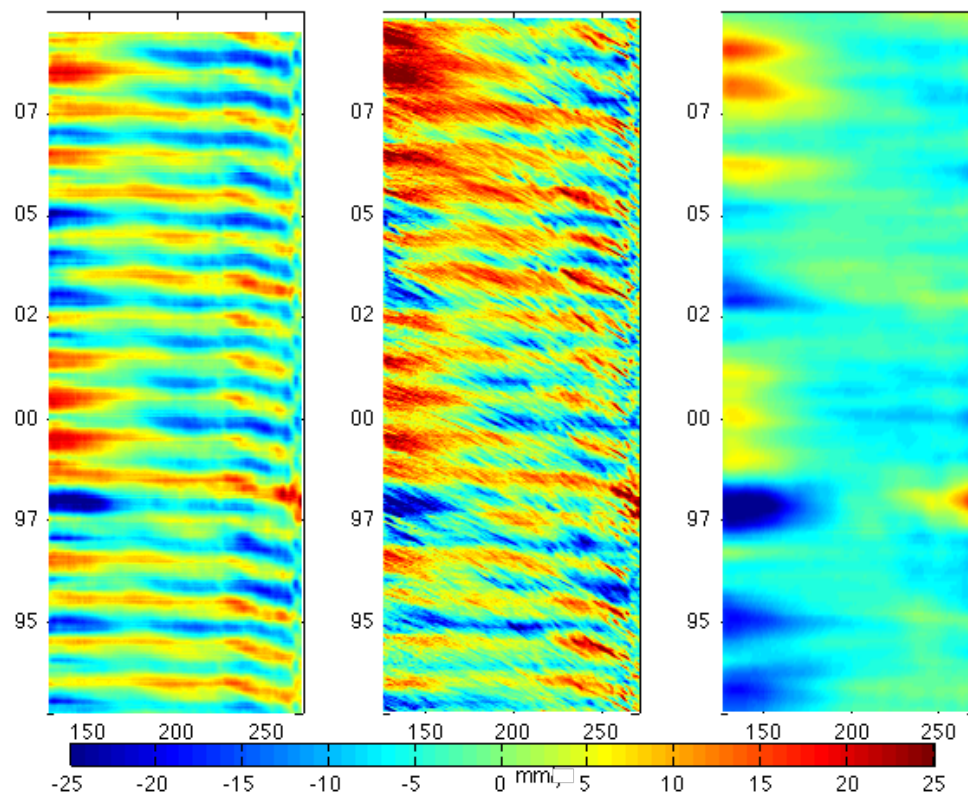


Figure 18. Hovmoller diagrams of SSH from HLK (left), AVISO (middle), and CW (right). Average of 12-14 °N latitude band, from 130 to 270 °E, over the time period 1993 to 2009.

Figure 18 shows some slight differences between HLK and AVISO. Mostly, these are related to spatial smoothing of the signals in HLK. To further verify that

the reconstruction will accurately portray bifurcation latitude, the aforementioned proxy was used with both the AVISO and HLK datasets. Figure 19 shows low-pass filtered time series of the bifurcation latitude computed from each dataset. It is apparent that both time series agree rather well, especially prior to around 2006. The disagreement following 2006 is most likely due to underestimated regional trend in the western Pacific by HLK, stemming from lack of sufficient tide gauge representation in that region. In agreement with *QC2010*, Figure 19 shows large migration on interannual and longer time scales of up to 4° , as opposed to seasonal variations typically on the order of $\sim 1^\circ$ (not shown).

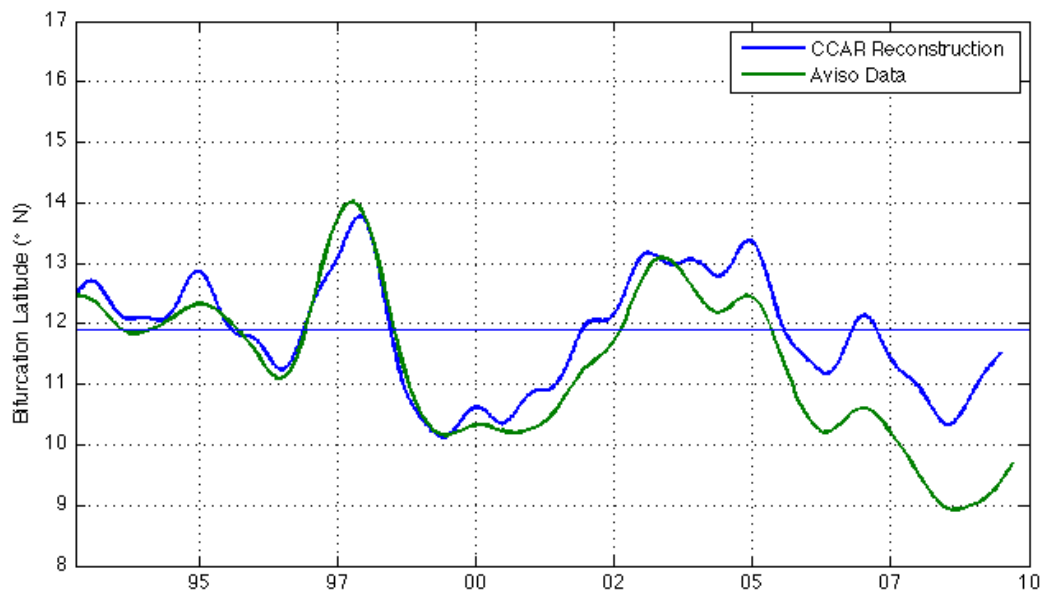


Figure 19. Bifurcation latitude time series from AVISO satellite altimetry data (green) and HLK reconstruction (blue). Time series are low pass filtered with a Gaussian filter and annual corner frequency.

4.3.2 NEC Bifurcation Latitude Back in Time

With the confirmation that the necessary signals are in the HLK reconstruction, the bifurcation latitude can be calculated over the entire reconstruction period with confidence. Figure 20 shows the smoothed NEC bifurcation latitude calculated from the HLK reconstruction and corresponding wavelet analysis. The quasi-decadal signals hinted at in Figure 19 span the entire analysis period. Additionally, a 3-5 year signal is apparent from 1980 through the late 90's. *QC2010* relate these interdecadal variations to surface wind forcing.

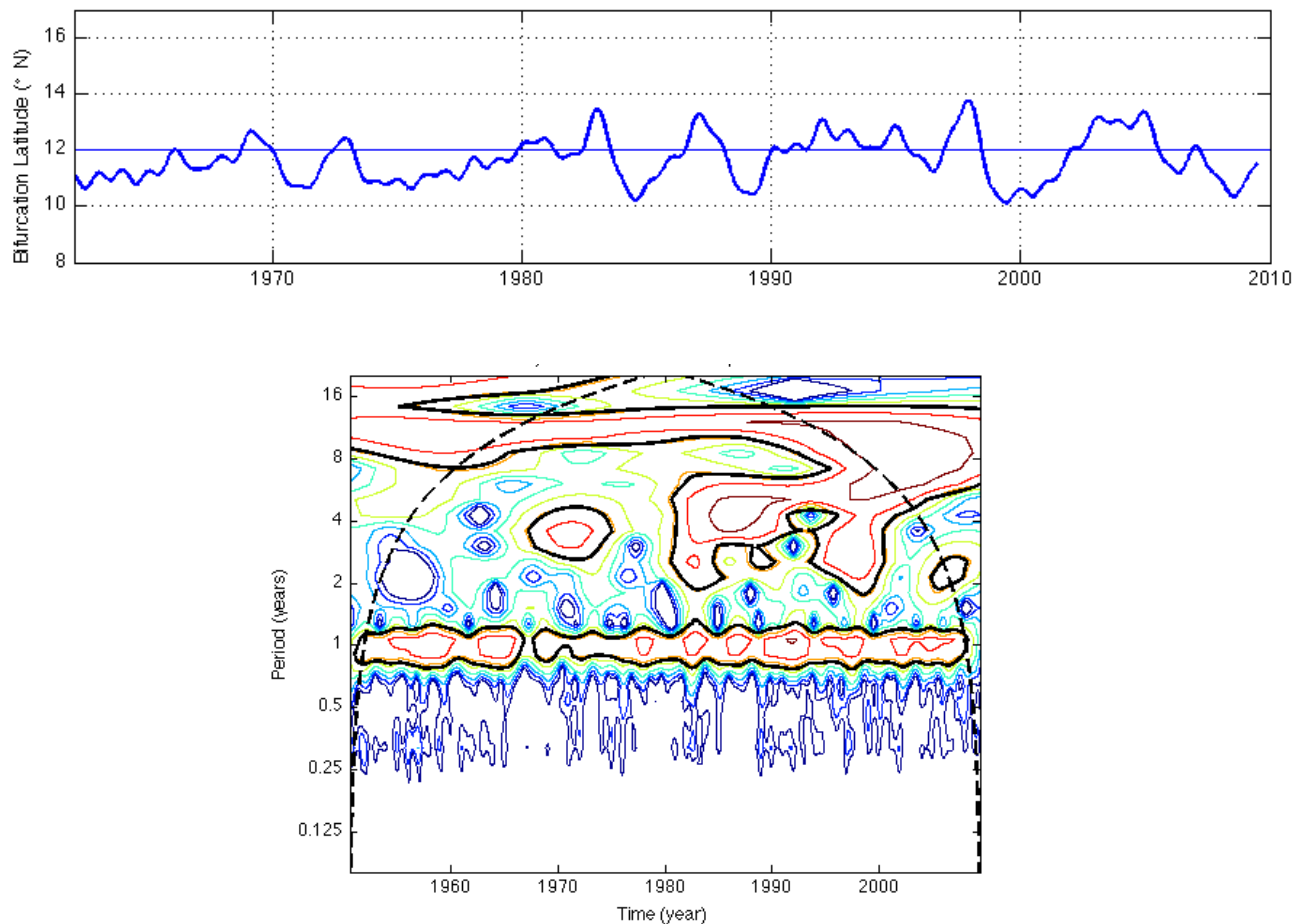


Figure 20. Top: NEC bifurcation latitude calculated from HLK and filtered as in Figure 19. Bottom: Wavelet power spectrum for reconstruction inferred bifurcation latitude; contour unit ($^{\circ}$)²; >95% confidence interval indicated by bold line; dashed line indicates cone of influence for edge effects.

When comparing the bifurcation latitude time series, the results from the 1 ½-layer reduced-gravity model used by *QC2010* and from HLK agree very well from 1980 onwards. Prior to this point, the phase is in agreement, however there exist discrepancies in the amplitude. When considering wavelet analysis, both data sources show strong annual and biennial variability, low longer time-scale variance prior to 1970 and significant quasi-decadal power in recent years. The one significant difference is that the bifurcation latitude inferred by the model used by *QC2010* does not show significant quasi-decadal signals prior to ~1990, while that inferred by HLK shows this signal over the entire time period.

4.3.3 Modal Analysis

QC2010 compare the NEC bifurcation latitude with the Nino3.4 index and find that although visually there is good correspondence between the two, correlation is only 0.5 and Nino3.4 is only able to explain 25% of the variance in the model derived bifurcation latitude. This is where one of the most interesting aspects of reconstructing with basis functions comes in. Due to the way reconstructions are created, by combining modes accounting for different amounts of variance (and sometimes specific physical signals), it is possible to examine how much certain modes contribute to signals within the reconstruction. Figure 21 shows the amount of variance in the latitude NEC bifurcation proxy latitude band (12-14°N) explained by each mode. It can be seen that the first couple modes

explain most of the variance and a total of over 95% of the variance in the region is accounted for with all 19 modes. Specifically, in the proxy box (Figure 17), modes 1, 2, and 9 account for 19, 34, and 7% of the variance, respectively. Based on experience with the HLK reconstruction and confirmed using wavelet analysis similar to that in Figure 20 (not shown), it is known that mode 1 represents the annual cycle and mode 2 represents the eastern Pacific ENSO. Mode 9 has both quasi-biennial and quasi-decadal power and is most likely a combination of different physical factors. Surprisingly, mode 3 represents the central Pacific components of ENSO, nearer to where the bifurcation actually takes place, and is not responsible for much variance in the proxy location.

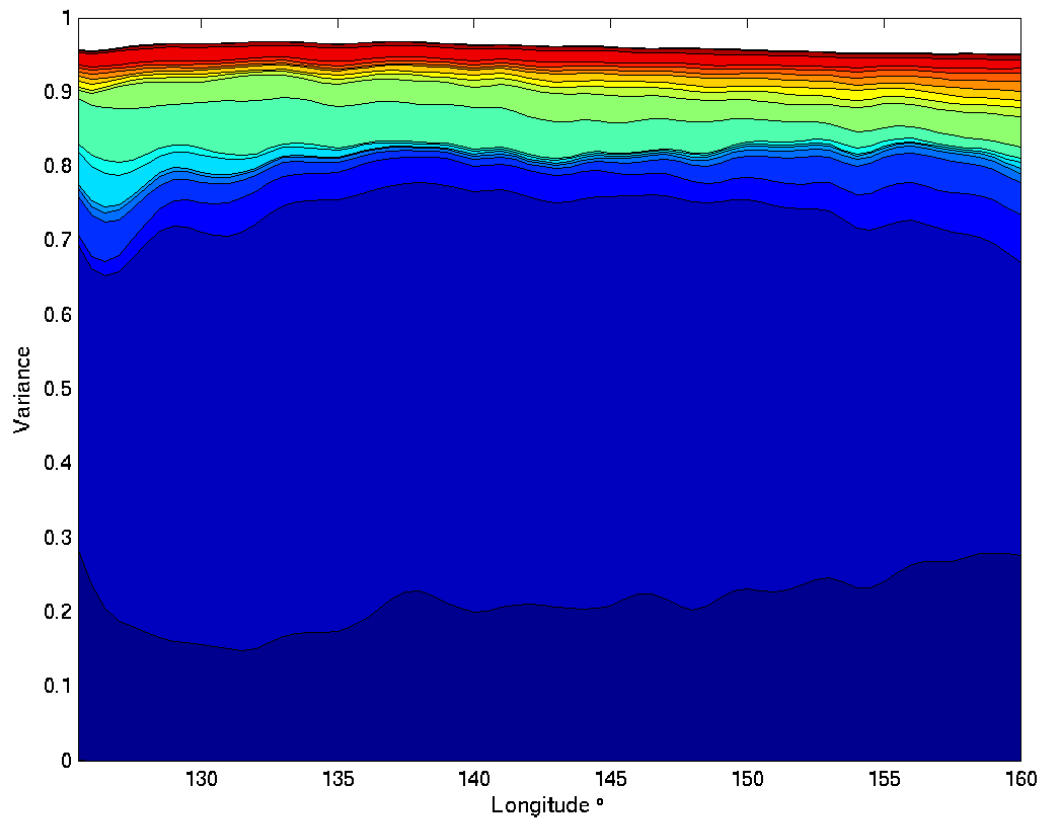


Figure 21. Modal variance averaged in the 12-14°N latitude band. Mode 19 starts on the top (red) and they decrease in descending order to mode 1 on the bottom (dark blue).

Once the most dominant modes are determined, it is possible to reconstruct with just those modes, creating an optimized 'filter'. Sea level was reconstructed in the region of interest using only modes 2, 3, 9, and 17, and the NEC bifurcation latitude was calculated from the result (Figure 22). This agrees very well with the low-pass filtered result found previously. It should be noted that the omitted modes do contribute to the local sea level and their absence causes the discrepancy in amplitudes seen in Figure 22. This technique could prove quite useful in certain circumstances, e.g. one might want to look for monthly signals that are not associated with the annual cycle. Low pass filtering would get rid of the desired signal, however simply removing the annual mode would allow for the desired (monthly) signal to remain.

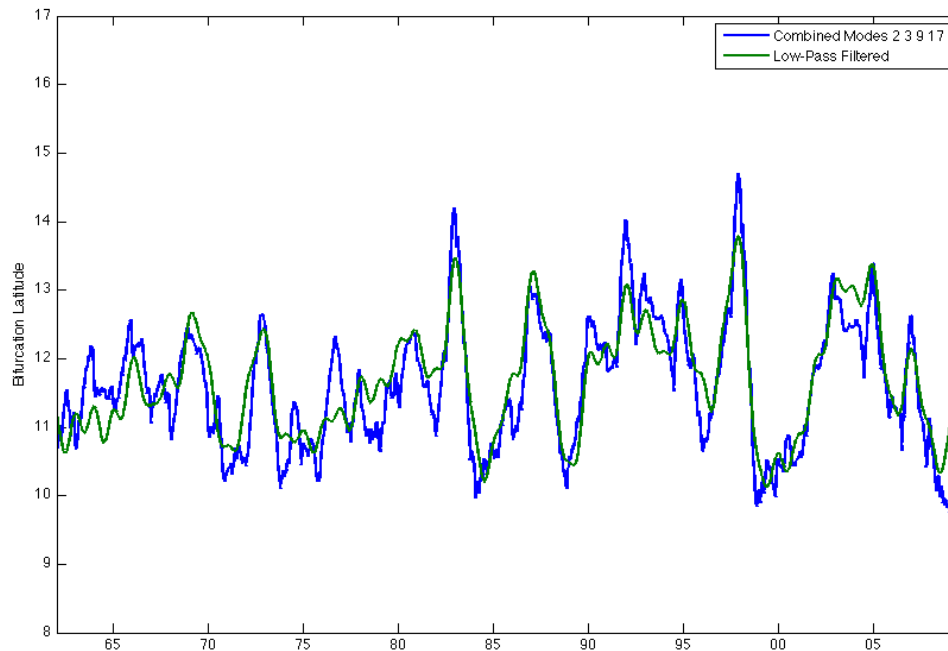


Figure 22. Non-filtered NEC bifurcation latitude inferred from sea level reconstruction using only modes 2, 3, 9, 17 (blue) and filtered NEC bifurcation latitude inferred from full HLK (green).

4.4 Conclusions and Discussion

This work found that CSEOF based reconstructions, such as HLK, are capable of capturing signals such as propagating Rossby waves. On the other hand, it was found that the CW EOF reconstruction does not capture this signal. Additionally, it was shown that the HLK reconstruction is a viable replacement for a sea level model when investigating the NEC bifurcation latitude back in time, using the methods presented by *QC2010*. This further confirms that the bifurcation location is dominated by 3-5 year variance back to the 70's and also presents the idea that quasi-decadal variance is more extensive than found by *QC2010*. The introduction of modal analysis allowed for a method of determining which physical

signals are responsible for variance associated with the NEC bifurcation. Further, reconstructing sea level with only the most dominant modes created a type of optimized filter.

Although most of the results presented agree with those of *QC2010*, two main discrepancies between the bifurcation latitude from HLK and the 1-½ layer model exist: 1) The longer period (quasi-decadal) variability prior to 1990 is only present when using HLK; 2) Disagreement in bifurcation latitude between both data sources prior to 1980. At this point, the causes behind these discrepancies are unknown, but certainly neither the reconstruction nor the model is perfect, so each surely has a hand in the disagreement. *QC2010* report the Nino3.4 index explains 25% of the model bifurcation latitude variance. The Nino3.4 is a more central Pacific region, which may speak to ones intuition when considering the NEC bifurcation, however, the modal analysis shown here suggests that the central Pacific ENSO does not play a large role in the bifurcation latitude. Perhaps a coupled index that takes into account more than one variable such as the Multivariate ENSO Index (MEI) would better correlate to the NEC bifurcation latitude. The MEI region is -30 to 30°N and 100 to 290°E; using this region would also take into account signal leaking through Indonesia into the Indian ocean, which brings up another very interesting sea level reconstruction case and a good segue to Chapter 5.

CHAPTER 5 SEA LEVEL TRENDS IN SOUTH EAST ASIAN SEAS (SEAS)

5.1 Overview

Sea level is a measurement of considerable interest and importance for the study of climate because it reflects both mass and heat storage changes in the global ocean. Variations in sea level over long time periods provide an important “lens” into the current state of the climate. Over the last century, sea level has been rising at an increasing rate due to the thermal expansion of water associated with the warming ocean and the melting of land ice [e.g. *Church et al.*, 2011]. While the trend in global mean sea level (GMSL) is positive (estimated from satellite altimetry to be 3.2 mm/yr.), the rise of sea level is far from uniform across the globe. Regional sea level changes in most areas of the ocean are strongly affected by spatially varying factors such as ocean warming, ocean dynamic responses, and gravitational and solid earth effects from changing surface mass [e.g. *Slangen et al.*, 2012; *Perrette et al.*, 2013].

Attributing the trends in both regional and global sea level to specific processes has important implications for projecting sea level rise in the future. Removing trends, for instance, associated with known climate variability can allow for a better understanding of the underlying warming trend [*Hamlington et al.*, 2011a; 2013; *Chambers et al.*, 2012]. In some regions, climate variability on decadal

(or longer) timescales can lead to trends that are significantly larger than the background secular trend. Identifying and explaining signals contributing to regional and global sea level variability and trends has been a frequently studied problem in recent years [e.g. *Bromirski et al.*, 2011; *Chambers et al.*, 2012; *Feng et al.*, 2004; *Hamlington et al.*, 2011a; *Merrifield et al.*, 2012; *Fasullo et al.*, 2013; *Han et al.*, 2013; *Hamlington et al.*, 2013]. The exceptional temporal length and global coverage of sea level reconstructions allows for an examination of longer timescale climate signals and the chance to assess their contribution to sea level trends both regionally and globally. Furthermore, it is possible to determine whether the current rate and spatial pattern of sea level change are uncommon or instead are simply a recurrence of multi-decadal climate oscillations [e.g. *Meysignac et al.*, 2012b].

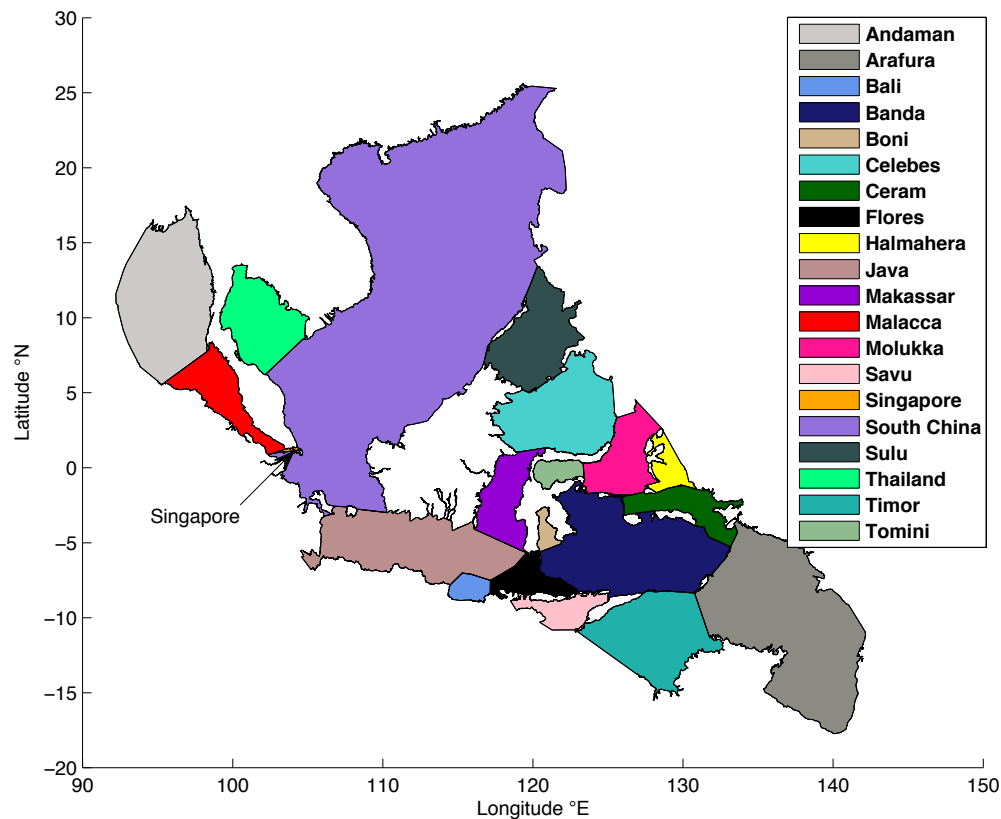


Figure 23. The 20 bodies of water (seas, straits, and gulfs) defined in the Limits of the Ocean and Seas [IHO, 1953] from the SEAS region.

This chapter focuses on an area of the ocean particularly affected by rising sea level in the past two decades. The Southeast Asian Seas (SEAS) region spans the largest archipelago in the global ocean and is comprised of a total of 20 seas according to the *Limits of the Ocean and Seas* published by the International Hydrographic Organization (IHO) in 1953 (IHO, 1953). Figure 23 shows the regional seas, straits, and gulfs as defined by the IHO and delineated by a high-resolution coastline data set [Fourcy and Lorvelec, 2013]. The region has many low-lying and densely populated coastal areas including large urban and rural river

deltas and thousands of small-inhabited islands. The Indonesian archipelago alone consists of 17,508 islands (6,000 inhabited) and encompasses the only tropical interoceanic throughflow in the global ocean, providing a complex oceanic pathway connecting the Pacific and Indian Oceans. The Indonesian throughflow, and thus sea level, is driven primarily by free equatorial Kelvin and Rossby (Figure 24) waves originating along the Indian and Pacific equatorial waveguides [Wijffels and Meyers, 2004] such as those discussed in Section 4.1, which were partly responsible for forcing the NEC bifurcation latitude variability. The SEAS region is also one of the most biodiverse oceanographic regions on the planet. Southeast Asia's coral reefs have the highest degree of biodiversity of all of the world's coral reefs and it is estimated that only 10 percent of the marine species associated with coral reefs have been identified and described (*Reaka-Kudia, 1997*).

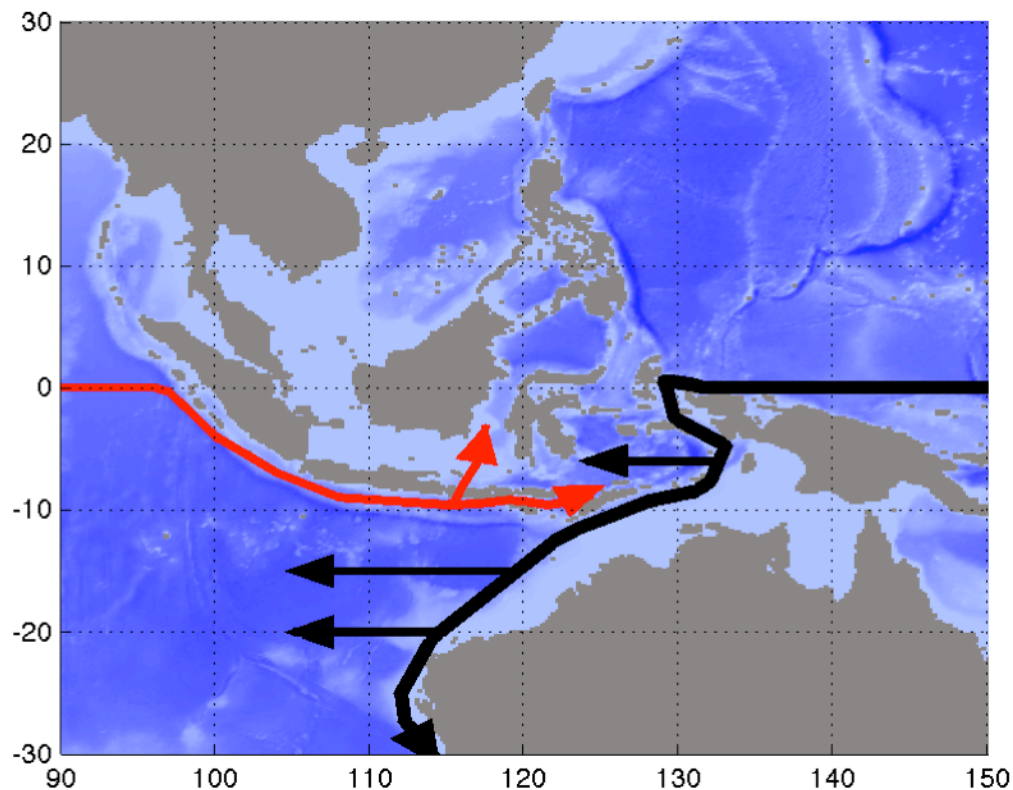


Figure 24. Schematic of remotely forced wave pathways into the Indonesian throughflow region (after *Wijffels and Meyers [2004]*). Red lines show the waveguide from the equatorial Indian Ocean, with energy spreading into the internal seas through both Lombok and Ombai Straits (red arrows). Black lines show the pathways for equatorial Pacific wind energy traveling down the Papuan/Australian shelf break and radiating westward-propagating Rossby Waves into the Banda Sea and South Indian Ocean (black arrows).

In the past two decades the SEAS region has experienced rising sea levels at rates more than double the global mean. Given the low-lying and densely populated coastal areas, there is great concern regarding whether the trends observed in the past two decades will persist into the coming decades. In this study, I examine the sea level trends in the SEAS region over the past sixty years, and extend recent studies on sea level in the Pacific Ocean [e.g. *Meyssignac et al., 2012; Merrifield et*

al., 2012; *Han et al.*, 2013; *Hamlington et al.*, 2013] to assess the direction of sea level variability in the near future. Our goal is to understand if the trends observed in the SEAS region by satellite altimeters are exceptional or have similarly occurred in the past, and if the trend pattern in the region is driven by decadal variability, what should be expected with regards to sea level rise in the future. To do this, I will use two different sea level reconstructions coupled with the satellite altimetry data. Using the definition of the SEAS provided by the IHO, the trend in each individual body of water is estimated and effect of decadal climate variability on trends in the SEAS region discussed. This study has important implications for the coastal populations in the SEAS region, providing the opportunity to gain a better understanding of future sea levels in perhaps the area on Earth most gravely affected by recent sea level rise.

5.2 Data and Methods

5.2.1 Satellite Altimetry and Tide Gauge Datasets

The satellite altimetry dataset used in this chapter is the AVISO data previously mentioned in Sections 3.2.1. These data are used as a baseline for comparison as well as in four of the five sea level reconstructions used in the study.

Each reconstruction uses tide gauge data from the Permanent Service for Mean SEA Level (PSMSL), also previously mentioned in Section 3.2.2. Each reconstruction uses different tide gauge editing and selection criteria depending on

time-series length, data gaps, area weighting, etc. These details will not be discussed but can be found in the respective reference for each reconstruction.

5.2.2 Sea Level Reconstructions

Five different sea level reconstructions are used in this analysis. They vary based on the training data and reconstruction method used. A summary of basic information concerning each reconstruction is given in Table 4. Please refer to the corresponding references if more information is desired. Note: HLK/TG was referred to as HLK in Chapter 4, and CW was previously mentioned as well.

Table 4. Summary of sea level reconstruction properties.

Reference	Abbr.	Basis Function Method	Training Data	Observation Data	Training Data Time Period	# of Modes	Percent of Variance	Reconstructed Time Period
Church et al. [2004]; Church and White [2006]	<i>CW</i>	EOFs	Custom 1° by 1° monthly SSHA maps derived from TOPEX/Poseidon, Jason-1 and OSTM (Jason-2) 10-day repeat altimetry using a 300 km Gaussian filter	Monthly sea level observations from 426 PSMSL tide gauge stations	1993 through 2009	20	84% of the non-annual signal	1950 through 2009
Hamlington Leben, and Kim [2012]	<i>HLK/TG</i>	CSEOFs	AVISO weekly SSHA subsampled to ½° by ½°	Monthly sea level from 377 PSMSL tide gauge stations upsampled to weekly observations	1993 through 2009	11	80% of the non-annual signal	1900 through 2009
Hamlington Leben, and Kim [2012]	<i>HLK/BV</i>	CSEOFs	AVISO weekly SSHA subsampled to ½° by ½° NOAA OISST weekly 1° by 1° SST	*Monthly sea level from 377 PSMSL tide gauge stations *Monthly SST ICOADS 2° by 2° observations	1993 through 2009	11	80% of the non-annual signal	1900 through 2009
Meyssignac et al. [2012]	<i>M/Alt</i>	EOFs	Annual Averaged AVISO	Annual averaged sea level observations from 91 PSMSL tide gauge stations	1993 through 2009	15	~ 88%	1950 through 2009
Meyssignac et al. [2012]	<i>M/Mean</i>	EOFs	Annual Averaged AVISO SODA 2.0 Drakkar/NEMO model	Annual averaged sea level observations from 91 PSMSL tide gauge stations	1958 through 2007	15	??	1950 through 2009

5.2.2.1 *Hamlington et al.* [2012] Bivariate Reconstruction (HLK/BV)

In addition to AVISO and PSMSL data, HLK/BV uses sea surface temperature (SST) to create a bivariate reconstruction. The SST training data are Optimal Interpolation SST (OISST; <http://www.esrl.noaa.gov/psd/data/>) data from NOAA, which are a combination of in situ SST data and satellite measurements, as well as simulated SST values near sea ice. The historical in situ SST data come from the International Comprehensive Ocean-Atmosphere Data Set (ICOADS; <http://icoads.noaa.gov/>), averaged to a $2^\circ \times 2^\circ$ grid and known as superobservations [*Smith et al.*, 1996].

To utilize SST measurements for an SSH reconstruction, basis functions of the SST training data are computed using CSEOFs. These basis functions are then transformed to have the same principal component time series as the SSH basis functions. The transformed SST basis functions and the SSH basis functions are then interpolated with the respective in-situ measurements to form a bivariate reconstruction [*Hamlington et al.*, 2012].

5.2.2.2 *Meyssignac et al.* [2012] Mean Reconstruction (M/Mean)

Meyssignac et al. [2012] created a mean sea level reconstruction dataset by averaging a satellite altimetry reconstruction with two model data reconstructions made using the SODA 2.0 [*Carton and Giese*, 2008] and the Drakkar/NEMO [*Dussin et al.*, 2009] ocean models.

5.2.3 *Estimating Sea Level Trends*

Prior to comparison, each reconstruction was annually averaged for consistency. Linear trends were computed over a variety of time spans and the uncertainty of each trend was found using standard error estimates for the trend term determined from the least squares linear regression.

5.2.4 *SEAS Regional Definition and Analysis*

For the SEAS regional analysis, the region was subdivided into 20 separate bodies of water, as shown in Figure 23. For each dataset, all points within a given boundary were averaged to determine an areal averaged mean time series for each body of water. If no points were present in the dataset, the nearest point was used. Linear trends were found after the calculation of subregion averages.

5.3 Results

While the sea level trends in the SEAS region have been large in the past two decades, a more pressing topic is whether the regional sea level trends will be similarly high in the coming decades. Projecting future regional sea level rise is a challenging task that requires expertise across a wide range of disciplines, and a broad understanding of the Earth system. One way to gain an understanding of possible future directions and ranges of sea level is to study changes on similar timescales in the past. As discussed above, sea level reconstructions extend the satellite altimetry record of sea level back in time, providing the opportunity to study the influence of low frequency variability on sea level trends. To highlight the trend variability at the time scales observed over the current altimetric record, 17-

year regional trend maps were computed with a least-square estimate of the linear trend from the sea level reconstruction dataset. Figure 25 shows these trend maps over the altimeter record time period, 1993-2009.

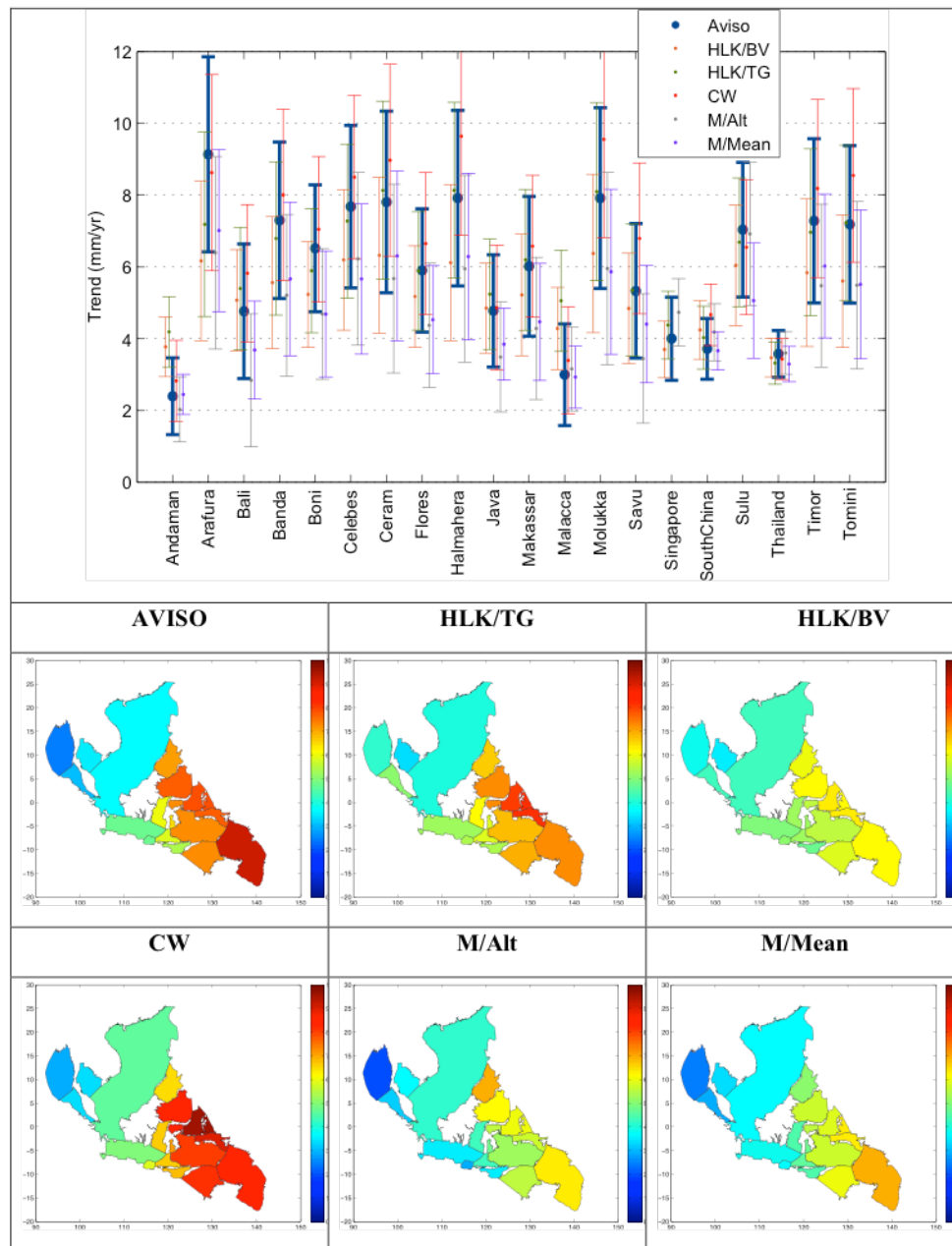


Figure 25. SEAS average sea level trends over the 17-year satellite altimeter record from 1993-2009 shown plotted as trend values with standard error estimates (A) and as color maps for AVISO and each of the reconstructions. Reconstructed average trends agree with AVISO (shown in bold) to within the estimated error.

In *Meysiganac et al.* [2012b], the question was asked whether the pattern of sea level trends observed during the satellite altimeter era had similarly occurred in the past 60 years. This is further explored by correlating the AVISO trend map with 17-year trend maps from the sea level reconstructions extending back to 1950 (Figure 26). Correlation extrema are centered in 1967, 1984 and 2001, implying a trend pattern like that observed by satellite altimetry has been present in the past, or in the case of 1984, the opposite trend pattern. Examining the regional trends in this region further allows for better understanding of the decadal variability that affects the sea level in this vulnerable region.

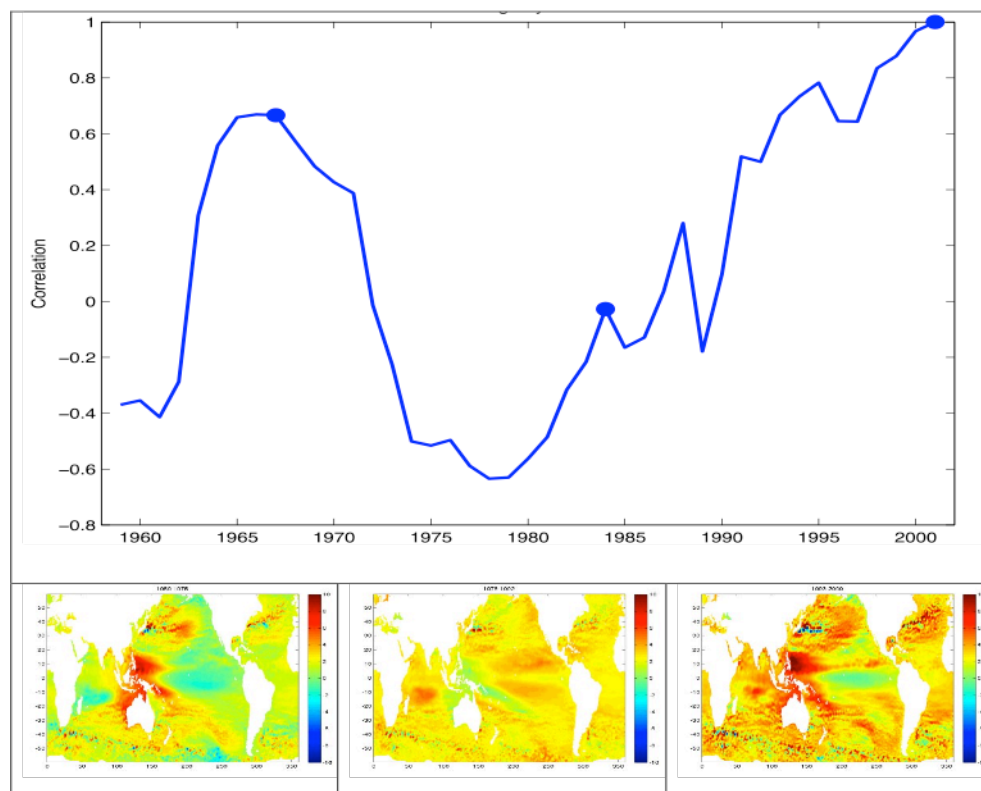


Figure 26. Lagged correlation coefficient (shown as the blue line in the upper plot) of the historical 17-year regional trend maps with the linear trend map from the satellite altimeter time period 1993-2009 centered on 2001 (rightmost blue dot). The bottom plot shows the 17-year sea level trend maps from HLK/BV in mm/year for the 1959-1976 (left), 1977-1992 (center), and 1993-2009 (right) time periods. The blue dots shown on the upper plot are the center points of the three 17-year windows.

Sea level trends in the SEAS region are some of the largest observed in the modern satellite altimeter record covering the past two decades. Regional sea level trends over the 17-year satellite altimeter record 1993 through 2009 are shown in Figure 25 for the AVISO data set and each of the sea level reconstructions during the training data set time period. Reconstructed sea level average trends in the SEAS agree with the AVISO values to within the estimated error, with the five reconstructions also showing good agreement over the entire region. Trends in the region over this time period are strictly positive and approach values greater than 1 cm/year in some areas. Trend values in the southeastern part of the SEAS region have been particularly high in the past two decades. To determine how the recent sea level trends compare to the past, sea level trends from 1959 to 1975 are computed (Figure 27). As in the past two decades, the sea level trend in each of the seas in the region is positive, with the highest trends found in the southeastern part of the SEAS region. In general, the HLK/BV, HLK/TG and CW reconstructions agree although some discrepancy is seen in the northwestern region of the SEAS, possibly a result of differing tide gauge selection and reconstruction technique between the three reconstructions. The M/Alt and M/Mean reconstructions show significantly lower trends during this period, possibly a function of over-fitting or tide gauge selection, causing underestimation of the regional trend.

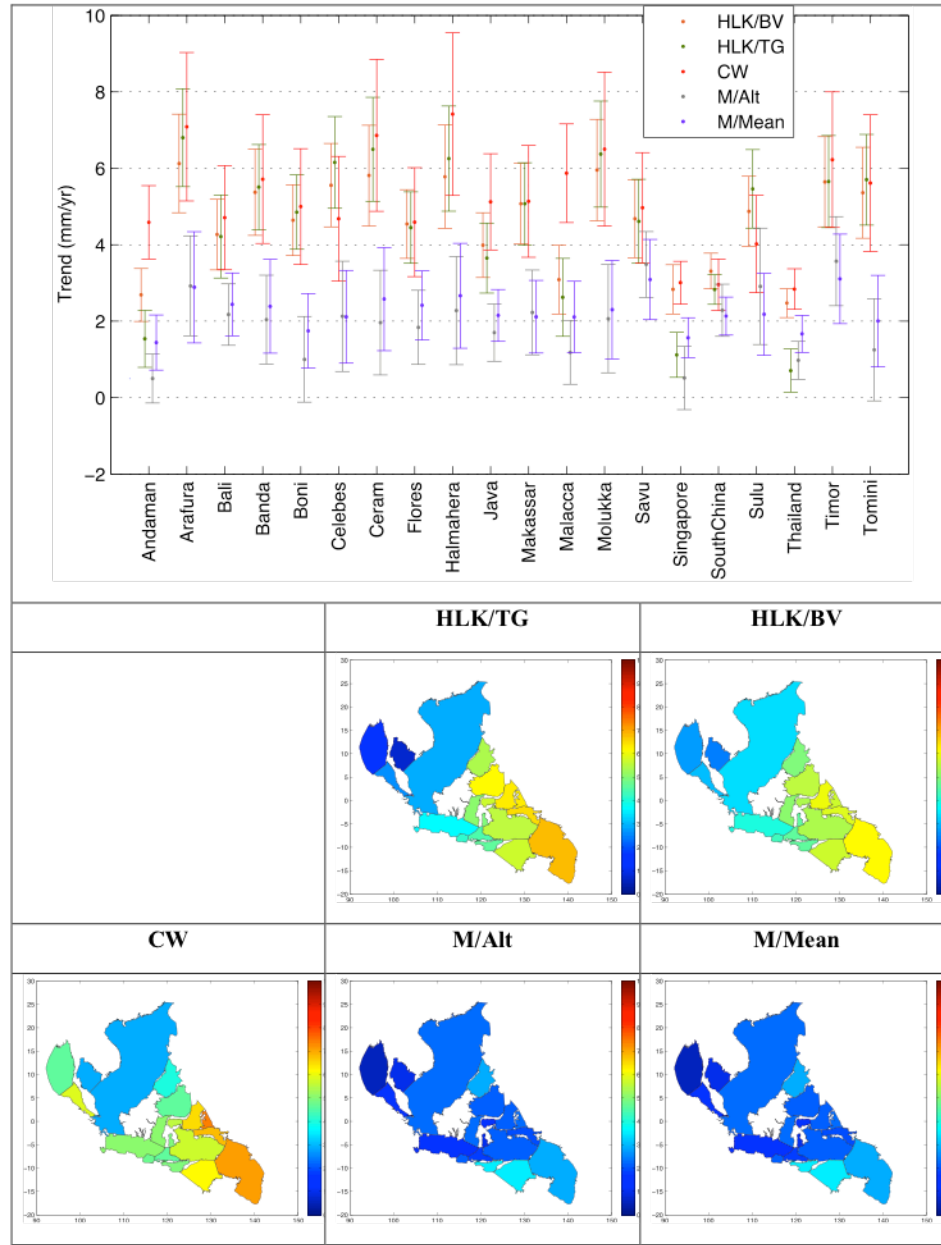


Figure 27. SEAS average sea level trends over the 17-year time period from 1959 through 1975 shown plotted as trend values with standard error (upper plot) and as color maps (bottom panels) for each reconstruction.

Finally, the sea level trend pattern in the SEAS from 1976 to 1992 is computed from all reconstructions (Figure 28). In contrast to the other two time periods, the sea level trends are much lower throughout the region, with the range

of sea level trends in some areas becoming negative. During this period, all reconstructions are in consensus to within the estimated error.

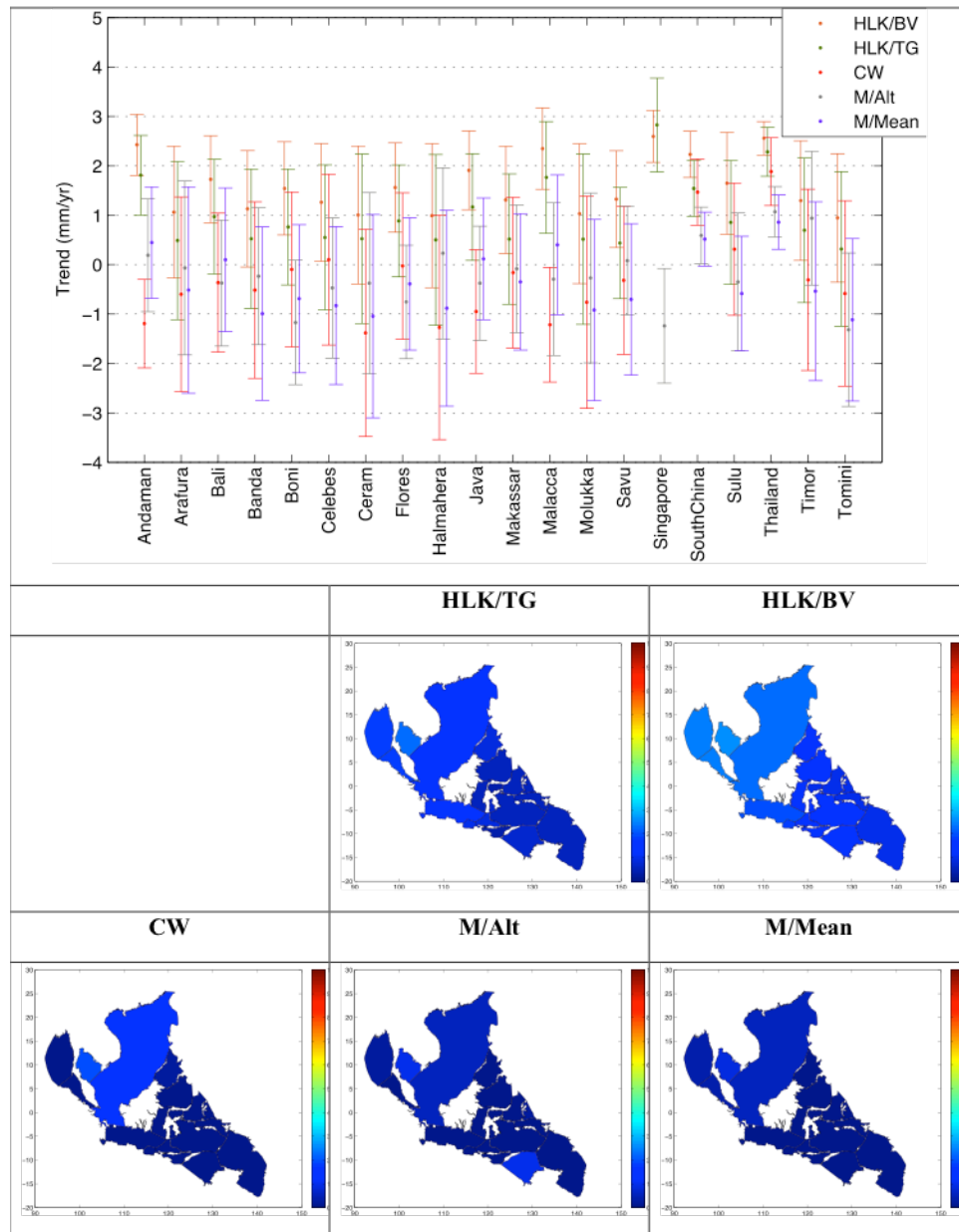


Figure 28. SEAS average sea level trends over the 17-year time period from 1976 through 1992 shown plotted as trend values with standard error (upper plot) and as color maps (bottom panels).

By comparing the 17-year sea level trend patterns from the past 50 years, the decadal-scale variability of sea level change in the SEAS region becomes evident. In Figure 29, using only the HLK/TG reconstruction, the trends for each sea over the three independent time periods are presented to highlight this variability. The similarity between trends for the time periods centered on 1967 and 2001 is clear, as are the significantly lower trends estimated for the 17-year window centered on 1984.

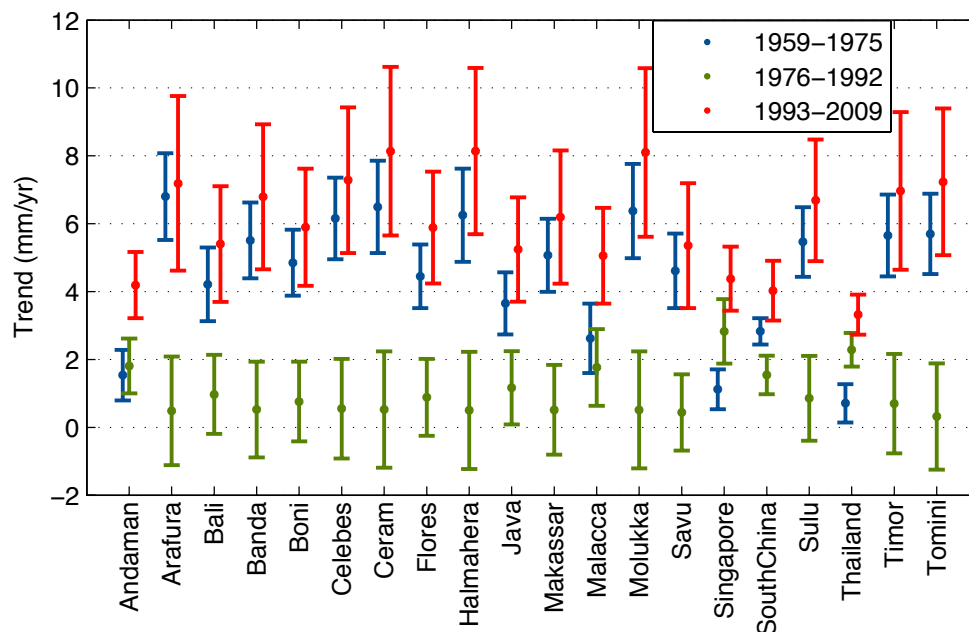


Figure 29. SEAS average sea level trends from the HLK/TG reconstruction for the three 17-year time periods centered on 1967, 1984, and 2001.

The question remains, what is driving these changes in the SEAS sea level trends and, more generally, the western Pacific sea level trends? *Merrifield et al.* [2012] showed that, when detrended by GMSL, the western Pacific sea level is correlated with the low-frequency variability of the Pacific Decadal Oscillation

(PDO) and the Southern Oscillation Index (SOI). This sea level signal is driven by anomalous decadal wind variability over the equatorial Pacific and propagates along the Rossby waveguide through the SEAS archipelago reaching as far south as Fremantle on the western Australian coast. Similarly, the next chapter discusses the influence of the PDO on both global and regional sea level trends, demonstrating that changes in the PDO have a significant impact on sea level trends in the tropical Pacific. Computing 17-year trends of the PDO index [*Mantua et al*, 1997], extrema are found centered roughly on the years of 1965, 1980, and 1997, corresponding closely to the centers of the three windows considered here. In light of the aforementioned previous studies and the analysis shown here, it is clear that there is a strong relationship between sea level trends in the SEAS region and decadal scale climate variability.

5.4 Conclusions and Discussion

This study focuses on a region of the globe that has been significantly impacted by rising sea levels in the past two decades. Whether sea level trends will be similarly high in the coming decades is an important question with significant societal and economic implications for the SEAS region. While projecting future sea level is an expansive problem, an understanding of future sea level can be gained by looking at the past. Sea level reconstructions provide a useful tool for understanding sea level changes in the past, present and future by extending the short satellite altimetry record back in time with the help of tide gauges.

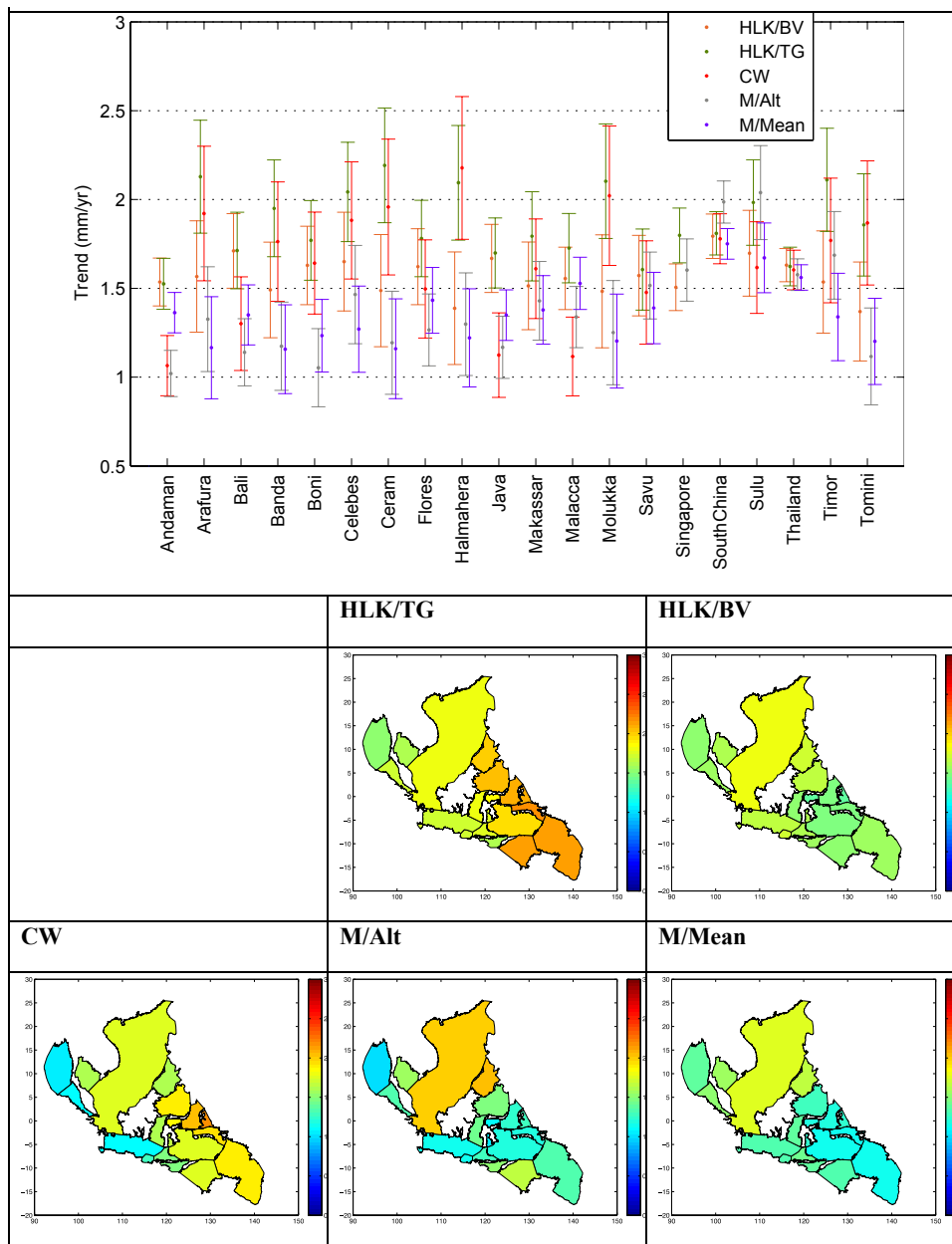


Figure 30. SEAS average sea level trends over the 60-year time period from 1950 through 2009 shown as plotted as trend values with standard error (upper plot) and as color maps (bottom panels) for each of the reconstructions.

Here, five sea level reconstructions created using multiple techniques have been used to study the sea level trends in the SEAS. The reconstructions agree well for the three 17-year windows considered (centered on 1967, 1984 and 2001), with

the exception of M/Alt and M/mean. Based on global trend maps (not shown) it is hypothesized that the disagreement here is caused by over-fitting and tide gauge selection of the M/Alt and M/mean reconstructions. Trend results exhibit decadal-scale fluctuations in the sea level trends in the SEAS region over the past 60 years. In light of this study and other recent studies [e.g. *Merrifield et al.*, 2012; *Hamlington et al.*, 2013], it is likely that the recent strong sea level trends observed during the altimetry record will abate as trade winds fluctuate on decadal and multi-decadal timescales. This suggests that SEAS regional sea level trends during the 2010s and 2020s are likely to be less than the trend in GMSL, similar to the smaller sea level trends observed during the 1976 to 1992 time period relative to GMSL. While the trends can be expected to be lower in the coming decades the long-term sea level trends in the SEAS region will continue to be affected by GMSL rise occurring now and in the future. The sea level trends from both reconstructions over the full time period from 1950 to 2009 are positive for the entire SEAS region (Figure 30). This underlying trend will be expected to persist, increasing the impact of decadal-scale fluctuations of sea level trends. In other words, in the future when the large positive sea level trends in the SEAS observed during the satellite altimeter era return to the region, the impact can be expected to be much more severe due to the higher seas upon which the decadal variability is occurring. The next chapter expands on these results to investigate how PDO has affected sea level in the past.

CHAPTER 6

INVESTIGATING THE PACIFIC DECADAL OSCILLATION (PDO) CONTRIBUTION TO GLOBAL SEA LEVEL

6.1 Overview

As previously discussed, the modern satellite altimetry record, spans only twenty years, making it difficult to separate longer-term secular trends and accelerations from natural climate variability. Sea level variations on decadal – and longer – timescales are known to contribute to the sea level trends since 1993, but evaluating their impact is challenging using only the short satellite altimeter record. Similar to the material just presented, this chapter exploits the long time series made available by reconstructions as a solution to this problem.

Identifying and explaining signals contributing to regional and global sea level trends has been a frequently studied problem in recent years [e.g. *Bromirski et al.*, 2011; *Chambers et al.*, 2012; *Feng et al.*, 2004; *Hamlington et al.*, 2011; *Merrifield et al.*, 2012; *Hamlington et al.*, 2013]. Removing trends associated with known climate signals can allow for a better understanding of the underlying warming trend, serving to unmask the presence of acceleration in GMSL or anthropogenically forced sea level rise, for instance. Understanding the contribution of climate signals with known periods to sea level trends can aid in the prediction of future sea level rise, as mentioned in Chapter 5. Predictions of the El Nino

Southern Oscillation (ENSO), for example, provide insight not only into future weather and precipitation patterns for different areas across the globe, but also into changes in regional and global sea level.

This chapter builds on the previous work to assess the variability of the spatial pattern of sea level rise over the past sixty years and its relationship to GMSL. Through this study, it is found that the Pacific Decadal Oscillation (PDO) [Cummins, 2005; Mantua and Hare, 2002] has a significant impact on sea level trends not just regionally in the Pacific Ocean [Meysignac, 2012b; Bromirski, 2011; Merrifield, 2012; Zhang, 2012], but also globally. The PDO contribution to the trend in GMSL over the last twenty years can be quantified, and by removing this contribution, a better understanding of the underlying secular trend in sea level rise can be obtained. This has important implications for the estimates of the both the trend and acceleration in GMSL over the past sixty years. GMSL is one of the most important indicators of climate change, and gaining a better understanding of the trend in GMSL has important implications for future projections of sea level rise.

Several studies have looked at the relationship between the PDO and sea level in the Pacific using both observational and model analysis [e.g. Meysignac et al., 2012; Merrifield et al., 2012; Zhang and Church, 2012; Cummins et al., 2005; Hamlington et al., 2013; Han et al., 2013]. In particular, Meysignac et al. [2012] attributed the fast western tropical Pacific (WTP) sea level rise during the past couple decades to natural variability, since similar east-west dipole patterns in the tropical Pacific were found in simulations of climate models with and without

anthropogenic forcing. While the results of *Han et al.* [2013] corroborate the conclusion that Pacific decadal climate modes are associated with basin-wide sea level patterns, it was determined that the large sea level trends observed in the WTP cannot be entirely explained as natural variability. Additionally, a spatial pattern associated with this signal can be removed, allowing for identification of a regional pattern of sea level rise in the western Pacific. Regional deviations from the global mean sea level (GMSL) change often reach 50-100% along the world's coastlines, severely limiting the utility of global sea level metric for planning and adaptation purposes. Understanding the factors that cause regional variation in sea level rise has important implications for the ability to project sea level at the regional level in the future.

6.2 Data and Methods

6.2.1 Datasets

AVISO, the HLK (HLK/TG) reconstruction, and the CW reconstruction are considered again. Refer to previous descriptions or references for more information [*H2011*; *CW2004*].

6.2.2 Estimating Sea Level Trends

Twenty-year linear trend maps were created through least squares fitting from annually averaged datasets, as described in Section 5.2.3. The maps were computed starting in 1960 (using data from 1950 to 1970) and advancing one year at a time to create 40 total maps. EOFs of the twenty-year trend maps from the sea

level reconstructions were computed. The contribution of each individual EOF mode to the twenty-year trends in GMSL could then be assessed by averaging the spatial component of the EOF (loading vector) and combining that with the temporal component (principal component time series). Additionally, reconstructing sea level associated with just one EOF mode can give an estimation of regional sea level contribution from a physical signal corresponding to that mode.

6.3 Results

6.3.1 20 Year Trends in Sea Level

As an initial check of the fidelity of the two sea level reconstructions, the spatial distribution of the linear trend over the altimeter time period (1993 to present) is computed for the AVISO dataset and the two reconstructions, HLK and CW. As seen in Figure 31, the linear trend patterns are generally consistent – particularly in the tropical Pacific - between the three datasets, providing an important first check on the agreement between the reconstruction and satellite altimeter data.

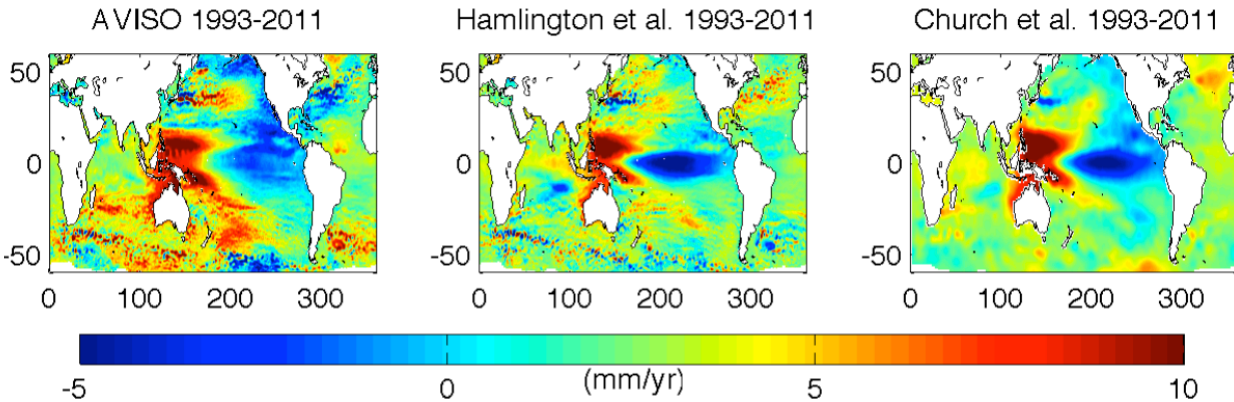


Figure 31. Regional distribution of sea level trends from 1993-2011 for the AVISO dataset (left), the *Hamlington et al.* [2011b] reconstructed sea level (HLK) (center), and the *Church et al.* [2004] reconstructed sea level (CW) (right).

To determine the variability of these trends at the time scales observed over the current altimetric record (roughly twenty years), a lagged correlation analysis is performed, comparing the altimetric trend pattern to twenty-year trends computed from the two sea level reconstructions. As seen in Figure 32, the correlations obtained from the HLK and the CW agree well over the full sixty-year record. There are three extrema in the twenty-year trend variability of the global sea level reconstructions when compared to the altimetric trends: 1957 to 1976, trend centered on 1967/1968; 1968 to 1987, trend centered on 1977/1978, and 1991 to 2010, trend centered on 2000/2001. The 1957-1976 time period is highly correlated with the altimetric trends, showing strong regional sea level trends in the tropical Pacific like those observed during the satellite record. On the other hand, a high anti-correlation is found for the trends computed between 1968 and 1987, with negative trends in the western tropical Pacific and positive trends in the eastern tropical Pacific. This correlations are similar to those seen in Chapter 5 with the 17-

year trend maps. Also notable is the change in sea level trends off the coast of California, with negative trends present during periods of positive correlation (such as the past 20 years), and positive trends during periods of negative correlation.

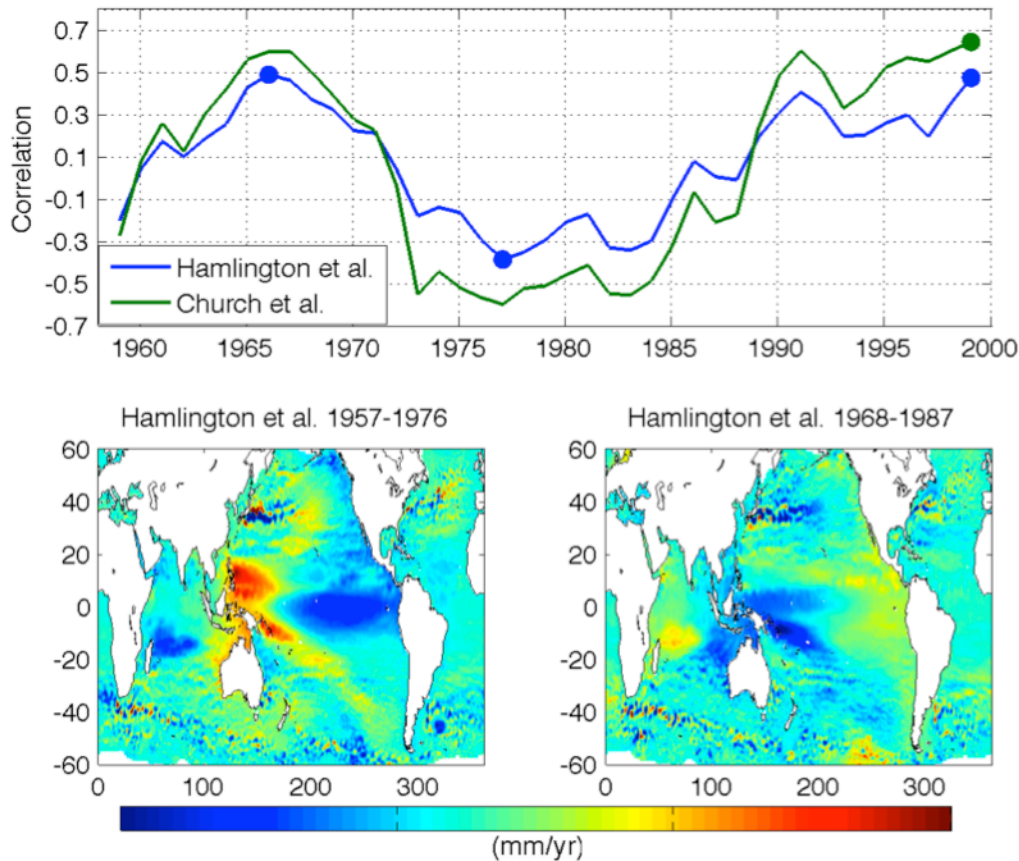


Figure 32. Correlation between the regional trend map from the AVISO dataset and twenty-year trend patterns from two sea level reconstructions, HLK (blue) and CW (green). Twenty-year trend patterns from the HLK dataset are also shown for two different periods associated with extrema in the correlation time series.

While the correlation between the current altimetric trend pattern and trend patterns in the past suggests the spatial distribution of trends observed in the last twenty-years is important, greater significance would be found in determining the dominant or most prevalent twenty-year trend pattern in the last sixty years. The

question can be asked, is there a trend pattern other than the one we are currently observing that has occurred frequently in the past and has a greater influence on global and regional sea level trends? To answer this question, I perform an EOF decomposition of the twenty-year trends from the HLK and the CW datasets, and look at the dominant (first EOF mode) twenty-year trend pattern. Figure 33 shows the first three modes of the EOF decomposition of the trends computed from the HLK dataset. The top panels show the loading vectors, while the bottom panel shows the corresponding principal component time series (PCTS). While only the results from the EOF decomposition of the HLK data are shown, the first three EOF PCTS from HLK and the first three from CW are generally in good agreement. The variance explained by the trend patterns of the first three EOFs is 41%, 30%, and 13%, respectively, with a total of 84% variance in these first three modes. Mode 1 has extrema in 1967, 1977 and 1991, and a similar spatial pattern to those seen in Figure 32. From this, it can be concluded that the current spatial distribution of trends observed during the altimetric record is the dominant twenty-year trend pattern and has shifted between negative and positive extremes during the past sixty years.

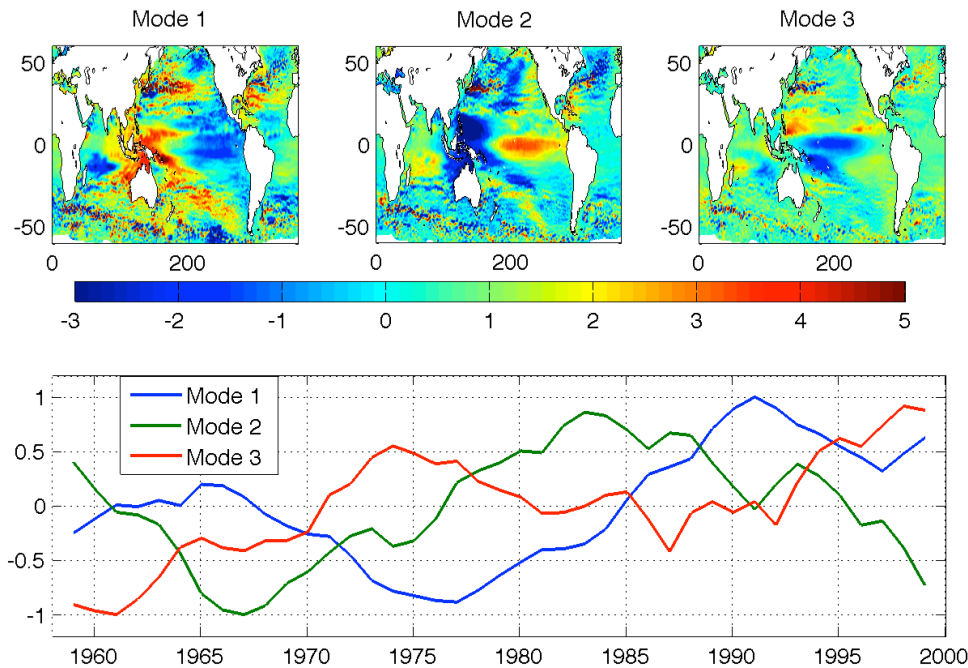


Figure 33. Loading vectors (top) and PCTS (bottom) for the EOF decomposition of twenty-year trends in the HLK dataset. The first three modes are shown, explaining 84% of the variance in the twenty-year trend patterns.

6.3.2 PDO Contribution to Sea Level Trends

As seen from the correlation analysis presented above, the spatial distribution of linear trends during the recent twenty-year altimetric record is not unique within the sixty-year reconstruction record, but corresponds to the positive phase of an oscillating pattern that dominates the trend variability. Attributing this pattern to a climate signal and obtaining a measure of the contribution to GMSL would provide a better understanding of the underlying trend during both the altimetric record and further into the past. When detrended by GMSL, the western Pacific sea level is correlated with the low-frequency variability of the PDO

[*Merrifield et al.*, 2012]. This sea level signal is driven by anomalous decadal wind variability over the equatorial Pacific, and would be expected to influence sea level trends on the timescale of the PDO. To evaluate whether changes in the PDO affect the trends in global mean sea level, a twenty-year running trend computation is performed on the PDO index, which is derived from sea surface temperature measurements in the Pacific [*Cummins et al.*, 2005; *Mantua et al.*, 1997, 2002]. In the top panel of Figure 34, the resulting twenty-year trends from the PDO are compared to mode 1 from the EOF decomposition. The negative of the PDO trends are shown, since the pattern of mode 1 in the north Pacific corresponds to the negative PDO phase in the PDO index. In addition to the agreement of the spatial patterns of mode 1 and the PDO in the north Pacific, the strong relationship between the two is demonstrated by a correlation of 0.96 between the twenty-year PDO trends and mode 1 of the twenty-year trends from the reconstructed sea level dataset.

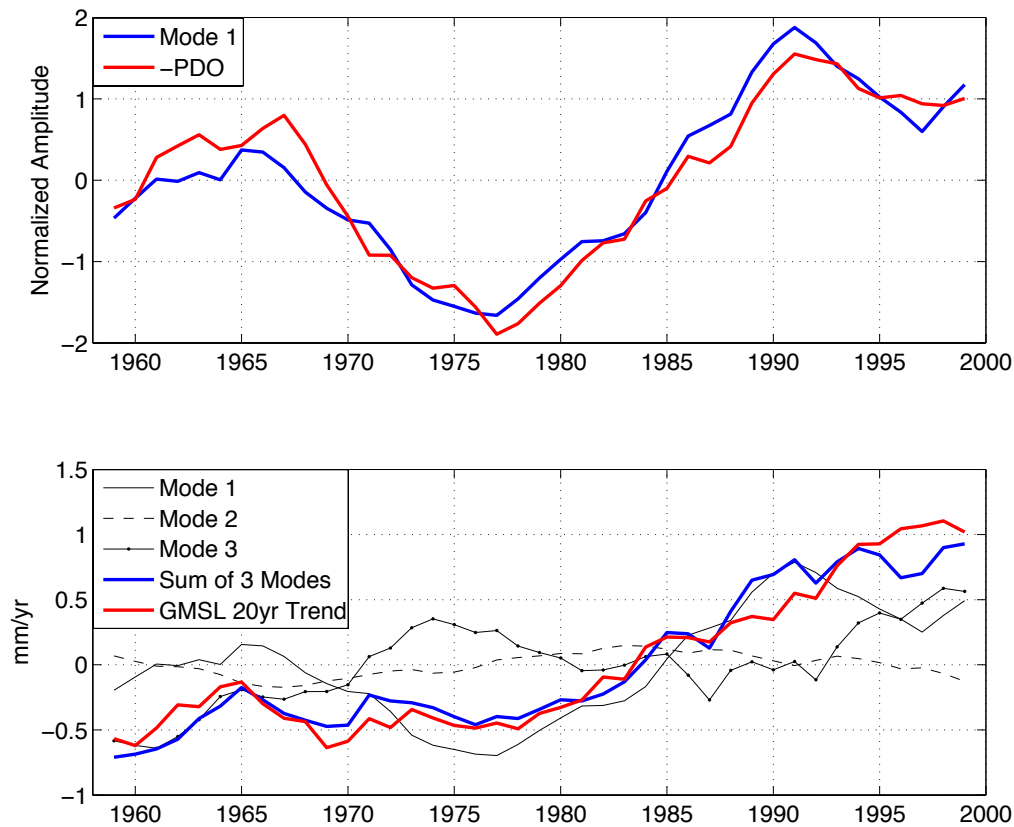


Figure 34. Top: Comparison between the mode 1 of the EOF decomposition of twenty-year trends from the HLK dataset and twenty-year trends computed from the PDO index (shown with opposite sign for direct comparison). Bottom: Contribution of the first three EOF modes to the twenty-year trends in GMSL. For comparison, the twenty-year trends computed directly from the GMSL of HLK are shown with a mean value of 1.54 mm/year removed.

Relating a twenty-year trend pattern derived from the reconstructed sea level to the PDO has important implications for the understanding of decadal fluctuations in GMSL. By combining the mean of the EOF loading vectors with the corresponding PCTS, the contribution of each mode to the twenty-year trends in GMSL can be calculated. In the bottom panel of Figure 34, the contributions to the GMSL trends of the first three EOF modes are shown, in addition to the twenty-

year trends in GMSL of the HLK dataset. An average twenty-year trend of 1.54 mm/year was removed from GMSL in order to make a direct comparison to the EOF decomposition results. As expected, based on the variance explained in the EOF decomposition, the first three modes explain the bulk of the twenty-year trends in GMSL. While mode 2 adds very little to GMSL, mode 1 and mode 3 contribute significantly to the twenty-year trends in GMSL. Mode 3 represents the secular trend in the tide gauges that is not captured by the altimetry-derived basis functions [H2011]. More importantly, however, the contribution of the PDO to twenty-year trends in GMSL can be evaluated from mode 1. Over the last sixty years, mode 1, and by extension the PDO, has contributed significantly at different time periods. During the altimeter time period, the PDO contributed 0.5 mm/year to the trend in GMSL. From 1968 to 1987, however, the PDO lowered the trend in GMSL by 0.7 mm/year. The most significant contribution of the PDO was made during the time period from 1981 to 2000, adding almost 0.8 mm/year to the trend in GMSL.

With an estimate of the actual contribution of the PDO to the trends in GMSL, the influence of the PDO can be removed to gain a better understanding of the underlying secular trend in GMSL that may be associated with anthropogenic climate change. For example, during the satellite altimeter time period, removing a trend of 0.5 mm/year would lead to estimate of the trend in GMSL closer to 2.7 mm/year than to the current estimate of 3.2 mm/year [Mitchum *et al.*, 2010]. The acceleration in the twenty-year trends in GMSL can also be calculated with and

without the PDO. Based on tide gauge analysis, acceleration was estimated in fifteen-year trends in GMSL of approximately 0.1 mm/year^2 since the late 1970s [Merrifield *et al.*, 2009]. With the PDO contribution included, the acceleration of the twenty-year trends in GMSL is found to be 0.04 mm/year^2 over the full record, and an acceleration of approximately 0.08 mm/year^2 since the late 1970s. After removing the PDO contribution, the rate of increase of the twenty-year trends, and hence the acceleration in GMSL becomes 0.02 mm/year^2 over the full record, and approximately 0.02 mm/year^2 since the late 1970s. While unlikely to have a significant impact on accelerations over a longer time period [Church and White, 2011; Woodworth *et al.*, 2009], the change in estimated acceleration has important implications for studying the secular trend in the satellite altimetry data as the record gets longer.

6.3.3 Removing the Spatial Contribution Due to PDO on Sea Level

The subsequent PDO contribution to regional sea level trends from 1993 to 2010 is shown in Figure 35. By removing the sea level trends resulting from the PDO from the AVISO sea level trends, it is possible to isolate the background secular trend from the natural variability and uncover the sea level trend pattern that is at least partially a result of anthropogenic warming. The differenced sea level trend pattern is shown in Figure 35. The large sea level trends over the past two decades around the equator near Indonesia and Papua New Guinea are greatly reduced by removing the PDO contribution. Off the coasts of the Philippines and northeastern Australia, however, the sea level trends are still large.

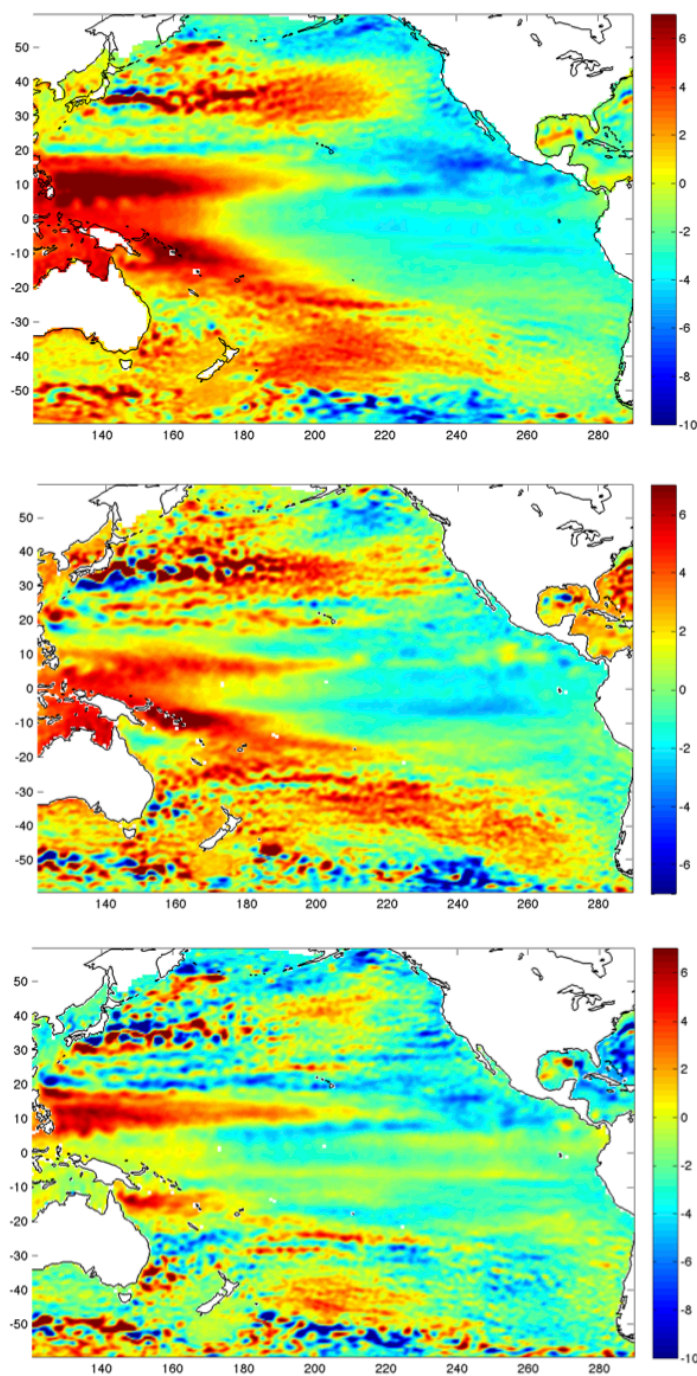


Figure 35. Sea level trends (mm/year) from 1993 to 2010 for (top) AVISO data, (middle) PDO contribution estimated from HLK sea level reconstruction, (bottom) AVISO minus the PDO contribution. Note, GMSL trend has been removed from AVISO data.

Hamlington et al. (Under Review) show that a similar analysis can be completed using wind stress data, reinforcing these results. Further, *Han et al.* [2013], find the warming and cooling of the tropical Indian Ocean (TIO) is in phase with the PDO, *i.e.* when the PDO enters a positive phase, the TIO is warming, and when the PDO transitions to a negative phase, the TIO cools. In the past two decades, however, the PDO has begun a shift to a negative phase, while the TIO has continued to warm. This implies the presence of a persistent warming trend in the TIO that has been attributed to anthropogenic warming, which further indicates that the rapid WTP sea level rise during recent decades is at least in part a result of anthropogenic factors.

6.4 Conclusions and Discussion

By attributing trends, both regionally and globally, to known climate signals, it is possible to improve our understanding of how sea level is rising as a result of the warming climate. Several studies have looked at the relationship between the PDO and sea level in the Pacific [*Meyssignac et al.*, 2012b; *Merrifield et al.*, 2012; *Zhang and Church*, 2012; *Cummins et al.*, 2005] but few have discussed how these signals contribute to trends on a global scale. Using a data-driven technique and without making *a priori* assumptions about the climate signals driving sea level change, the relationship between the PDO and GMSL can be quantified. It is found that removing the influence of the PDO from GMSL lowers the estimated acceleration in GMSL over the past sixty years, suggesting the observed increase in the underlying secular trend in GMSL is more linear than previously thought. With

the short satellite altimeter record alone, it is difficult to assess the contribution of signals like the PDO to decadal – and longer – trends. The reconstructed sea level datasets provide the opportunity to extract these climate signals from the sea level record.

From the analysis done here, the PDO is estimated to contribute over 15% of the GMSL trend during the satellite altimeter period. Determining exactly how the PDO affects and contributes to changes in GMSL is the subject of future study, but it is likely to be a combination of thermosteric and mass changes, driven in some part by related precipitation pattern changes. An additional benefit of attributing sea level trends to a climate signal like the PDO is the ability to project future changes in regional and GMSL trends [*Zhang and Church, 2012*]. For instance, if the PDO changes sign from the positive to the negative phase (decreasing trend in the PDO), the sea level trends off the coast of California will be negative, while the trends in the western tropical Pacific will be positive. Similarly, when the PDO undergoes a change from negative phase to positive phase (increasing trend in the PDO), sea level will rise off the coast of California and fall in the western tropical Pacific. This can also be applied to changes in GMSL. Positive to negative shifts in the PDO will result in acceleration in GMSL, while negative to positive shift will cause a deceleration in GMSL. According to the index derived from SST measurements, the PDO has undergone a shift from positive to negative in the last ten to twenty years with a corresponding decreasing trend. However, based on the period of the PDO, it should shift phase again within the next ten to twenty years,

leading to the possibility of lower sea level in the western Pacific and rising sea level off the coast of California. In addition, such a shift would lead to a deceleration in the rate of GMSL rise.

It is also found that removing the effect of this natural variability does have a significant impact on the resulting spatial trend pattern. This reinforces the idea anthropogenic forcing may play a large role in sea level rise in the region. Additionally, the prevailing thought has been that once the PDO shifts and changes sign, the sea level rise in the western tropical Pacific will ease and future decades will hold much more manageable levels of sea level change for the region. While this appears to be the case for areas near Indonesia, in the light of the results presented here, the high rate of sea level rise near the Philippines and northeastern Australia should not be similarly expected to abate.

While identifying the climate signals and processes that contribute to regional and global sea level trends can provide insight into past and future sea level change, it is important to keep this in context. The PDO contribution to the twenty-year trends discussed here is only a fraction of the twenty-year trends in GMSL. The PDO causes acceleration and deceleration in GMSL on decadal timescales, and appears to have a significant impact on regional sea level change. The underlying secular trend in sea level is much larger than the PDO contribution, and over the last sixty years, the twenty-year trends in GMSL have consistently been positive. With the results presented here, however, a better understanding of

this underlying trend can be developed, particularly during the satellite altimeter era, insight into how sea level may change in the coming decades can be provided.

CHAPTER 7 CONCLUSION

With the expectation that global sea level will continue to climb in upcoming years, it is crucial to understand what factors contribute to sea level rise and how sea level has behaved in the past. Understanding variations in the ocean can have massive implications, such as improving knowledge of a localized transport, like that seen with the NEC bifurcation point, or looking at the pattern of sea level trend in a very vulnerable region, as seen with the SEAS analysis, or finding a known signal contributes to a significant portion of recent global sea level rise, as was done with the PDO contribution to GMSL. All of these consequential findings would not be possible without information provided by reconstructing sea level.

Sea level reconstruction allows for the combination of two data sources, taking the benefits of both and creating a globally extensive dataset with a much longer temporal span than is currently available through satellite remote sensing. This work shows that reconstructing sea level is not a trivial task, but can be done in such a way as to create reconstructions that are quite similar to the calibration data. If nothing else, I hope the reconstruction comparisons shown here instill an understanding and confidence in the skill of reconstructed datasets, and help to expand the value of reconstructions in the future. It has been just 10 years since the first sea level reconstruction was publicly available, but the amount of science

made possible from reconstructions since their introduction is astounding. Methods for creating reconstructions have continued to evolve (from EOFs to CSEOFs to bivariate CSEOFs), improving their quality and exposure. With more and more attention from the public and the scientific community, it is likely that the utility of reconstructions will continue grow, helping to increase our understanding of sea level variations on both global and regional scales.

The potential for groundbreaking future discoveries from sea level reconstruction is very good. In the previous section, I look at regional sea level trend patterns without the contribution from PDO, which provides a pattern of sea level trend that may be largely unattributable to natural variation. Going forward, using longer records made possible by sea level reconstruction along with additional historical data, it is likely that understanding of how sea level is altered by anthropogenic factors will increase greatly.

CHAPTER 8 REFERENCES

- Beckley, B.D., F.G. Lemoine, S.B. Lutchke, R.D. Ray, and N.P. Zelensky, (2007), A reassessment of global and regional mean sea level trends from TOPEX and Jason-1 altimetry based on revised reference frame and orbits. *Geophys. Res. Lett.* **34**, L14607.
- Berge-Nguyen, M., A. Cazenave, A. Lombard, W. Llovel, J. Viarre, and J. F. Cretaux (2008), Reconstruction of past decades sea level using thermosteric sea level, tide gauge, satellite altimetry and ocean reanalysis data, *Global Planet. Change*, 62, 1-13, doi:10.1016/j.gloplacha.2007.11.007
- Bromirski, P. D., A.J. Miller, R.E. Flick, and G. Auad (2011), Dynamical suppression of sea level rise along the Pacific Coast of North America: Indications for imminent acceleration. *J. Geophys. Res.* **116**, C07005.
- Carton, J.A. and B.S. Giese, (2008): A reanalysis of ocean climate using Simple Ocean Data Assimilation (SODA), *Monthly Weather Review*, 136, 2999-3017.
- Cazenave, A., and R.S. Nerem (2004), Present day sea level change: Observations and causes. *Rev. Geophys.* **42**, RG3001.
- Cazenave, A., and W. Llovel (2010), Contemporary sea level rise, *Annu. Rev. Mar. Sci.* **2**, 145–173.

- Chambers, D.P., C.A. Melhaff, T.J. Urban, D. Fuji, and R.S. Nerem (2002), Low-frequency variations in global mean sea level: 1950-2000, *J. Geophys. Res.* 107, 3026. doi: 10.1029/2001JC001089.
- Chambers, D. P., M. A. Merrifield, and R. S. Nerem (2012), Is there a 60-year oscillation in global mean sea level, *Geophys. Res. Lett.*, 39, L18607, doi:10.1029/2012GL052885.
- Chelton, D.B., J.C. Ries, B.J. Haines, L.-L. Fu, and P.S. Callahan (2001). Satellite Altimetry. In: Fu, L.L. and A. Cazenave (eds.), *Satellite Altimetry and Earth Sciences: A handbook of techniques and applications*, pp. 1-133, Academic Press, San Diego.
- Christiansen, B., T. Schmith, and P. Thejll (2010), A Surrogate Ensemble Study of Sea Level Reconstructions, *J. Clim.*, 23:4306-4326. 106 , doi: 10.1175/2010JCLI3014.1.
- Church, J.A., N.J. White, R. Coleman, K. Layback, and J.X. Mitrovica (2004), Estimates of the regional distribution of sea level rise over the 1950-2000 period, *J. Clim.*, 17: 2609-2625, doi: 10.1175/1520-0442(2004)017%3C2609:EOTRDO%3E2.0.CO;2.
- Church, J.A. and N.J. White (2006), A 20th century acceleration in global sea level rise, *Geophys. Res. Lett.* 36, L040608.
- Church, J.A., and N.J. White. (2011), Sea-Level Rise from the Late 19th to the Early 21st Century, *Surv. in Geophys.*, 32-4:585-602, doi: 10.1007/s10712-011-9119-1.

- Cummins, P., G. Lagerloef and G. Mitchum (2005), A regional index of northeast Pacific variability based on satellite altimeter data, *Geophys. Res. Lett.*, VOL. 32, L17607, doi:10.1029/2005GL023642.
- Dussin R., A.M. Treguier, J.M. Molines, B. Barnier, T. Penduff, L. Brodeau, G. Madec (2009). Definition of the interannual experiment ORCA025-B83, 1958–2007. LPO Report 902.
- Feng, M., Y. L, and G. Meyers (2004), Multidecadal variations of Fremantle sea level: Footprint of climate variability in the tropical Pacific, *Geophys. Res. Lett.* **31**, L16302.
- Fourcy, D. and O. Lorvelec (2013). A new digital map of limits of oceans and seas consistent with high-resolution global shorelines. *Journal of Coastal Research*, 29(2), 471-477. doi: 10.2112/JCOASTRES-D-12-00079.1
- Hamlington, B.D., R.R. Leben, R.S. Nerem, and K.-Y. Kim (2011), The effect of signal-to-noise ratio on the study of sea level trends, *J. Climate* **24**, 1396-1408.
- Hamlington, B.D., R.R. Leben, R.S. Nerem, W. Han, K.-Y. Kim, (2011b), Reconstructing sea level using cyclostationary empirical orthogonal functions. *J. Geophys. Res.*, 116:C12015. doi:10.1029/2011JC007529.
- Hamlington, B. D., R. R. Leben, and K.-Y. Kim. (2012), Improving sea level reconstructions using non-sea level measurements, *J. Geophys. Res.*, 117, C10025, doi:10.1029/2012JC008277.

- Hamlington, B. D., R. R. Leben, M. W. Strassburg, R. S. Nerem, and K.-Y. Kim (2013), Contribution of the Pacific Decadal Oscillation to global mean sea level trends, *Geophys. Res. Lett.*, 40, 5171–5175, doi:10.1002/grl.50950.
- Hamlington, B.D., R.R. Leben, M. W. Strassburg, K.-Y. Kim (2014), Cyclostationary empirical orthogonal function sea-level reconstruction. *Geoscience Data Journal*. doi: 10.1002/gdj3.6
- Hamlington, B.D., M.W. Strassburg, R.R. Leben, W. Han, R.S. Nerem, and K.-Y. Kim (Under Review), Uncovering the Anthropogenic Warmin-Induced Sea Level Rise Signal in the Pacific Ocean, *Nat. Geosci.*
- Han W., G.A. Meehl, A. Hu, M. Alexander, T. Yamagata, D. Yuan, M. Ishii, P. Pegion, J. Zheng, B. Hamlington, X.-W. Quan, and R. Leben (2013), Intensification of decadal and multi-decadal sea level variability in the western tropical Pacific during recent decades. *Clim. Dyn.*, DOI:10.1007/s00382-013-1951-1.
- Kaplan, A.M., M.A. Cane, Y. Kushnir, A.C. Clement, M.B. Blumenthal, and B. Rajagopalan (1998), Analyses of global sea surface temperature 1856-1991, *J. Geophys. Res.*, 103:18567-17589, doi: 10.1029/97JC01736.
- Kerr, R. A. (2000), A North Atlantic climate pacemaker for the centuries, *Science*, 288, 1984–1985, doi: 10.1126/science.288.5473.1984
- Kim, K.-Y., G.R. North and J. Huang (1996), EOFs of one-dimensional cyclostationary time series: Computations, examples, and stochastic

- modeling. *J. Atmos. Sci.*, 53: 1007-1017, doi: 10.1175/1520-0469(1996)053<1007:EOODCT>2.0.CO;2.
- Kim, K.-Y., and G.R. North (1997), EOFs of harmonizable cyclostationary processes, *J. Atmos. Sci.*, 54, 2416-2427, doi: 10.1175/1520-0469(1997)054%3C2416:EOHCP%3E2.0.CO;2.
- Kim, K.-Y. and Q. Wu. (1999), A comparison of study of EOF techniques: Analysis of nonstationary data with periodic statistics. *J. Climate*, 12:185-199, doi: 10.1175/1520-0442-12.1.185
- Kim, K.-Y. and C. Chung. (2001), On the evolution of the annual cycle in the tropical Pacific. *J. Climate*, 14:991-994.
- Kimura, S., T. Inoue, and T. Sugimoto, 2001: Fluctuations in the distribution of low-salinity water in the North Equatorial Current and its effect on the larval transport of the Japanese eel. *Fish. Oceanogr.*, 10, 51–60.
- Le Traon, P.-Y., F. Nadal, N. Ducet (1998), An improved mapping method of multi-satellite altimeter data. *J. Atmos. Oceanic Technol.*, 15, 522-534, doi: 10.1175/1520-0426(1998)015<0522:AIMMOM>2.0.CO;2.
- Llovel, W., A. Cazenave, P. Rogel, A. Lombard, and M. B. Nguyen (2009), Two-dimensional reconstruction of past sea level (1950–2003) from tide gauge data and an Ocean General Circulation Model, *Clim. Past*, 5, 217-227, doi:10.5194/cp- 5-217-2009.

- Mantua, N.J., S.R. Hare, Y. Zhang, J.M. Wallace, and R.C. Francis (1997), A Pacific interdecadal climate oscillation with impacts on salmon production, *Bull. of Amer. Meteor. Soc.*, **78**, 1069-1079.
- Mantua, N. J., and S.R. Hare (2002), The Pacific Decadal Oscillation, *J. Oceanogr.* **58**, 35–44.
- Merrifield, M. A., S.T. Merrifield, and G.T. Mitchum. (2009), An Anomalous Recent Acceleration of Global Sea Level Rise. *J. Climate*, **22**, 5772–5781.
- Merrifield, M.A., P. Thompson, and M. Lander (2012), Multidecadal sea level anomalies and trends in the western tropical Pacific. *Geophys. Res. Lett.* **39**, 13.
- Meyssignac, B., M. Becker, W. Llovel, and A. Cazenave (2012), Assessment of two dimensional past sea level reconstructions over 1950-2009 based on tide-gauge data and different input sea level grids. *Surv. Geophys.* Doi:10.1007/s10712-011-9171-x.
- Meyssignac, B., D. Salas y Melia, M. Becker, W. Llovel, and A. Cazenave (2012b). "Tropical Pacific spatial trend patterns in observed sea level: internal variability and/or anthropogenic signature?" *Climate of the Past* 8, no. 2: 787-802.
- Mitchum, G. T., R.S. Nerem, M.A. Merrifield, and W.R. Gehrels (2010), *Modern sea-level-change estimates, in Understanding Sea-level Rise and Variability*, edited by J. A. Church et al., pp. 122–142, (Wiley, Chichester, U. K.).

- Nerem, R. S. (1995), Global Mean Sea Level Variations from TOPEX/POSEIDON Altimeter Data. *Science* 268: 708-710.
- Nitani, H., 1972: Beginning of the Kuroshio. *Kuroshio: Its Physical Aspects*, H. Stommel and K. Yoshida, Eds., University of Tokyo Press, 129–163.
- Perrette, M., F. Landerer, R. Riva, K. Frieler, and M. Meinshausen (2013), A scaling approach to project regional sea level rise and its uncertainties, *Earth Syst. Dynam.*, 4, 11-29, doi:10.5194/esd-4-11-2013.
- Qiu, B., and R. Lukas, 1996: Seasonal and interannual variability of the North Equatorial Current, the Mindanao Current and the Kuroshio along the Pacific western boundary. *J. Geophys. Res.*, 101, 12 315–12 330.
- Qiu, B., and S. Chen (2010), Interannual-to-Decadal Variability in the Bifurcation of the North Equatorial Current off the Philippines. *J. Phys. Oceanogr.*, 40, 2525-2538, doi: 10.1175/2010JPO4462.1
- Ray, R. and B. Douglas (2011), Experiments in reconstructing twentieth-century sea level 1048 levels, *Prog. Oceanogr.*, 91, 496-515, doi: 10.1016/j.pocean.2011.07.021.
- Reaka-Kudla, M. L. 1997. The global biodiversity of coral reefs: A comparison with rainforests. *In: Reaka-Kudla, M. L., D. E. Wilson, and E. O. Wilson (eds.), Biodiversity II: Understanding and Protecting Our Natural Resources*, pp. 83-108. Joseph Henry/National Academy Press, Washington, D. C.
- Rio, M. H., S. Guinehut, and G. Larnicol (2011), New CNES-CLS09 global mean dynamic topography computed from the combination of GRACE data,

altimetry, and in situ measurements, *J. Geophys. Res.*, 116, C07018, doi:10.1029/2010JC006505.

Slangen, A. B. A., C. A. Katsman, R. S. W. van de Wal, L. L. A. Vermeersen, R. E. M. Riva (2012), Towards regional projections of twenty-first century sea-level change based on IPCC SRES scenarios, *Clim. Dyn.*, doi:10.1007/s00382-011-1057-6

Smith, T.M., R.W. Reynolds, R.E. Livezey, and D.C. Stokes (1996), Reconstruction of historical sea surface temperatures using empirical orthogonal functions, *J. Climate*, 9:1403-1420, doi: 10.1175/1520-0442(1996)009<1403:ROHSST>2.0.CO;2.

Smith, T.M., and R.W. Reynolds (2004), Improved extended reconstruction of SST (1854–1997). *J. Climate*, 17, 2466–2477, doi: 10.1175/1520-0442(2004)017%3C2466:IEROS%3E2.0.CO;2.

Stenseth, N.C., G. Ottersen, J.W. Hurrell, A. Mysterud, M. Lima, K.S. Chan, N.G. Yoccoz, and B. Ådlandsvik (2003), Studying climate effects on ecology through the use of climate indices: the North Atlantic Oscillation, El Nino Southern Oscillation and beyond, *Proc. R. Soc. Lond. B*, 270, pp. 2087–2096, doi: 10.1098/rspb.2003.2415.

Strassburg, M.W., B.D. Hamlington, R.R. Leben, P. Manurung, J. Lumban Gaol, B. Nababan, S. Vignudelli, and K.-Y. Kim (In Prep.), Sea Level Trends in South East Asian Seas (SEAS), *Climate of the Past*.

- Strassburg, M.W., B.D. Hamlington, R.R. Leben, and K.-Y. Kim (Under Review), A Comparative Study of Sea Level Reconstruction Techniques Using 20 Years of Satellite Altimetry Data, *J. Geophys. Res.*
- Sturges, W., and Douglas B.C. (2011), Wind effects on estimates of sea level rise, *J. Geophys. Res.* **116**, C06008.
- van Onselen, K.I., (2000), The influence of data quality on the detectability of sea-level height variations. Ph.D. Thesis, NCG Publications on Geodesy, vol. 49, TU Delft, Delft, Netherlands.
- Wijffels, S.E. and G.A. Meyers (2004), An intersection of oceanic waveguides: variability in the Indonesian throughflow region. *J Phys. Oceanogr* 34:1232-1253.
- Woodworth, P. L., N.J. White, S. Jevrejeva, S.J. Holgate, J.A. Church, W.R. Gehrels (2009), Evidence for the accelerations of sea level on multi-decade and century timescales, *Int. J. Climatol.* **29**, 777–789.
- Yeo, S.R., and K.-Y. Kim (2013), Global warming, low-frequency variability, and biennial oscillation: an attempt to understand the physical mechanisms driving major ENSO events, *Climate Dynam.*, doi: 10.1007/s00382-013-1862-1.
- Zhang, X., and J.A. Church (2012), Sea level trends, interannual and decadal variability in the Pacific Ocean, *Geophys. Res. Lett.* **39**, L21701.